Signatures of Majorana zero-modes in nanowires, quantum spin Hall edges, and quantum dots

Mi, S.

Signatures of Majorana zero-modes in nanowires, quantum spin Hall edges, and quantum dots

Proefschrift

ter verkrijging van
de graad van Doctor aan de Universiteit Leiden,
op gezag van Rector Magnificus
prof. mr. C. J. J. M. Stolker,
volgens besluit van het College voor Promoties
te verdedigen op woensdag 22 april 2015
klokke 15.00 uur

door

Shuo Mi

geboren te Beijing, China in 1983

Promotiecommissie

Promotor:	Prof. dr. C. W. J. Beenakker
Co-promotor:	Dr. M. T. Wimmer (Delft University of Technology)
Overige leden:	Dr. A. R. Akhmerov (Delft University of Technology)
	Prof. dr. E. R. Eliel
	Prof. dr. C. Morais Smith (Utrecht University)
	Prof. dr. J. M. van Ruitenbeek

Casimir PhD Series 2015-06
ISBN 978-90-8593-214-7
An electronic version of this thesis can be found at
https://openaccess.leidenuniv.nl

This work is part of the research programme of the Foundation for Fundamental Research on Matter (FOM), which is part of the Netherlands Organisation for Scientific Research (NWO).

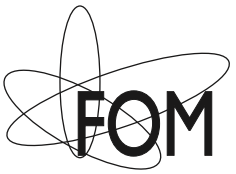

Cover: *Evolution of the differential conductance of a superconducting quantum dot upon variation of an external parameter (such as the magnetic field). The circles indicate the poles of the scattering matrix in the complex energy plane. The accumulation of poles on the imaginary axis gives rise to a Y-shaped conductance resonance profile, which can be mistaken for a Majorana zero-mode. (See chapter 5.)*

To my mother and grandmother

献给我的母亲和姥姥

Contents

Chapter 1

Introduction

1.1 Preface

Majorana zero-modes, also referred to as *Majorana bound states* or *Majorinos*, are states in the middle of the excitation gap of a superconductor (so at zero excitation energy), bound to a magnetic vortex or other defect. The name goes back to a concept introduced by the Italian physicist Ettore Majorana [1], of a charge-neutral fermionic particle that is identical to its anti-particle. Such *Majorana fermions* may or may not be realized as fundamental particles in high energy physics, but in superconductors they appear naturally when a Cooper pair breaks up [2].

In field theory, particles that are their own anti-particles must be described by a real field, as the complex conjugate of a field creates the anti-particle. It is quite common for a bosonic particle to be described by a real field, the electromagnetic field of a photon being a familiar example. However, the field of a fermion is described by the Dirac equation, which is a complex wave equation. This led Paul Dirac to predict the existence of positrons as the anti-particles of electrons, given by a complex conjugate solution of his equation. What seemed to be a mathematical necessity was challenged in 1937 by Majorana, who showed that the Dirac equation allowed for real solutions. This opened up the possibility for the existence of charge-neutral fermions that would be their own anti-particle.

The search for Majorana fermions in particle physics focuses on the detection of the annihilation of pairs of neutrinos, to demonstrate the identity of neutrino and antineutrino [3]. But so far whether neutrinos

are Majorana fermions is still an open question.

The situation is altogether different in superconductors: There Majorana fermions appear naturally as non-fundamental quasiparticles either localized or propagating inside specific solid state systems as a result of an unpaired electron can be seen equally well as a charge excess or a charge deficit of e. In an effective mean-field description the quasiparticle charge is therefore only conserved modulo $2e$, and this makes it possible to construct a coherent superposition of empty and filled states, i. e. electrons and holes, which is described by a real wave equation of the Majorana type. Pairs of superconducting quasiparticles, known as Bogoliubov quasipartiles which is a coherent supperposition of electrons and holes, can annihilate upon collision, demonstrating their Majorana nature [4].

Majorana fermions can be bound to a defect [5, 6]. The identity of particle and antiparticle then demands that this bound state is at zero energy, in the middle of the excitation gap. This socalled Majorana zero-mode is no longer a fermion, instead its statistics upon pairwise exchange depends on the order of the exchange operation [7]. Such non-Abelian statistics can be used to perform logical operations [8], an application known as topological quantum computation [9].

Although the earliest proposals to realize Majorana zero-modes in superconductors go back many decades [6, 7], these required an exotic form of pairing inside chiral p-wave superconductors. It was only realized recently that conventional s-wave pairing is sufficient in combination with spin-orbit coupling [10–13]. By now there is a great variety of systems in which Majorana zero-modes have been predicted [14–18], and there is mounting experimental evidence for their observation [19–23]. One such observation is shown in Figure 1.1 in a system of one dimensional semicondctor InSb nanowire with proximity to Nb superconducting reservoir.

In this thesis three platforms for Majorana zero-modes are investigated theoretically: one dimensional nanowires (Chapter 2), two dimensional topological insulators (Chapters 3, 4), and zero dimensional quantum dots (Chapters 5, 6). In this introductory chapter I will give an overview of the basic concept of a Majorana zero-mode, explaining the role played by superconductivity, followed by a discussion of identifying signatures and applications to quantum computation. Then a brief summary of each of the following chapters is given.

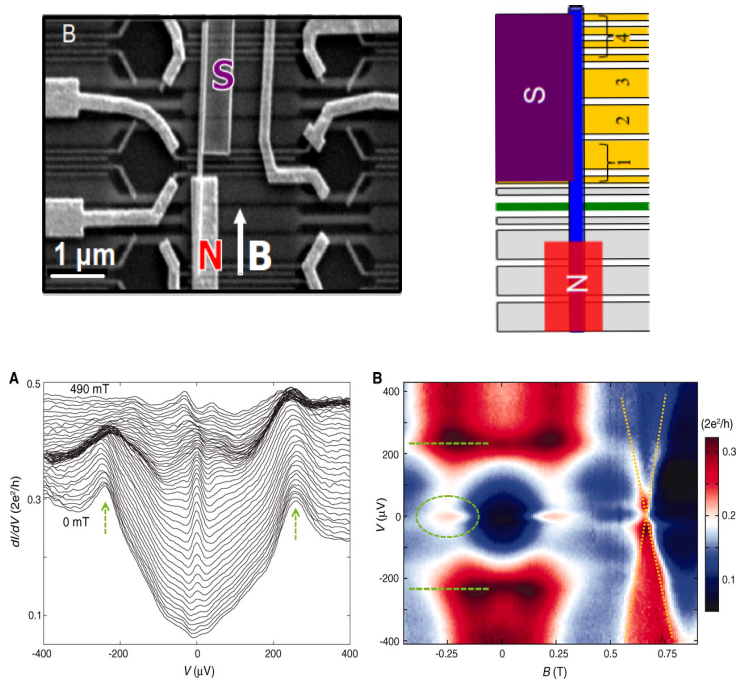

Figure 1.1. The first experimental observation of a Majorana zero-mode in a measurement of the differential conductance of an InSb nanowire coupled to a Nb superconductor. The zero-mode shows up as a zero-bias peak, emerging and persisting over a range of magnetic fields. Pictures taken from Ref. [19]. Reprinted with permission from AAAS.

1.2 The basics of Majorana zero-modes

1.2.1 The key role played by superconductivity

To construct a charge-neutral Majorana fermion in condensed matter one has to start with building blocks which are charged, electrons and holes. The hole is a vacancy state created below the Fermi level when an electron is excited above the Fermi sea. One can combine an electron and a hole to make a charge-neutral quasiparticle called an *exciton*. Since the exciton is a two-particle state combining a pair of half-integer-spin fermions, it is an integer-spin *boson*, like a photon.

To make a charge-neutral *fermion*, one needs to create a single-particle

state as a coherent superposition of electron and hole. Such a coherent superposition requires a superconducting condensate. The idea is based on the understanding that the ground state of a superconductor is a collective condensate of pairs of electrons with opposite momentum and spin, socalled *Cooper pairs*. As illustrated in Fig. 1.2, an unpaired electron then differs from an unpaired hole by one Cooper pair. Scattering processes that convert an electron into a hole, known as Andreev scattering or Andreev reflection, preserve energy and momentum but charge, and switch spin bands. It then becomes possible by adding or removing a Cooper pair from the condensate without consuming extra energy. This coupling of electron and hole degrees of freedom makes it possible to create a coherent superposition of oppositely charged quasiparticles. This charge-neutral excitation, a socalled Bogoliubov quasiparticle, is the superconducting analogue of a Majorana fermion.

To go from a Majorana fermion to a Majorana zero-mode we need to confine the quasiparticle. Fig. 1.3 shows the spectrum of bound states, socalled Andreev levels, existing within the superconducting gap in the core of a magnetic vortex. Due to particle-hole symmetry, the energy spectrum is symmetric with respect to the Fermi level at $\varepsilon = 0$, halfway within the gap at $\pm\Delta$. In a conventional superconductor the zero-point motion prevents the appearance of a level at $\varepsilon = 0$. All levels then come in $\pm\varepsilon$ pairs. An unpaired level at $\varepsilon = 0$ appears in a topological superconductor. This zero-mode is pinned, and it cannot move up or down in energy without breaking particle-hole symmetry. Because it is at zero excitation energy, it is half-particle and half-hole, so it is its own antiparticle. Hence the name Majorana zero-mode.

1.2.2 Majorana operators

The properties of Majorana zero-modes are conveniently described in second quantization representation, in terms of identical creation and annihilation operators. To introduce these, we consider the simplest case of one fermionic state. It can be either an empty state $|0\rangle \equiv \binom{1}{0}$ or an occupied state $|1\rangle \equiv \binom{0}{1}$. We can define creation and annihilation operators by

$$c_1^\dagger = |1\rangle\langle 0| = \begin{pmatrix} 0 & 0 \\ 1 & 0 \end{pmatrix}, \quad c_1 = |0\rangle\langle 1| = \begin{pmatrix} 0 & 1 \\ 0 & 0 \end{pmatrix}. \tag{1.1}$$

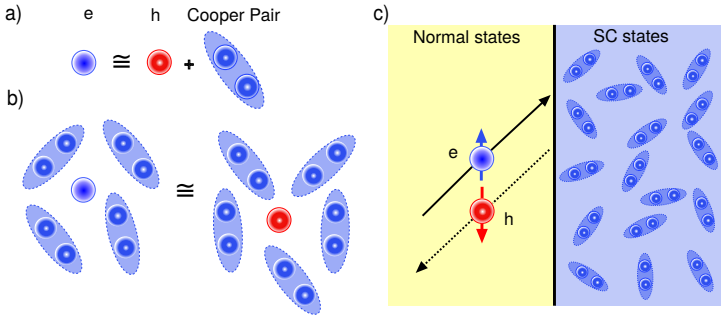

Figure 1.2. Panels (a) and (b) illustrate that an unpaired electron in a sea of Cooper pairs is equivalent to an unpaired hole. Panel (c) shows the conversion of an electron into a hole by Andreev reflection at the interface between a normal metal and a superconductor.

These operators satisfy fermionic anti-commutation relations,

$$\{c_i\,, c_j^\dagger\} = \delta_{ij}, \quad \{c_i\,, c_j\,\} = \{c_i^\dagger, c_j^\dagger\} = 0. \tag{1.2}$$

Majorana operators are constructed from the creation and annihilation operators,

$$\gamma_1 = c_1 + c_1^\dagger = \begin{pmatrix} 0 & 1 \\ 1 & 0 \end{pmatrix} = \sigma_x, \tag{1.3}$$

$$\gamma_2 = -\,i(c_1 - c_1^\dagger) = \begin{pmatrix} 0 & -i \\ i & 0 \end{pmatrix} = \sigma_y, \tag{1.4}$$

$$c_1^\dagger = \frac{\gamma_1 - i\gamma_2}{2},\; c_1 = \frac{\gamma_1 + i\gamma_2}{2}. \tag{1.5}$$

These are Hermitian operators, $\gamma_i = \gamma_i^\dagger$ ($\gamma_i^2 = \gamma_i^{\dagger 2} = 1$), obeying a modified anti-commutation relation:

$$\{\gamma_i, \gamma_j\} = 2\delta_{ij}. \tag{1.6}$$

In the terms of the Majorana operators the fermion number operator takes the form

$$\hat{\mathcal{N}} = c_1^\dagger c_1 = \frac{1 - i\gamma_2\gamma_1}{2}, \tag{1.7}$$

and the fermion parity operator is

$$\hat{\mathcal{P}} = i\gamma_2\gamma_1 = \sigma_z = (-1)^{\hat{\mathcal{N}}} = \mathrm{e}^{i\pi\hat{\mathcal{N}}} = \begin{pmatrix} 1 & 0 \\ 0 & -1 \end{pmatrix}. \tag{1.8}$$

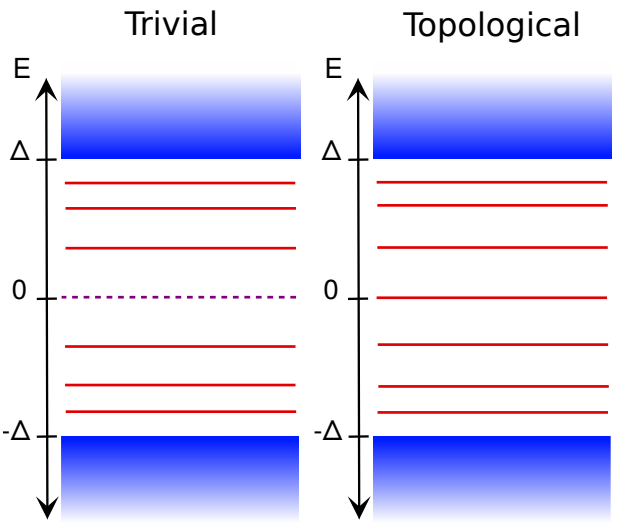

Figure 1.3. The distinction between the excitation spectrum of a conventional superconductor (left panel) and a topological superconductor (right panel). In both cases the spectrum has $\pm E$ symmetry, but the topological superconductor has an unpaired zero mode.

The fermion parity is $+1$ for the unoccupied state $|0\rangle$, and -1 for the occupied state $|1\rangle$. Note that $\{\gamma_i, \hat{\mathcal{P}}\} = 0$.

We may generalize this construction to an N-fermion state, giving rise to $2N$ Majorana operators,

$$\begin{aligned} \gamma_{2i-1} &= c_i + c_i^\dagger, \;\; c_i^\dagger = \frac{\gamma_{2i-1} - i\gamma_{2i}}{2}, \\ \gamma_{2i} &= -i(c_i - c_i^\dagger), \;\; c_i = \frac{\gamma_{2i-1} + i\gamma_{2i}}{2}. \end{aligned} \tag{1.9}$$

The corresponding fermion number and parity operators are given by

$$\hat{\mathcal{N}}_i = c_i^\dagger c_i = \frac{1 - i\gamma_{2i}\gamma_{2i-1}}{2}, \tag{1.10}$$

$$\hat{\mathcal{P}} = i\gamma_{2N}\gamma_{2N-1}\cdots i\gamma_2\gamma_1 = (-1)^{\sum_{i=1}^{N}\hat{\mathcal{N}}_i}. \tag{1.11}$$

It is worth to note that any Hamiltonian which is quadratic in the fermionic creation and annihilation operators preserves fermion parity, i. e. $[\hat{\mathcal{P}}, \hat{\mathcal{H}}] = 0$. Therefore, the Hilbert space of $2N$ Majorana operators

divides into even and odd fermion number sectors, each of dimension 2^{N-1}.

1.2.3 Kitaev chain and Majorana zero-modes

As a simple example for the appearance of Majorana zero-modes, we now discuss the Kitaev chain model of a topological superconductor [24]. In this model the pair potential Δ involves electrons with the same spin on neighboring sites of the chain, so the spin degree of freedom can be ignored. Including also the nearest neighbor hopping energy t and chemical potential μ on N sites of the chain, the Hamiltonian is

$$H = \mu \sum_{i}^{N} c_i^\dagger c_i - \sum_{i=1}^{N-1} \left[t \left(c_i^\dagger c_{i+1} + c_{i+1}^\dagger c_i \right) + \Delta \left(c_i \, c_{i+1} + c_{i+1}^\dagger c_i^\dagger \right) \right]. \quad (1.12)$$

Upon Fourier transformation,

$$c_i = \frac{1}{\sqrt{N}} \sum_{k=-\infty}^{+\infty} \mathrm{e}^{-ik\cdot x_i} c_k, \; c_i^\dagger = \frac{1}{\sqrt{N}} \sum_{k=-\infty}^{+\infty} \mathrm{e}^{+ik\cdot x_i} c_k^\dagger, \quad (1.13)$$

the Hamiltonian can be rewritten in a matrix form in Nambu space,

$$H = \frac{1}{2} \sum_{k=0}^{\infty} \begin{pmatrix} c_k^\dagger & c_{-k} \end{pmatrix} h_{BdG} \begin{pmatrix} c_k \\ c_{-k}^\dagger \end{pmatrix}, \quad (1.14)$$

where h_{BdG} is the socalled Bogoliubov-de Gennes Hamiltonian. For the Kitaev model it has the form

$$h_{BdG} = (\mu - 2t\cos k)\tau_z + (2\Delta \sin k)\tau_y = \epsilon_k \tau_z + \Delta_k \tau_y = \mathbf{d} \cdot \boldsymbol{\tau}, \quad (1.15)$$

where $\mathbf{d} = (0, \Delta_k, \epsilon_k)$ and $\boldsymbol{\tau} = (\tau_x, \tau_y, \tau_z)$. The energy spectrum is given by $E_k = \pm\sqrt{\epsilon_k^2 + \Delta_k^2} = \pm|\mathbf{d}|$. When k runs over the Brillouin zone $k \in [0, 2\pi]$ the vector $\mathbf{d}(k)$ forms a closed loop winding around the origin an even number of times, i.e. the topologically trivial case, or an odd number of times, i.e. the topologically nontrivial case. The former corresponds to $|\mu| > |2t|$, while the latter corresponds to $|\mu| < |2t|$.

The topologically nontrivial case $|\mu| < |2t|$ has Majorana zero-modes at the end points of the chain. To see this, we transform from the

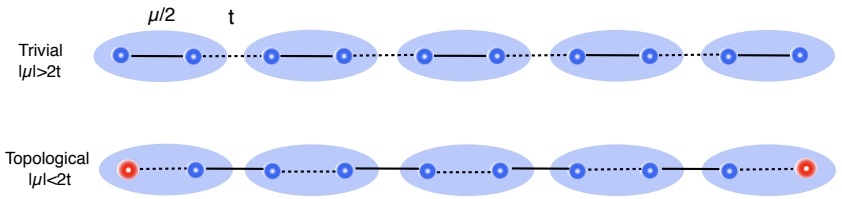

Figure 1.4. A schematic demonstration of the appearance of unpaired Majorana zero-modes (red dots) at the end points of the Kitaev chain. The shadow area indicates a site of the lattice, with a fermionic operator c_i represented by a pair of Majorana operators γ_{2i-1} and γ_{2i}.

operators c_n to the Majorana operators γ_n defined in Eq. (1.10),

$$H = \frac{\mu}{2}\sum_{n=1}^{N}(1 - i\gamma_{2n}\gamma_{2n-1}) + i\sum_{n=1}^{N-1}\left[\frac{(\Delta+t)}{2}\gamma_{2n+2}\gamma_{2n-1} + \frac{(\Delta-t)}{2}\gamma_{2n+1}\gamma_{2n}\right]. \tag{1.16}$$

For $t = -\Delta$, $\mu = 0$ the Hamiltonian simplifies to

$$H = \Delta\sum_{n=1}^{N-1} i\gamma_{2n+1}\gamma_{2n}. \tag{1.17}$$

The operators γ_1 and γ_{2N} do not appear in the Hamiltonian (1.17), and they commute with the Hamiltonian, i. e. $[\gamma_1, H] = [\gamma_{2N}, H] = 0$. These two unpaired Majorana operators define the *Majorana zero-modes*. They correspond to a fermion state $c = \frac{1}{2}(\gamma_1 + i\gamma_{2N})$ which splits over the two end points of the chain (see Fig. 1.4). In this topologically nontrivial case, the Hamiltonian has two degenerate ground states at zero energy, distinguished by the occupation number of the fermionic state. This degeneracy has been proposed by Kitaev as a way to store information in a quantum computer. Because the information is distributed over the two ends of the chain, it is believed to be less sensitive to external perturbations than information that is stored locally.

1.2.4 Experimental signatures

There exists a variety of experimental features that can serve as a "smoking gun" for the existence of Majorana zero-modes. The first experiments

focused on the zero-bias peak of the tunnelling conductance. Due to perfect Andreev reflection at the zero-mode, the zero-temperature, zero-voltage limit of the differential conductance is quantized to $2e^2/h$ [25]. In the experiment [19], see Fig.1.1, the zero-bias conductance peak is an order of magnitude smaller, presumbaly because of thermal averaging. This complicates the unambiguous interpretation of the experiment, because there are other mechanisms that could give a non-quantized zero-bias peak [26, 27]. (One such mechanism is discussed in Chapter 5 of this thesis.)

Another feature of Majorana zero-modes is the so called 4π-periodic Josephson effect [10, 24, 28]. The energy spectrum of a Josephson junction containing a pair of Majorana zero-modes, separated by a tunnel barrier, is 4π-periodic in the phase difference ϕ across the junction. This corresponds to a flux periodicity of h/e, twice the usual $h/2e$ periodicity. One can understand the change from $2e$ to e as a manifestation of the fact that a Majorana fermion is only half an electron.

1.2.5 Non-Abelian statistics

Unlike Majorana fermions, which have the usual fermionic statistics (a sign change of the wave function upon pairwise exchange), the exchange statistics of Majorana zero-modes is non-Abelian, it depends on the order of the exchange operations [7].

Quite generally, for Abelian statistics the exchange of a pair of indistinguishable particles multiplies the wave function by a phase factor, $\psi \mapsto \mathrm{e}^{i\theta}\psi$. The phase θ can be 0 (bosons), π (fermions) or any other value $\theta \in (0, \pi)$ (anyons). Different exchanges commute with each other.

For non-Abelian statistics the exchange operates on a manifold of degenerate states (all zero-modes are at $\varepsilon = 0$), mapping one state on another via a unitary transformation, $\psi \mapsto U\psi$. Because matrix multiplication does not commute, the order of the exchange operations matters. Specifically the exchange of two Majorana zero-modes i, j corresponds to an unitary operator $U(T_{ij})$ which is given by

$$U(T_{ij}) = \frac{1 - \gamma_i\gamma_j}{\sqrt{2}}, \quad U(T_{ij})^\dagger = U(T_{ij})^{-1} = \frac{1 + \gamma_i\gamma_j}{\sqrt{2}}. \tag{1.18}$$

The Majorana operators transform as follows:

$$\begin{aligned} U(T_{ij})\gamma_i U(T_{ij})^\dagger &= \gamma_j, \\ U(T_{ij})\gamma_j U(T_{ij})^\dagger &= -\gamma_i, \\ U(T_{ij})\gamma_k U(T_{ij})^\dagger &= \gamma_k \quad (k \neq i, j). \end{aligned} \tag{1.19}$$

If we take three Majorana zero-modes $\{\gamma_i, \gamma_j, \gamma_k\}$ the pairwise exchanges $i \leftrightarrow j$ and $j \leftrightarrow k$ do not commute, because the two operators $U(T_{ij}) = (1 - \gamma_i\gamma_j)/\sqrt{2}$ and $U(T_{jk}) = (1 - \gamma_j\gamma_k)/\sqrt{2}$ do not commute, i. e. the commutator $[U(T_{ij}), U(T_{jk})] = \gamma_i\gamma_k$ is non-zero. Such non-commuting sequence of pairwise exchanges is called "braiding".

Braiding of Majorana zero-modes is not sufficiently powerful to produce *all* logical operations, but a subset of operations can be obtained in this way [9]. Braiding is insensitive to local sources of decoherence, because it does not involve phase shifts as for ordinary unitary evolution of a quantum state. One says that the braiding operation has "topological protection". Quantum computations assisted by braiding operations are called topological quantum computations.

1.3 This thesis

1.3.1 Chapter 2

To explain the experimental results in InSb nanowires achieved by the Delft group [19], we investigate whether the appearance of a soft gap in the differential conductance can be reconciled with the existence of Majorana zero-modes. From our simulation and calculation, we conclude that the combination of weak disorder with a partial coverage of the wire by the superconductor does indeed give rise to a softening of the induced superconducting gap. We find that the soft gap does not prohibit the presence of Majorana zero-modes, supporting an interpretation of the observed zero-bias conductance peak in these terms. We also point out that the minimal gap in such a nanowire is very small, thus it severely limits the lifetime of a Majorana qubit.

1.3.2 Chapter 3

The quantum spin Hall effect is an analogue of the quantum Hall effect in a system where time-reversal symmetry is not broken by a magnetic

field [30–35]. The edge of a quantum spin Hall insulator has counterpropagating helical modes, with the direction of motion tied to the spin direction. As long as time-reversal symmetry is preserved, there can be no backscattering in the helical mode. When superconductivity is induced at the edge, a Majorana zero-mode is predicted to appear [10, 11]. The advantages of this system over the nanowire, are that the conduction happens in a single mode and that disorder cannot cause any backscattering. The disadvantage is that one cannot create an electrostatic barrier in this system, since the absence of backscattering prohibits that. A ferromagnetic insulator does form a tunnel barrier, but this material is experimentally inconvenient. As an alternative, we suggest a gate controllable metallic puddle with weak disorder and weak magnetic field to induce back scattering of the edge state. We show that the zero-bias peak from the Majorana zero-mode is hidden in a single conductance measurement, but is revealed upon averaging over gate voltages. Using this geometry as a building block, we design a flux-controlled circuit to perform a braiding operation.

1.3.3 Chapter 4

We continue our study of the quantum spin Hall effect, to explain a remarkable finding by the group from Rice University [36]: in InAs/GaSb quantum wells the helical edge conduction persists in perpendicular magnetic fields as large as 8 T, when we would expect strong backscattering from time-reversal symmetry breaking. We cannot quite explain the experimental data, but we do find an unusual phase diagram in our model calculation: The critical breakdown field for helical edge conduction splits into two fields with increasing disorder, an upper critical field for the transition into a quantum Hall insulator (supporting chiral edge conduction) and a lower critical field for the transition to bulk conduction in a quasi-metallic regime. The spatial separation of the inverted bands, typical for broken-gap InAs/GaSb quantum wells, is essential for the magnetic-field induced bulk conduction — there is no such regime in the HgTe quantum wells studied by the Würzburg group [34].

1.3.4 Chapter 5

The characteristic feature of the Delft experiment [19] is a resonant peak around zero bias-voltage V that does not split upon variation of a mag-

netic field B. In the $B - V$ plane the conductance peaks trace out an unusual Y-shaped profile, distinct from the more common X-shaped profile of peaks that meet and immediately split again. It is tempting to think that the absence of a splitting of the zero-bias conductance peak demonstrates unambiguously that the quasi-bound state is nondegenerate, hence Majorana. However, as found in Ref. [26], the Y-shaped conductance profile is generic for superconductors with broken spin-rotation symmetry and broken time-reversal symmetry, irrespective of the presence or absence of Majorana zero-modes. In this chapter we investigate the appearance of such "fake Majorana peaks" in the framework of random-matrix theory. We contrast the two ensembles with broken time-reversal symmetry, in the presence of spin-rotation symmetry (symmetry class C), or in its absence (class D). The poles of the scattering matrix in the complex plane, encoding the center and width of the resonance, are repelled from the imaginary axis in class C, but attracted to it in class D. This explains the appearance of Andreev resonances that are are pinned to the middle of the gap and produce a zero-bias conductance peak that does not split over a range of parameter values (Y-shaped profile).

1.3.5 Chapter 6

In this chapter, we demonstrate how the superconducting phase difference in a Josephson junction may be used to remove the Kramers degeneracy of the Andreev levels, producing a nondegenerate two-level system that can be used as a qubit for quantum information processing. The splitting is known to be small in two-terminal Josephson junctions, but when there are three or more terminals the splitting becomes comparable to the superconducting gap. Application of a phase difference can then cause the switch of the ground state fermion parity from even to odd, observed as a crossing of the Andreev levels at the Fermi energy. In essence, the multi-terminal Josephson junction realizes a "discrete vortex" in the junction, which may eventually be used to trap Majorana zero-modes.

Bibliography

[1] E. Majorana, Nuovo Cimento **5**, 171 (1937).

[2] F. Wilczek, Nature Physics **5**, 614 (2009).

[3] S. R. Elliott and M. Franz, arXiv:1403.4976.

[4] C. W. J. Beenakker, Phys. Rev. Lett. **112**, 070604 (2014).

[5] N. B. Kopnin and M. M. Salomaa, Phys. Rev. B **44**, 9667 (1991).

[6] G. E. Volovik, JETP Letters **70**, 609 (1999).

[7] N. Read and D. Green, Phys. Rev. B **61**, 10267 (2000).

[8] S. B. Bravyi and A. Yu. Kitaev, Ann. Phys. **298**, 210 (2002).

[9] C. Nayak, S. H. Simon, A. Stern, M. Freedman, and S. Das Sarma, Rev. Mod. Phys. **80**, 1083 (2008).

[10] L. Fu and C. L. Kane, Phys. Rev. Lett. **100**, 096407 (2008).

[11] L. Fu and C. L. Kane, Phys. Rev. B **79**, 161408(R) (2009).

[12] R. Lutchyn, J. Sau, and S. Das Sarma, Phys. Rev. Lett. **105**, 077001 (2010).

[13] Y. Oreg, G. Refael, and F. von Oppen, Phys. Rev. Lett. **105**, 177002 (2010).

[14] M. Z. Hasan and C. L. Kane, Rev. Mod. Phys. **82**, 3045 (2010).

[15] X.-L Qi and S. C. Zhang, Rev. Mod. Phys. **83**, 1057 (2011).

[16] J. Alicea, Rep. Prog. Phys. **75**, 076501 (2012).

[17] C. W. J. Beenakker, Ann. Rev. Cond. Mat. Phys. **4**, 113 (2013).

[18] J. Alicea and A. Stern, arXiv:1410.0359.

[19] V. Mourik, K. Zuo, S. M. Frolov, S. R. Plissard, E. P. A. M. Bakkers, and L. P. Kouwenhoven, Science **336**, 1003 (2012).

[20] M. T. Deng, C. L. Yu, G. Y. Huang, M Larsson, P. Caroff, and H. Q. Xu, Nano Lett. **12**, 6414 (2012).

[21] H. A. Nilsson, P. Samuelsson, P. Caroff, and H. Q. Xu, Nano Lett. **12**, 228 (2012).

[22] A. Das, Y. Ronen, Y. Most, Y. Oreg, M. Heiblum, and H. Shtrikman, Nature Phys. **8**, 887 (2012).

[23] S. Nadj-Perge, I. K. Drozdov, J. Li, H. Chen, S. Jeon, J. Seo, A. H. MacDonald, B. A. Bernevig, and A. Yazdani, Science **346**, 602 (2014).

[24] A. Yu. Kitaev, Phys.-Usp. **44**, 131 (2001).

[25] K. T. Law, P. A. Lee, and T. K. Ng, Phys. Rev. Lett. **103**, 237001 (2009).

[26] D. I. Pikulin, J. P. Dahlhaus, M. Wimmer, H. Schomerus, and C. W. J. Beenakker, New J. Phys. **14**, 125011 (2012).

[27] J. Liu, A. C. Potter, K. T. Law, and P. A. Lee, Phys. Rev. Lett. **109**, 267002 (2012).

[28] L. P. Rokhinson, X. Liu, and J. K. Furdyna, Nat. Phys. **8**, 795 (2012).

[29] A. Stern and N. H. Lindner, Science **339**, 1179 (2013).

[30] C. L. Kane and E. J. Mele, Phys. Rev. Lett. **95**, 226801 (2005).

[31] B. A. Bernevig and S. C. Zhang, Phys. Rev. Lett. **96**, 106802 (2006).

[32] B. A. Bernevig, T. L. Hughes and S. C. Zhang, Science **314**, 1757 (2006).

[33] C. X. Liu, T. L. Hughes, X. -L. Qi, K. Wang, and S. C. Zhang, Phys. Rev. Lett. **100**, 236601 (2008).

[34] M. König, S. Wiedmann, C. Brüne, A. Roth, H. Buhmann, L. W. Molenkamp, X. -L. Qi, and S. C. Zhang, Science, **318**, 5851 (2007).

[35] M. König, H. Buhmann, L. W. Molenkamp, T. L. Hughes, C. -X. Liu, X. -L. Qi, and S. C. Zhang, J. Phys. Soc. Jpn. **77**, 031007 (2008).

[36] L. Du, I. Knez, G. Sullivan, and R.-R. Du, arXiv:1306.1925

Chapter 2

Impact of the soft induced gap on the Majorana zero-modes in semiconducting nanowires

2.1 Introduction

In a recent paper Mourik *et al.* reported observing signatures of Majorana zero-modes in indium antimonide nanowires contacted by NbTiN superconductor [1] by implementing an earlier theoretical proposal [2, 3]. More specifically they have reported a zero bias peak in Andreev conductance appearing when magnetic field was applied parallel to the wire. Since creating and observing Majorana zero-modes is a long-standing challenge, this result together with follow-up experiments [4–6] has created a big interest both in the theoretical [7] and experimental communities [8].

The observations reported in Ref. 1 differ significantly from what is expected within a simple theoretical picture. In particular the appearance of the zero bias peak was not accompanied by the closing of the observed induced superconducting gap. The magnetic field at which the zero bias peak appeared was approximately a factor of two smaller than the expected value.

Perhaps the observed feature that is most hard to reconcile with existence of Majorana zero-modes is the fact that the tunneling conductance did not follow the prediction of BTK theory [9], and instead a soft gap was observed with tunneling conductance inside the gap roughly proportional to the bias voltage, or the excitation energy. Since Majorana

zero-modes are protected exactly by the superconducting gap, it is not clear whether they may appear without this protection.

The aim of our work is to figure out whether the observed soft gap may be due to low disorder in the nanowire and the presence of multiple one-dimensional bands. It is well known [10] that the broad distribution of dwell times in such integrable systems leads to a soft gap since different quasiparticles bounce off the superconductor with very different frequencies. Our conclusion is mixed: on one hand we indeed find that the multiband origin of the soft induced gap fits the observations reasonably well. If it is indeed the reason for appearance of the soft gap, this allows us to put an upper bound on the amount of disorder in the nanowire, and to conclude that disorder is not prohibitively strong to observe Majorana zero-modes. On the other hand, presence of bands with minute band gap diminishes greatly the topological protection of Majorana zero-modes and makes the nanowire implementations not directly suitable to observe the non-Abelian properties of Majorana zero-modes.

The layout of this chapter is as follows. In Sec. 2.2 we provide general considerations for the mechanism behind the induced gap. We discuss the methods we use in detail in Sec. 2.3. We describe the profile of the induced gap in Sec. 2.4, which is followed by the discussion of the relation between the soft gap and Majorana zero-modes in Sec. 2.5. We conclude in Sec. 2.6.

2.2 Possible origins of the soft gap

The superconducting hard gap in presence of time reversal symmetry is protected by Anderson's theorem [11], that shows that the gap size is not sensitive to disorder and spin-orbit interaction. There are several ways in which the Anderson theorem can be violated in the nanowire-superconductor hybrid structure.

First of all, the time reversal symmetry may be broken even in the absence of magnetic field due to the presence of magnetic impurities. Such impurities may create a fluctuating magnetic field that may suppress the superconducting gap [12]. This scenario requires the scale of the effective magnetic field created by the impurities to be tuned to the size of the superconducting gap, since otherwise either the effect of the impurities on the density of states is negligibly, or the gap completely

closes instead of acquiring a liner profile in the density of states.

The density of states may also become nonzero at low energies due to the thermal level broadening [13]. Applied to the typical experimental setup, this requires the electron temperature to be comparable to the induced superconducting gap $\sim 1K$, while most of the experiments are performed at a much lower temperature $\lesssim 100mK$, and resolve features of the much narrower width. Therefore we will focus on the low temperature regime.

Additionally, if the coupling between the normal metal and the superconductor is not weak, the differential conductance profile may get a scaling different from that of the density of states [9, 13]. Since the softness of the gap is observed to persist in the weak coupling regime $G \ll e^2/h$, we focus on the physical effects that directly modify the density of states in the nanowire.

In a hybrid system, the situation becomes more complicated, where one distinguishes the long junction junction regime when the Thouless energy $E_{\mathrm{Th}} \ll \Delta$ or the short junction regime $E_{\mathrm{Th}} \gg \Delta$. In the short junction regime most of the weight of the wave function of the Andreev states is inside the superconducting region, so that the Anderson theorem is fulfilled, and there is no modification of the BCS density of states. In the long junction regime, on the other hand, most of the weight of the Andreev state is in the normal region, so that the energy of each Andreev state is inverse of its dwell time in the normal region. Since the overall size of the observed induced gap is suppressed compared to the bulk gap in the corresponding superconductors, it is reasonable to assume that the long junction limit applies.

In order to generate a smooth profile of the overall density of states, a power law distribution of flight times towards the superconductor is required. This may be obtained in a diffusive system, with the mean free path much shorter than the distance to the superconductor [14]. Since the nanowires are nearly ballistic before depositing the superconductor, and since even the wave length in the nanowire is not much shorter than the wire diameter, this limit probably does not apply. On the other hand, when the mean free path is very long, such that the system becomes integrable due to the conservation of momentum along the wire, the soft superconducting gap may arise naturally from the appearance of the trajectories with very long flight times due to their momentum being almost parallel to the nanowire axis [15, 10] [see Fig. 2.1(b)]. In a

simplified two-dimensional setup the flight time and the corresponding energy of the Andreev states are given by:

$$T(p_\parallel) = \frac{2m^* d}{\sqrt{p_F^2 - p_\parallel^2}}, \quad E_{\text{gap}} = \frac{\pi\hbar}{2T(p_\parallel)}, \tag{2.1}$$

with m^* the effective carrier mass, d the wire diameter, p_F the Fermi momentum, and $p_\parallel$ the momentum along the wire. Integration of $\rho(E)$ over $p_\parallel$ yields a linearly vanishing density of states near $E = 0$.

We have given this intepretation of the apparent soft gap in terms of a simplified 2D model. The argument depends on the flight time of classical paths, and hence depends sensitively on geometry. Directly applying this quasiclassical formalism to the 3D geometry of the experiment would only be possible numerically. Instead, we will present a full quantum calculation of the induced gap in the 3D nanowire geometry below. Still, we will be able to explain the main observed features in terms of this quasiclassical argument.

2.3 Methods and system setup

We consider a semiconducting nanowire with spin-orbit coupling, assuming that the spin-orbit coupling is due to a electric field perpendicular to the substrate. The nanowire Hamiltonian then reads:

$$\mathcal{H} = \frac{\mathbf{p}^2}{2m^*} + \frac{\alpha}{\hbar}(\sigma_x p_y - \sigma_y p_x) + E_Z\sigma_x + V(x), \tag{2.2}$$

where α is a parameter denotes the Rashba spin-orbit coupling strength, and $E_Z = \frac{1}{2}g\mu_B B$ is the Zeeman energy due to a magnetic field B in the x-direction, and $V(x)$ is a potential, e.g. due to disorder. In InSb, the effective mass $m^* = 0.014m_e$ where m_e is the bare electron mass, and $g = 51$.

We describe the presence of the superconducting contact within the Bogoliubov-de Gennes formalism, so that the total Hamiltonian for the semiconductor and the superconducting contact is given as

$$H_{BdG} = \begin{pmatrix} \mathcal{H} & \Delta \\ \Delta & -\mathcal{T}\,\mathcal{H}\,\mathcal{T}^{-1} \end{pmatrix}. \tag{2.3}$$

Here Δ is the superconducting order parameter, which we set nonzero only in the superconducting contact. Superconductivity in the nanowire is then only induced through proximity. $\mathcal{T}$ is the time-reversal operator.

In order to make contact to experiment and take into account the effects of broadening to to finite coupling to leads or finite temperature, we compute the Andreev conductance. To do so, we use the scattering matrix formalism. The scattering matrix for Andreev reflection reads

$$r_A = \begin{pmatrix} r_{ee} & r_{eh} \\ r_{he} & r_{hh} \end{pmatrix} . \tag{2.4}$$

where the individual blocks are the scattering matrices for reflection between electrons (e) and holes (h), respectively. The Andreev conductance is then given as

$$G = \frac{e^2}{h} \mathrm{Tr} \left(\mathbf{1} - r_{ee} r_{ee}^\dagger + r_{he} r_{he}^\dagger \right) . \tag{2.5}$$

We compute the scattering matrix (2.4) numerically in a tight-binding approximation of Eq. (2.3) using Kwant [16]. The geometry of the simulated system is shown in Fig. 2.1(a). In particular, we consider a nanowire with length $2\mu m$ and diameter $100\,nm$ coated by layer of superconductor (blue shell in Fig. 2.1(a)), covering an angle 2ϕ of the nanowire.

In the tight-binding description of the superconductor, we use the same hopping matrix element $t = \hbar^2/2ma^2$ (where a is the lattice constant of the discretization) as in the nanowire, and set $\Delta = t$, to be in the limit of short coherence length as appropriate for the superconductor used in the experiment [1]. The hopping t_s between superconductor and semiconductor is used as a fit parameter controlling the induced gap.

The proximitized part of the nanowire is separated from the normal part of the nanowire by a $25\,nm$ wide, rectangular tunnel barrier (red region in Fig. 2.1(a)). We tune the tunnel barrier height such that the normal state conductance $0.6\,e^2/h$.

We include random on-site disorder drawn from the uniform distribution $[-U_0, U_0]$. This random on-site potential itself does not have a physical meaning (the fluctations of the potential are on the scale of the lattice constant a of the discretization). To assess the strength of the disorder, we characterize it by computing the mean free path in a wire without magnetic field or superconductor.

We can extract the mean free path numerically from the disorder-

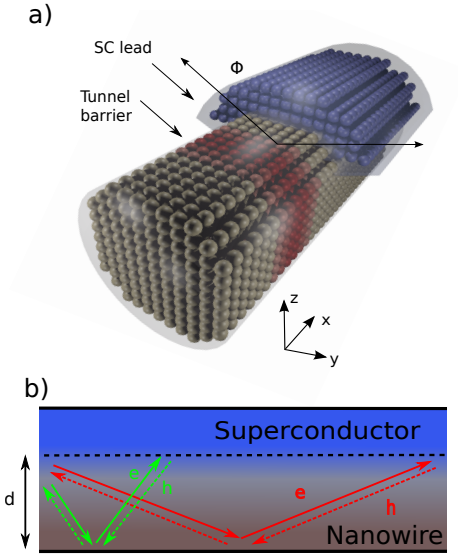

Figure 2.1. *a*) The layout of the system used in our study. The grey region indicates the nanowire, the blue shell the superconductor, and the red region shows the depleted part of the nanowire which forms the tunnel barrier. *b*) Schematic of paths for particles of different channels. The solid lines are trajectories of electrons and the dash lines of holes. The green lines indicates lower modes who have smaller parallel momentum thus shorter dwelling time and smaller and softer induced gaps. The red lines are for higher channel modes with larger parallel momentum and larger and harder induced gaps.

averaged conductance by fitting [17]

$$\langle G(\mu, U_0)\rangle = \frac{e^2}{h}\frac{N}{1+3L/4\xi_{\mathrm{MFP}}}, \tag{2.6}$$

where L is the length of the nanowire, and $\langle G\rangle$ the disorder averaged conductance.

The mean scattering time τcan also be computed from Fermi's golden rule, using the three-dimensional density of states of the nanowire bulk. We then find

$$\frac{1}{\tau} = \frac{a^3(2m^*)^{3/2}}{2\pi\hbar^4}\frac{1}{3}U_0^2\sqrt{\epsilon_F}, \tag{2.7}$$

where ϵ_F is the Fermi energy. The mean free path in our tight-binding

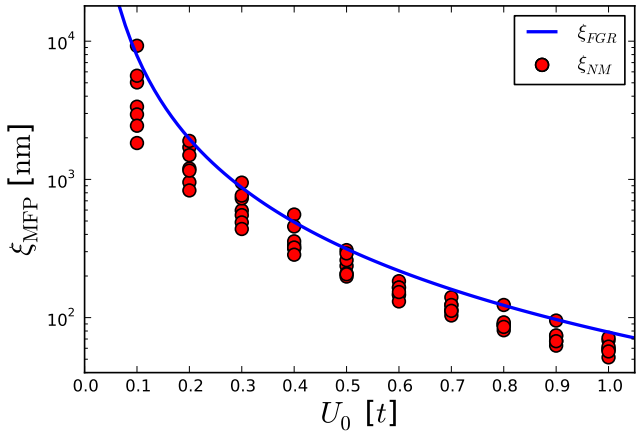

Figure 2.2. Mean free path ξ_{MFP} as a function of disorder strength U_0. Dots are numerically computed values for different values of chemical potential (corresponding to a range of 6–16 subbands) fitting disorder-averaged conductances for a range of nanowire lengths from 83 nm to 833 nm to Eq. (2.6). The solid line is the Fermi golden rule estimate from Eq. (2.8).

model from Fermi's golden rule is then given by

$$\xi_{\mathrm{MFP}} = v_F\,\tau = \frac{4\pi a}{\frac{1}{3}U_0^2/t^2} \tag{2.8}$$

In Fig. 2.2 we show both the numerically extracted mean free path as well as the prediction from Fermi's golden rule. Note that the latter does not account for the discrete subband structure of the nanowire, and correspondingly we observe a larger deviation from the numerical result for weak disorder, where subbands are mixed only little.

2.4 Gap softness

We first consider the induced superconducting gap in the nanowire in the absence of a magnetic field, $B = 0$. In this limit our general considerations relating classical paths to induced superconducting gaps are valid.

Since the induced gap depends inversely on the time between hits on the superconductor, we can expect the amount of surface being covered by the superconductor to have a large influence. In Fig. 2.3 we show

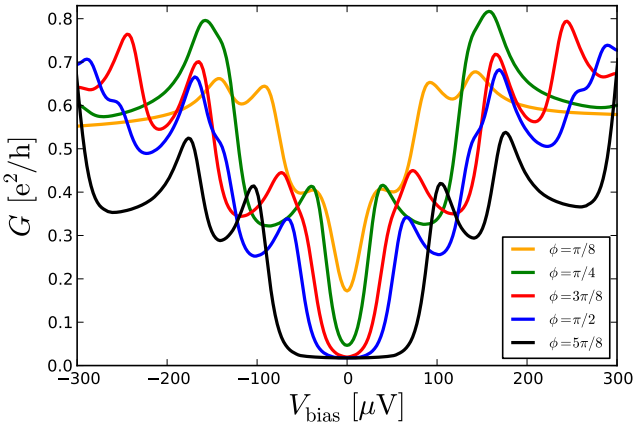

Figure 2.3. Influence of the coverage angle ϕ on the induced gap in the nanowire, as seen in the differential conductance G. Results are in the limit of a clean wire ($U_0 = 0$) and in the absence of a magnetic field ($B = 0$)

.

the differential conductance of the nanowire device as a function of bias voltage for different coverage angles ϕ of the superconductor.

A common feature for all coverage angles is that we observe not only a single superconducting gap, but instead a series of gaps, signaled by a series of coherence peaks with increasing bias voltage. We can attribute these to the different subbands that correspond to classical paths of different length, as argued above. The lowest subbands (with small transverse momentum) correspond to the smallest induced gaps, whereas the highest subbands (with a large transverse momentum) correspond to the largest induced gaps. In a clean system the conductances of the different modes simply add up. Thus we only see a strong suppression of the conductance within the smallest gap, whereas within the induced gap of the higher modes there is a finite conductance due to the above-gap conductance of the lower modes.

When increasing the coverage angle, we observe that each of the induced gaps increases monotonously. Again, this fits well with our expectations from the classical paths: For all modes the corresponding trajectories become shorter when the surface covered by the superconductor increases. A similar behavior is found when the coupling strength to the superconductor is changed (not shown here): When increasing the coupling strength, the probability of Andreev reflection is enhanced

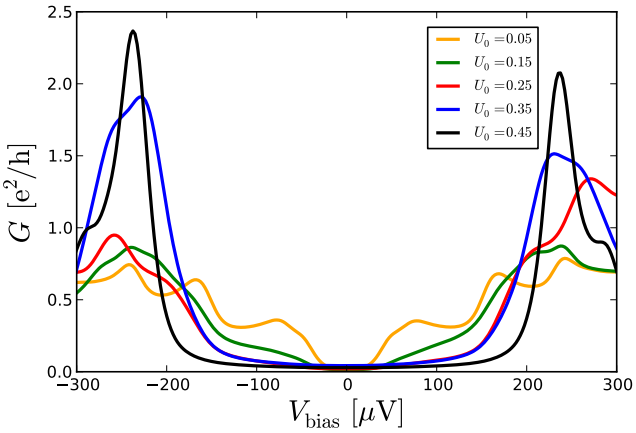

Figure 2.4. Influence of disorder on the observed gap in the conductance. Small disorder ($U_0 < 0.15$) reduces the observed coherence peaks and smoothens the observed gap. Larger disorder however leads eventually to a single hard gap. Results are for a coverage angle $\phi = 3\pi/8$, $t_s = t/2$ and zero magnetic field.

whereas the probability of normal reflection is reduced. This again leads to shorter trajectories and thus larger induced gaps for larger couplings.

The multi-mode nature of the nanowires thus leads naturally to a series of induced gaps, that manifest themselves in an increasing conductance until the bias voltage exceeds the largest induced gap. This is already reminiscent of the monotonously increasing sub-gap conductance in the experiment, if we identify the experimentally assigned gap with the largest induced gap in the highest subband. The main visual difference is the strong feature of a series coherence peaks in our numerics, that is absent in the experimental measurements. These strong coherence peaks for every subband are due to the fact that modes are globally well-defined in a clean system. Disorder will scatter between subbands and can thus have a large effect on the induced gaps.

For the remainder of the chapter we fix the coverage angle to $\phi = 3\pi/8$ in accordance with experiments [1]. We also fix $t_s = t/2$ to obtain a width of the apparent soft gap of 250 μeV as in the experiment, and continue to discuss the effects of disorder on the induced gap.

In Fig. 2.4 we show the dependence of the differential conductance on disorder strength. Weak disorder reduces the coherence peaks observed in the clean system due to scattering between subbands, and at $U_0 = 0.15$

only a smooth, soft gap is observed in the conductance, reminiscent of experiment. The presence of several modes in the nanowire together with weak scattering can thus explain the soft gap of the experiment completely.

For larger disorder strength, we instead find a transition to a single, hard gap. This is due to the fact that for strong scattering different modes are completely mixed, and the only remaining length scale in the problem is the mean free path. The latter is thus a natural cut-off for the maximum trajectory length and sets the value of the induced gap. The observation of a soft gap thus also sets an upper limit on the disorder present in the system. A comparison with Fig. 2.2 suggests a limit on the mean free path of order 1 μm. (It should be noted though that this estimate may depend on other details such as the potential drop across the nanowire.)

We note that the phenomenology observed here, a transition from a smooth gap to a hard gap with increasing disorder was described before for the case of metallic mesoscopic systems [14], where the semiclassical theory is expected to hold due to the large number of modes. Still, the semiclassical theory continues to describes the general trends in the semiconductor devices. Particular to our results is the prediction that in a clean nanowire system the different subbands would manifest themselves in series of coherence peaks. These should be observable in experiment if nanowire quality is improved.

2.5 Majorana zero-modes in a soft gap

Having established a plausible mechanism for an apparently soft gap in a proximitized nanowire, we now focus on the case of finite magnetic field, and in particular, Majorana zero-modes.

In a strictly one-dimensional wire a topological state with Majorana zero-modes is reached when [2, 3],

$$E_Z > \sqrt{\Delta^2 + \mu^2}\,. \tag{2.9}$$

In multi-band wires this condition still holds, provided that μ is replaced by $\mu - E_n$, where E_n is the band edge of the n-th subband [18]. In nanowires as typically used in experiments, the subband spacing is typically much larger than the Zeeman energy [19]. In this limit, only the

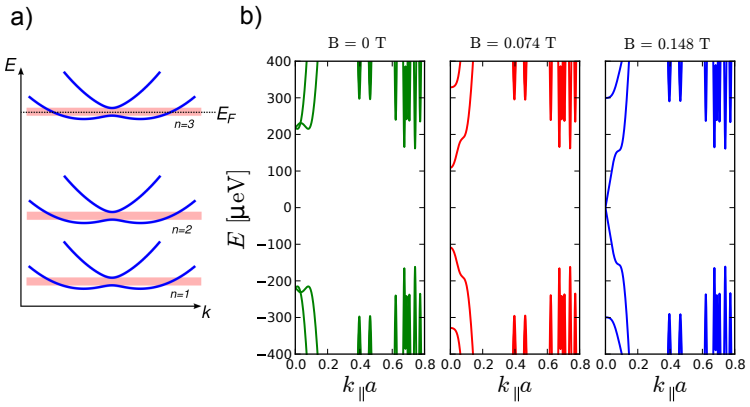

Figure 2.5. Majorana zero-modes in multi-band nanowires. (a) Schematic band structure of a multi-band nanowire with Rashba spin-orbit coupling in a magnetic field. A topological phase is reached if the Fermi energy E_F is tuned into the Zeeman gap of a subband; for a subband spacing larger than the Zeeman splitting this is only possible for the highest subband (with the largest confinement energy). (b) Band structure of proximitized nanowires for different values of the magnetic field. Results are for a coverage angle $\phi = 3\pi/8$ and $t_s = t/2$.

subband closest to the Fermi energy can be tuned into a topological state and host Majorana zero-modes [20, 21], as illustrated in Fig. 2.5(a) – the remainder of the subbands remains trivial.

The subband hosting an Majorana zero-mode hence has a large transverse momentum (the band edge being close to the Fermi energy), and hence a large induced gap. Hence, the Majorana zero-mode in proximitized nanowires are governed by the larger gap scale associated with the soft gap (in contrast to the smallest induced gaps of the lowest subbands). In particular, the threshold magnetic field for obtaining a topological state will be governed by this energy scale. This is in agreement with experiment [1], that have interpreted the largest energy scale of the soft gap as the induced gap Δ of the one-dimensional model Majorana theories [2, 3].

Figs. 2.5(b) show the band structure of a proximitized wire for increasing magnetic field. As expected from the previous arguments, only the highest mode (with the largest transverse momentum and the smallest longitudinal momentum k) shows a topological phase transition around

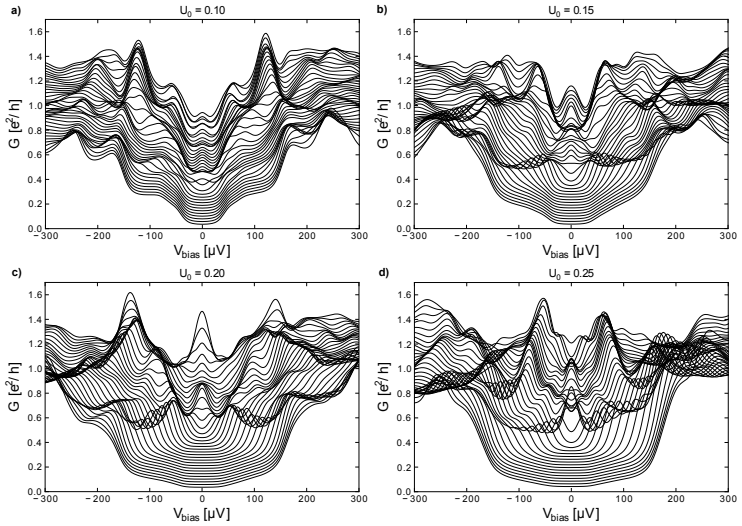

Figure 2.6. Andreev conductance of a proximitized nanowire for different disorder strengths ((a)-(d)) and different magnetic fields. Magnetic field is varied from $0 - 0.53\,\mathrm{T}$ and curves for different magnetic field are shifted vertically for clarity. Results are for a coverage angle $\phi = 3\pi/8$ and $t_s = t/2$.

$B = 0.15\,\mathrm{T}$. In fact, it is only this mode that shows an appreciable magnetic field dependence at all: All other subbands have a large longitudinal wave vector k_F and the spin-orbit energy $\alpha k_F \gg E_Z$, so that the induced gap for these modes is preserved in a magnetic field.

Hence, we find that in a clean wire the topological phase transition involves a single subband only, whereas the remainder of the modes forms an magnetic-field independent background. We can thus expect a similar phenomenology in the transport as was discussed for a constant induced gap common to all modes [20, 21], i.e. the appearance of a zero-bias peak in a background of a nearly magnetic-field independent gap and with a low visibility of the gap closing at the topological phase transition. The main difference to this previous work is that we now find the zero bias peak in apparently soft gap.

This expectation is confirmed by numerical calculations. In Fig. 2.6(a) we show the numerically calculated Andreev conductance for a range of magnetic field for weak disorder. In this case indeed the zero-bias peak appears without the topological phase transition visible as a gap closing. In addition, the series of induced gaps is visible as a constant background,

independent of magnetic field, and the remnants of the coherence peaks is visible as a series of nearly magnetic-field independent peaks at different bias voltages. We predict that these should be also visible in experiment as nanowire quality improves.

When disorder is increased, the visibility of the coherence peaks vanishes, and the gap is softened even more (Fig. 2.6(b)). In this case also the visibility of the gap closing at the topological transition increases, though the degree of softness and the onset of a visible gap closing depend very much on the details of the disorder and the barrier, i.e. a soft gap does not automatically imply that the gap closing should be visible. When disorder is increased more (Figs. 2.6(c),(d)), the induced gap becomes hard, but is also more strongly affected already by weak magnetic fields. In this case the superconducting gap starts to close at similar field strength required for the Majorana zero-mode to form. For even stronger disorder we find the gap to close completely with a number of low-energy states forming a large zero-bias peak as described in [22].

2.6 Conclusion

Our main finding is that a multichannel nanowire with limited scattering naturally exhibits an apparently soft gap. This is due to different induced superconducting gaps in each of the different channels. Disorder mixes subbands and ultimately leads to a single, hard induced gap. The observation of a soft gap thus may pose an upper limit on the scattering in nanowires.

The appearance of Majorana zero-modes is not affected significantly by the apparently soft gap. In fact, Majorana zero-modes are governed by the largest induced gap in the nanowire - this is advantageous for their observation as the corresponding coherence length of the topological gap scales inversely with the induced s-wave gap. A shorter coherence length protects Majorana zero-modes from disorder and separates the Majorana zero-modes at the two ends of the nanowire. On the other hand, the presence of the small induced gaps constituting the soft gap in the nanowire implies a very much smaller energy scale for other quasiparticles in the system. This may be a serious obstacle for observing the braiding statistics of Majorana zero-modes.

Our proposed mechanism for the soft gap has consequences that can be tested experimentally: First, we predict that in clean nanowires the An-

dreev conductance exhibits a series of nearly magnetic-field independent peaks corresponding to the induced gaps in the different subbands. Second, we predict that due to the small energy scale of the smallest induced gap there should be a significant normal transconductance between the two ends of the nanowire.

Bibliography

[1] V. Mourik, K. Zuo, S. M. Frolov, S. R. Plissard, E. P. A. M. Bakkers, and L. P. Kouwenhoven, Science **336**, 1003 (2012).

[2] R. M. Lutchyn, J. D. Sau, and S. Das Sarma, Phys. Rev. Lett. **105**, 077001 (2010).

[3] Y. Oreg, G. Refael, and F. von Oppen, Phys. Rev. Lett. **105**, 177002 (2010).

[4] M. T. Deng, C. L. Yu, G. Y. Huang, M Larsson, P. Caroff, and H. Q. Xu, Nano Lett. **12**, 6414 (2012).

[5] A. Das, Y. Ronen, Y. Most, Y. Oreg, M. Heiblum, and H. Shtrikman, Nature Phys. **8**, 887 (2012).

[6] L. P. Rokhinson, X. Liu, and J. K. Furdyna, Nat. Phys. **8**, 795 (2012).

[7] D. I. Pikulin, J. P. Dahlhaus, M. Wimmer, H. Schomerus, and C. W. J. Beenakker, New J. Phys. **14**, 125011 (2012).

[8] H. O. H. Churchill, V. Fatemi, K. Grove-Rasmussen, M. T. Deng, P. Caroff, H. Q. Xu, and C. M. Marcus, Phys. Rev. B **87**, 241401 (2013).

[9] G. E. Blonder, M. Tinkham, and T. M. Klapwijk, Phys. Rev. B **25**, 4515 (1982).

[10] P. G. de Gennes and D. Saint-James, Phys. Lett. **4**, 151 (1963).

[11] P. W. Anderson, J. Phys. Chem. Solids **11**, 26 (1959).

[12] S. Takei, B. M. Fregoso, H.-Y. Hui, A. M. Lobos, and S. Das Sarma, Phys. Rev. Lett. **110**, 186803 (2013).

[13] T. D. Stanescu, R. M. Lutchyn, and S. Das Sarma, Phys. Rev. B **90**, 085302 (2014).

[14] S. Pilgram, W. Belzig, and C. Bruder, Phys. Rev. B **62**, 12462 (2000).

[15] C. W. J. Beenakker, Lect. Notes. Phys. **667**, 131 (2005).

[16] C. W. Groth, M. Wimmer, A. R. Akhmerov, and X. Waintal, New. J. Phys. **106**, 127001 (2001).

[17] C. W. J. Beenakker, Rev. Mod. Phys. **69**, 731 (1997).

[18] R. Lutchyn, T. Stanescu, and S. Das Sarma, Phys. Rev. Lett. **106**, 127001 (2011).

[19] I. van Weperen, S. R. Plissard, E. P. A. M. Bakkers, S. M. Frolov, and L. P. Kouwenhoven, Nano Lett. **13**, 387 (2013).

[20] T. Stanescu, S. Tewari, J. Sau, and S. Das Sarma, Phys. Rev. Lett. **109**, 266402 (2012).

[21] F. Pientka, G. Kells, A. Romito, P. Brouwer, and F. von Oppen, Phys. Rev. Lett. **109**, 227006 (2012).

[22] J. Liu, A. C. Potter, K. T. Law, and P. A. Lee, Phys. Rev. Lett. **109**, 267002 (2012).

Chapter 3

Proposal for the detection and braiding of Majorana fermions in a quantum spin Hall insulator

3.1 Introduction

Topological insulators in proximity to a superconductor have been predicted [1] to support Majorana zero-modes: midgap states with identical creation and annihilation operators and non-Abelian braiding statistics [2, 3], that are presently under intense scrutiny [4]. The conducting edge of a quantum spin Hall (QSH) insulator seems like an ideal system to search for these elusive particles in a transport experiment [5, 6]: Only a single mode propagates in each direction along the edge, unaffected by disorder since backscattering of these helical modes is forbidden by time-reversal symmetry [7]. The QSH edge is thus immune for the multi-mode and disorder effects that complicate the Majorana-fermion interpretation of transport experiments in semiconductor nanowires [8, 9].

Andreev reflection at a superconducting interface has been reported in an InAs/GaSb quantum well [10], which is a QSH insulator because of a band inversion and the appearance of edge states connecting conduction and valence bands [11]. Similar experiments can be tried in HgTe/CdTe quantum wells, where the QSH effect was first discovered [12, 13]. We

expect a Majorana fermion to be present in these systems, delocalized along the edge connecting a normal and superconducting contact, but without a distinctive resonance in the electrical conductance. Andreev reflection of a helical edge mode doubles the current at all energies inside the band gap, so each edge contributes $2e^2/h$ to the differential conductance irrespective of any midgap states.

Here we present a method to restore the sensitivity of the conductance to the zero-mode resonance, by trapping the Majorana fermion near the superconducting interface. Only a minor modification of the existing experimental setup [10] is needed, essentially only a gate electrode at one of the edges, to locally push the conduction band through the Fermi level. (See Fig. 3.1.) The area under the gate then forms a two-dimensional metallic region, connected to the superconductor by the helical edge mode. Backscattering at this Andreev quantum dot in a weak magnetic field (one flux quantum or less through the dot) provides for an electrostatically tunable confinement of Majorana fermions. We discuss the detection of Majoranas as a short-term application, and braiding as a longer term perspective.

3.2 Proposal for detection

There exists a variety of phase coherent backscattering mechanisms for helical edge modes [14–20], based on different methods of time-reversal symmetry breaking to open a minigap in the edge state spectrum. A locally opened minigap forms a tunnel barrier for the edge modes and two tunnel barriers in series form a quantum dot at the QSH edge [19]. For a robust Majorana resonance it is advantageous to have a ballistic coupling rather than a tunnel coupling to the superconductor, so we form a quantum dot by placing two ballistic point contacts in series — without opening an excitation gap at the Fermi level.

The geometry, sketched in Fig. 3.1, can be seen as a gate-controlled realization of the puddles of metallic conduction that may occur naturally near the QSH edge [21–23]. An electron entering the metallic area under the gate from one side can be either transmitted to the other side or reflected back to the same side, with amplitudes contained in the 2×2 unitary scattering matrix $S(\varepsilon)$, dependent on the energy ε relative to the Fermi level. Time reversal symmetry requires an antisymmetric scattering matrix [24], $S_{nm} = -S_{mn}$, so the reflection amplitudes on the diagonal

are necessarily zero and the gate has no effect on the conductance.

A perpendicular magnetic field B effectively removes this constraint, once the flux through the gate is of the order of a flux quantum h/e. The electronic scattering matrix then has the four-parameter form

$$\begin{aligned} S &= \begin{pmatrix} r' & t' \\ t & r \end{pmatrix} = e^{i\phi_1\sigma_0} e^{i\phi_2\sigma_z} e^{i\gamma\sigma_y} e^{i\phi_3\sigma_z}, \\ \gamma &\in [0, \pi/2), \quad \phi_n \in [0, 2\pi), \quad n = 1, 2, 3. \end{aligned} \tag{3.1}$$

We have introduced Pauli spin matrices σ_x, σ_z, with σ_0 the 2×2 unit matrix.

If the scattering in the quantum dot is chaotic, the matrix S is uniformly distributed among all 2×2 unitary matrices. The Haar measure on the unitary group gives the probability distribution

$$P(\gamma, \phi_1, \phi_2, \phi_3) = (2\pi)^{-3} \sin 2\gamma, \tag{3.2}$$

representing the circular unitary ensemble (CUE) of random-matrix theory [25]. This produces a transmission probability $T = |t|^2 = \sin^2 \gamma$ that is *uniformly* distributed between zero and one [26, 27]. Different realizations of the ensemble, with different $T \in [0, 1]$, can be reached by varying the gate voltage, so that the quantum dot in a magnetic field functions as a tunable transmitter for the helical edge channels.

We now use this quantum dot as an energy-sensitive detector of the presence of a Majorana zero-mode at the interface with a superconductor. To explain how the energy sensitivity appears, we follow the usual procedure [25] of combining the electronic scattering matrix $S(\varepsilon)$, the hole scattering matrix $S^*(-\varepsilon)$, and the Andreev reflection matrix

$$r_{\mathrm{A}} = \alpha \tau_y, \quad \alpha = \sqrt{1 - (\varepsilon/\Delta_0)^2} + i\varepsilon/\Delta_0. \tag{3.3}$$

The Pauli matrix τ_y acts on the electron-hole degree of freedom and Δ_0 is the superconducting gap. An electron incident on the quantum dot along a helical edge state is reflected back as a hole with probability

$$R_{he}(\varepsilon) = \frac{T(\varepsilon) T(-\varepsilon)}{|1 - \alpha^2(\varepsilon) r(\varepsilon) r^*(-\varepsilon)|^2}. \tag{3.4}$$

At the Fermi level $\varepsilon = 0$ one has $\alpha = 1$ and $rr^* = 1 - T$, hence $R_{he} = 1$ irrespective of the transmission probability T through the quantum dot.

This is the Majorana resonance [28]. Away from the Fermi level the resonance has (for $T \ll 1$) a Lorentzian decay $\propto [1 + (\varepsilon/\Gamma)^2]^{-1}$, of width $\Gamma = T\delta_{\rm dot}/4\pi$ set by the average level spacing $\delta_{\rm dot}$ of the quantum dot.

The differential conductance $G = dI/dV$, at bias voltages $|V| < \Delta_0/e$ and in the zero-temperature limit, directly measures the probability (3.4):

$$G/G_0 = 2 + 2R_{he}(eV), \quad G_0 = e^2/h. \tag{3.5}$$

The two contributions to the conductance correspond to the two edges connecting the normal and superconducting contact: The edge containing the quantum dot contributes $2e^2/h \times R_{he}$, while the other edge remains unperturbed and contributes the full $2e^2/h$ — for sufficiently small B that the helical edge state remains gapless.

The ensemble averaged conductance $\langle G\rangle$ has a peak value of $4G_0$ at $V = 0$, above an off-resonant baseline $G_{\rm base}$ that we calculate as follows. We may assume $\delta_{\rm dot} \ll \Delta_0$, so we keep $\alpha = 1$. We treat the off-resonant scattering amplitudes at $\pm\varepsilon$ as statistically independent random variables in the CUE, distributed according to Eq. (3.2). Substitution of the parameterization (3.1) into Eq. (3.4) gives, upon averaging,

$$\begin{aligned} G_{\rm base}/G_0 &= 2 + 2\int_0^{\pi/2} d\gamma_+ \int_0^{\pi/2} d\gamma_- \, \sin 2\gamma_+ \sin 2\gamma_- \\ &\quad \times \int_0^{2\pi} \frac{d\phi}{2\pi} \frac{\sin^2\gamma_+ \sin^2\gamma_-}{|1 - \cos\gamma_+ \cos\gamma_- e^{i\phi}|^2} \\ &= \tfrac{2}{3}\pi^2 - 4 \approx 2.58. \end{aligned} \tag{3.6}$$

A similar calculation gives the *triangular* line shape of $\langle G(V)\rangle$ as an average over the Lorentzian line shape of $G(V)$,

$$\begin{aligned} \langle G(V)\rangle - G_{\rm base} &\propto \int_0^1 dT \, [1 + (4\pi eV/T\delta_{\rm dot})^2]^{-1} \\ &= 1 - (4\pi eV/\delta_{\rm dot}) \arctan(\delta_{\rm dot}/4\pi eV) \\ &= 1 - 2\pi^2 e|V|/\delta_{\rm dot} + \mathcal{O}(V^2). \end{aligned} \tag{3.7}$$

To test these analytical predictions, we have performed numerical simulations of a model Hamiltonian for an InAs/GaSb quantum well [11, 10, 29–31]. Results are shown in Fig. 3.2 and fully confirm our expectations: Without the quantum dot the Majorana resonance remains hidden in the background conductance (dashed curve in Fig.

3.2a), demonstrating that the 0.1 T applied field is weak enough to cause no appreciable backscattering of the helical edge states. We then create a 200 nm × 200 nm quantum dot, as in Fig. 3.1, by applying a gate voltage. This suppresses the background conductance, revealing the Majorana resonance at $V = 0$ (solid curves). Disorder averaging removes all resonances from Andreev levels at $V \neq 0$, so that the Majorana resonance stands out above the baseline conductance G_{base}, in very good agreement with the calculated value (3.6). The triangular line shape of the average conductance is also confirmed by the simulations (Fig. 3.2b).

The ensemble average in Fig. 3.2 is an average over disorder realizations. As is well known from quantum dot experiments [32, 33], statistically equivalent ensembles may be generated for a fixed disorder potential by varying the gate voltage, which is more practical from an experimental point of view. In Fig. 3.3 we show a computer simulation performed in this way. To reduce the sensitivity to thermal averaging, we took a smaller (100 nm × 100 nm) quantum dot, keeping the magnetic field at 0.1 T. The simulation shows that the Majorana resonance remains clearly visible above the background conductance at temperatures of 100 mK.

3.3 Proposal for braiding

So much for the detection of Majorana zero-modes. In the final part of this chapter, we take a longer term perspective and present a geometry that allows for the braiding of pairs of Majorana fermions, for the demonstration of the predicted non-Abelian statistics [3]. While the quantum spin Hall edge seems ideally suited for the detection of Majorana zero-modes, its one-dimensionality prevents the exchange of adjacent Majoranas. What is needed is a Y- or T-junction of superconductors to perform the "three-point turn" introduced by Alicea et al. [34] and implemented in a variety of braiding proposals for a network of nanowires [35–38].

In Fig. 3.4a we show how a constriction in the quantum spin Hall insulator can be used to achieve the same functionality as a crossing of nanowires. The constriction couples the helical edge states on opposite edges by tunneling, which is effective if it is narrower than the decay length of the edge states (100 nm or smaller). The coupling may be increased, if needed, by gating the constriction region into the conduction

band. Three of the four edges leading into the constriction are gapped by a superconducting island. The fourth edge contains one of the quantum dots discussed earlier, tuned to a gate voltage interval of minimal transmission $T \ll 1$.

Let us check that the constriction traps a Majorana zero-mode. Helical edge states incident on the constriction from the three superconductors have reflection amplitudes that are contained in a 3×3 reflection matrix $r(\varepsilon)$. Neglecting transmission throught the quantum dot, this is a unitary matrix. (A nonzero T will give a finite width to the zero mode.) A bound state in the constriction at energy ε is a solution of the determinantal equation [39]

$$\mathrm{Det}\,[1 - \alpha^2 \Lambda r(\varepsilon) \Lambda^* r^*(-\varepsilon)] = 0, \tag{3.8}$$

with $\Lambda = \mathrm{diag}\,(e^{i\phi_1}, e^{i\phi_2}, e^{i\phi_3})$ a diagonal matrix containing the phase ϕ_n of the order parameter on the n-th superconductor. Since $\alpha(0) = 1$, see Eq. (3.3), the condition for a zero mode is that the matrix uu^*, with $u \equiv \Lambda r(0)$, has an eigenvalue equal to $+1$. The eigenvalues of uu^* come in complex conjugate pairs $e^{\pm i\psi}$. An unpaired eigenvalue at -1 is forbidden by $\mathrm{Det}\, uu^* = 1$, but an unpaired eigenvalue at $+1$ is allowed and in fact necessary when the dimensionality of u is odd — as it is here.

In Fig. 3.4b,c we combine two constrictions in π-shaped circuit, to perform the braiding protocol of Ref. [38]. There are six Majorana fermions, one at each constriction and four more trapped by quantum dots along the quantum spin Hall edge. Adjacent Majorana operators $\gamma_m, \gamma_{m'}$, for example γ_B and γ_E, are coupled by the charging energy E_C of the intermediate superconducting island S_n through the Hamiltonian [36]

$$H_n = iU_n \gamma_m \gamma_{m'}, \;\; U_n \propto \exp\left[-\sqrt{8E_\mathrm{J}(\Phi_n)/E_\mathrm{C}}\right], \tag{3.9}$$

This coupling can be switched on and off by adjusting the Josephson energy $E_\mathrm{J} = E_0 \cos(e\Phi/\hbar)$ of the superconducting island, via the magnetic flux Φ through a split Josephson junction that connects the island to a superconducting ground.

As worked out in Refs. [35, 36], the alternating coupling and decoupling of adjacent Majoranas has the effect of exchanging them: One effectively moves the Majorana at B through the T-junction towards F, followed by $C \mapsto B$ and finally $F \mapsto C$ completes the exchange of B and C. If this exchange is repeated, one ends up with the original configuration of Majoranas, but in an orthogonal state: The fermion parity of S_4 has

switched between even and odd. This signature of non-Abelian statistics can be measured as described in Ref. [38], as a shift in the resonance frequency of a superconducting transmission line containing the circuit.

In conclusion, we have shown how the helical edge state in a quantum spin Hall insulator may be used as a single-channel, disorder-insensitive alternative to semiconductor nanowires, for the detection and braiding of Majorana fermions. For all we know, the experiments on InAs/GaSb quantum wells [10] may already have produced the predicted Majorana zero-modes [1], but since the $4e^2/h$ conductance resonance is hidden in the $4e^2/h$ off-resonant background there is no way to tell. The quantum dot geometry proposed here lowers the average background to about $2.6\,e^2/h$, allowing for the emergence of the Majorana resonance. This seems to be an experiment that is fully within reach of existing devices, requiring only the addition of a nanostructured gate electrode and the application of a weak magnetic field. As a longer-term perspective, we have shown how a constriction in the quantum spin Hall insulator can reproduce the functionality of a nanowire T-junction, required for braiding and for the demonstration of non-Abelian statistics.

3.4 Appendix: Description of the numerical simulations

Our numerical simulations are based on the four-band Hamiltonian of an InAs/GaSb quantum well [12, 11], which in zero magnetic field takes the form

$$\mathcal{H}(\boldsymbol{k}) = \begin{pmatrix} H_0(\boldsymbol{k}) & H_1(\boldsymbol{k}) \\ -H_1^*(-\boldsymbol{k}) & H_0^*(-\boldsymbol{k}) \end{pmatrix}, \tag{3.10}$$

as a function of wave vector $\boldsymbol{k} = (k_x, k_y)$ in the x-y plane of the semiconductor layers. The block structure refers to the spin degree of freedom, while each block itself has a 2×2 matrix structure that refers to the (s, p) orbital degree of freedom.

The diagonal block describes the hybridization of the s and p orbitals,

$$H_0 = \begin{pmatrix} U + b_0 - b_+k^2 & b_3k_+ \\ b_3k_- & U - b_0 - b_-k^2 \end{pmatrix}, \tag{3.11}$$

with $k^2 = k_x^2 + k_y^2$, $k_\pm = k_x \pm ik_y$, and $b_\pm = b_1 \pm b_2$. We have included an electrostatic potential U, to account for the effects of a gate electrode.

$b_0 = -\ 0.0078$ eV	$c_0 = \ \ 0.0002$ eV
$b_1 = -\ 5.8$ eV·Å^2	$c_1 = \ \ 0.00066$ eV·Å
$b_2 = -66.0$ eV·Å^2	$c_2 = \ \ 0.0006$ eV·Å
$b_3 = \ \ 0.37$ eV·Å	$c_3 = -0.07$ eV·Å

Table 3.1. Parameters of the four-band Hamiltonian (3.10), representative for a heterostructure consisting of 10 nm InAs and 10 nm GaSb layers, sandwiched between AlSb barriers [29].

The off-diagonal block describes the spin-orbit coupling by inversion asymmetry (Rashba and Dresselhaus effects),

$$H_1(\boldsymbol{k}) = \begin{pmatrix} c_1 k_+ + i c_3 k_- & -c_0 \\ c_0 & c_2 k_- \end{pmatrix}. \tag{3.12}$$

to first order in k. The parameter values we used in our simulations, taken from Ref. [29], are listed in Table I.

Time reversal symmetry is expressed by

$$\mathcal{H}(\boldsymbol{k}) = \sigma_y \mathcal{H}^*(-\boldsymbol{k})\sigma_y, \tag{3.13}$$

where the Pauli matrix σ_y acts on the spin blocks. A perpendicular magnetic field $\boldsymbol{B} = (0, 0, B)$ breaks time reversal symmetry, via an orbital and a Zeeman effect. The orbital effect is accounted for by the substitution $\boldsymbol{k} \mapsto \boldsymbol{k} - (e/\hbar)\boldsymbol{A}$, with vector potential $\boldsymbol{A} = (0, Bx, 0)$. The Zeeman energy $g\mu_{\mathrm{B}} B\sigma_z$ is a negligibly small effect in the weak magnetic fields $B \approx 0.1\,T$ considered here, so we do not include it.

The effect of a superconducting contact is introduced via the BdG Hamiltonian,

$$H_{\mathrm{BdG}} = \begin{pmatrix} \mathcal{H}[\boldsymbol{k} - (e/\hbar)\boldsymbol{A}] & \Delta \\ \Delta^\dagger & -\sigma_y \mathcal{H}^*[-\boldsymbol{k} - (e/\hbar)\boldsymbol{A}]\sigma_y \end{pmatrix}. \tag{3.14}$$

The blocks of H_{BdG} refer to the (e, h) electron-hole degree of freedom, coupled by the pair potential Δ induced by the superconducting contact. Electron-hole symmetry is expressed by

$$H_{\mathrm{BdG}}(\boldsymbol{k}) = -(\sigma_y \otimes \tau_y) H^*_{\mathrm{BdG}}(-\boldsymbol{k})(\sigma_y \otimes \tau_y), \tag{3.15}$$

where the Pauli matrix τ_y acts on the electron-hole blocks. A spin-singlet s-wave proximity effect may still couple the s and p orbitals of the quantum well [30], without breaking either electron-hole or time-reversal symmetry, but for simplicity here we take a scalar Δ.

For the numerical simulations we discretize the Hamiltonian (3.14) on a square lattice (lattice constant $a = 10\,\mathrm{nm}$) in the geometry shown to scale in Fig. 3.1. We set $\Delta = 1\,\mathrm{meV}$ in the superconducting contact and zero elsewhere. The effect of the gate electrode is modeled by an offset U_{gate} of the electrostatic potential in the area under the gate. Disorder in the quantum well is modeled on the lattice by a random on-site potential U_{disorder}, uniformly distributed in the interval $(-5\,\mathrm{meV}, +5\,\mathrm{meV})$. The magnetic field in the quantum well and the normal-metal contact is fixed at $B = 0.103\,\mathrm{T}$, corresponding to one flux quantum h/e through an area of size $200\,\mathrm{nm} \times 200\,\mathrm{nm}$. Inside the superconducting contact we set $B = 0$, ignoring the penetration of flux in magnetic vortices.

At excitation energies $|\varepsilon| < \Delta$ the electrons and holes incident on the superconductor are fully reflected. The reflection amplitudes are contained in an 8×8 unitary reflection matrix. The 4×4 Andreev reflection block $r_{he}(\varepsilon)$ gives the differential conductance at zero temperature,

$$G(V,0) = \frac{2e^2}{h} \mathrm{Tr}\, r_{he}(eV) r_{he}^\dagger(eV). \tag{3.16}$$

The corresponding result at finite temperature T_0 follows upon integration,

$$\begin{aligned} G(V,T_0) &= -\int_{-\infty}^{\infty} d\varepsilon\, G(\varepsilon/e,0) \frac{\partial f}{\partial \varepsilon}, \\ f(\varepsilon,V,T_0) &= \frac{1}{1+\exp[(\varepsilon - eV)/k_{\mathrm{B}}T_0]}. \end{aligned} \tag{3.17}$$

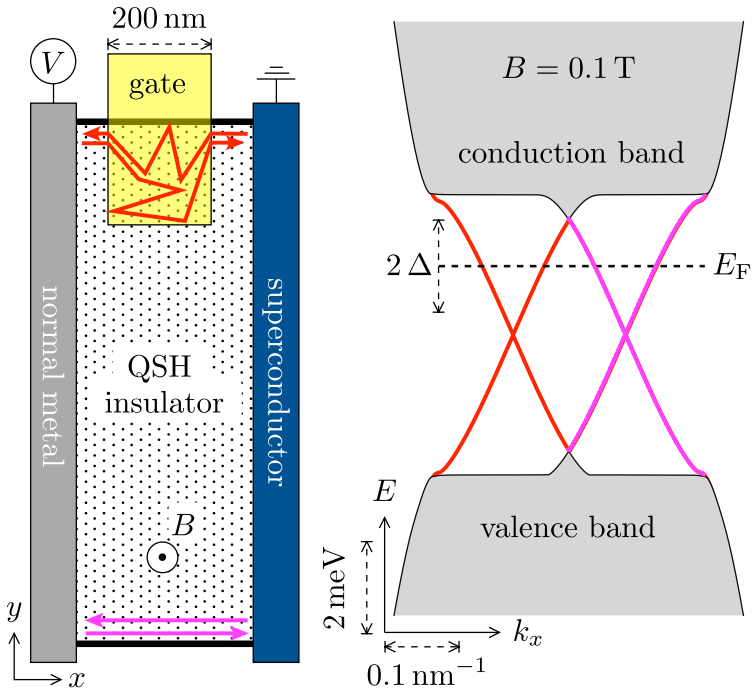

Figure 3.1. *Left panel:* Andreev quantum dot, created by a gate electrode at the edge of a quantum spin Hall (QSH) insulator in a perpendicular magnetic field B. A current I is passed between metallic and superconducting contacts, and the differential conductance $G = dI/dV$ is measured as a function of the bias voltage V for different gate voltages. *Right panel:* Band structure of an InAs/GaSb quantum well, for the parameters used in the computer simulations. The helical edge states appear inside the gap, connecting conduction and valence bands. Under the gate, the conduction band is pushed through the Fermi level at E_F, to create a metallic puddle. Inside the superconducting contact, a gap 2Δ opens around the Fermi level.

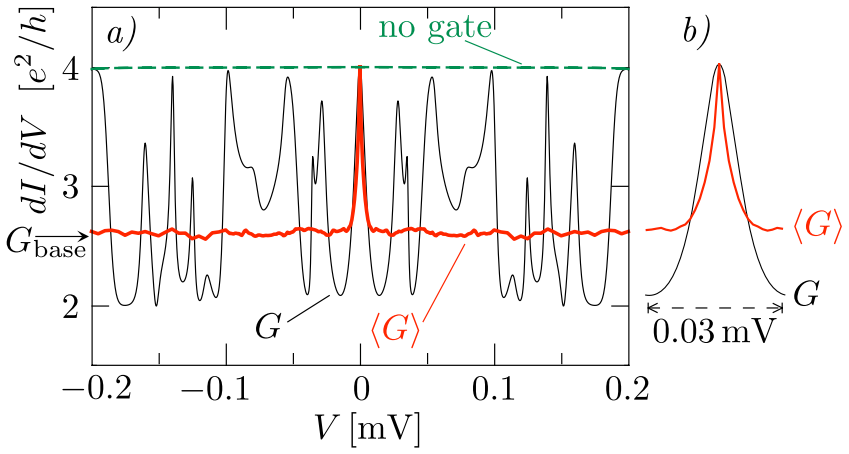

Figure 3.2. *a)* Zero-temperature differential conductance $G = dI/dV$ as a function of bias voltage V, calculated numerically for the system of Fig. 3.1. The bottom of the conduction band in the gated region (200 nm × 200 nm) is $E_c = -1.5$ meV below the Fermi level. The black curve is for a single disorder realization, the red curve is the disorder average. The calculated background conductance G_{base} from Eq. (3.6) is indicated (arrow). For comparison, the conductance without the gate electrode is also shown (green dashed curve). The Majorana resonance is then fully absorbed in the background and invisible. *b)* Enlargement of the Majorana resonance from the left panel, to show the difference in line shape.

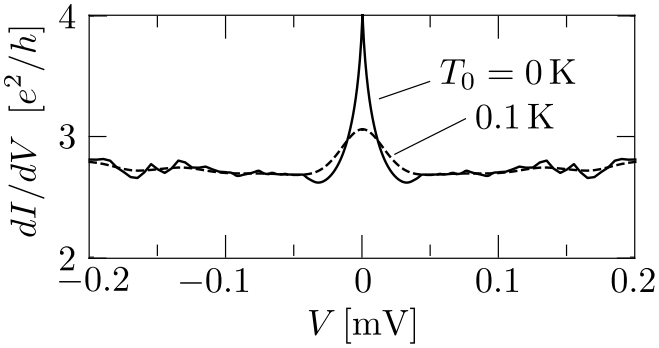

Figure 3.3. Differential conductance, averaged over gate voltages (-4.5 meV $\leq E_c \leq -1.5$ meV) for a single disorder realization. All system parameters are the same as in Fig. 3.2, except for the size of the gated region, which is 100 nm × 100 nm. The solid curve is at zero temperature and the dashed curve at a temperature of 0.1 K.

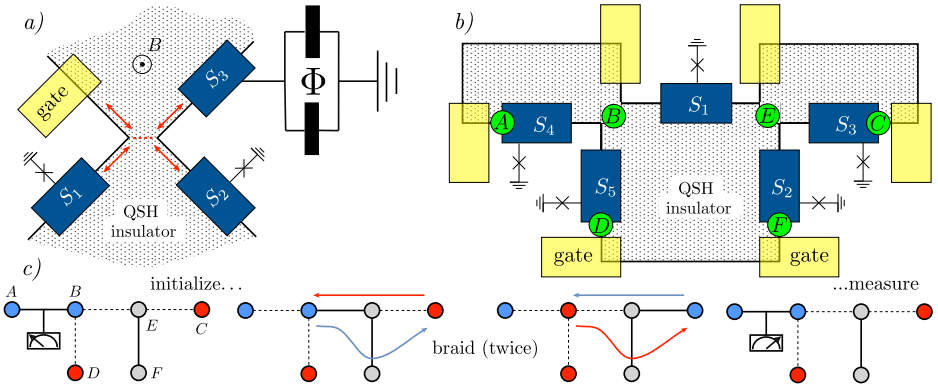

Figure 3.4. *a)* Constriction in a quantum spin-Hall insulator, contacted along three edges by a superconducting island. If the fourth edge is blocked by a gate electrode, the constriction traps a Majorana fermion. Each superconducting island is connected to a superconducting ground by a split Josephson junction enclosing a magnetic flux, indicated schematically by a $\times$ symbol and shown expanded for one of the islands. *b)* Two constrictions in series form a π-shaped circuit that can be used to braid the Majorana fermions (green circles). The flux through each split Josephson junction controls the coupling of adjacent Majoranas. *c)* Schematic of the braiding operation in the π-circuit [38]. Coupled Majoranas are connected by a solid line, uncoupled Majoranas by a dashed line.

Bibliography

[1] L. Fu and C. L. Kane, Phys. Rev. Lett. **100**, 096407 (2008).

[2] A. Yu. Kitaev, Phys. Usp. **44** (suppl.), 131 (2001).

[3] N. Read and D. Green, Phys. Rev. B **61**, 10267 (2000).

[4] Two reviews of the search for Majorana fermions in superconductors are: J. Alicea, Rep. Prog. Phys. **75**, 076501 (2012) [arXiv:1202.1293]; C. W. J. Beenakker, Annu. Rev. Con. Mat. Phys. **4**, 113 (2013) [arXiv:1112.1950].

[5] L. Fu and C. L. Kane, Phys. Rev. B **79**, 161408(R) (2009).

[6] J. Nilsson, A. R. Akhmerov, and C. W. J. Beenakker, Phys. Rev. Lett. **101**, 120403 (2008).

[7] Two reviews of topological insulators are: M. Z. Hasan and C. L. Kane, Rev. Mod. Phys. **82**, 3045 (2010); X.-L. Qi and S.-C. Zhang, Rev. Mod. Phys. **83**, 1057 (2011).

[8] M. Franz, arXiv:1302.3641.

[9] T. D. Stanescu and S. Tewari, arXiv:1302.5433.

[10] I. Knez, R.-R. Du, and G. Sullivan, Phys. Rev. Lett. **109**, 186603 (2012).

[11] C. Liu, T. L. Hughes, X.-L. Qi, K. Wang, and S.-C. Zhang, Phys. Rev. Lett. **100**, 236601 (2008).

[12] B. A. Bernevig, T. L. Hughes, and S. C. Zhang, Science **314**, 1757 (2006).

[13] M. König, S. Wiedmann, C. Brune, A. Roth, H. Buhmann, L. W. Molenkamp, X.-L. Qi, and S.-C. Zhang, Science **318**, 766 (2007).

[14] J. Maciejko, X.-L. Qi, and S.-C. Zhang, Phys. Rev. B **82**, 155310 (2010).

[15] Y. Tanaka, A. Furusaki, and K. A. Matveev, Phys. Rev. Lett. **106**, 236402 (2011).

[16] K. Hattori, J. Phys. Soc. Jpn. **80**, 124712 (2011).

[17] R. Ilan, J. Cayssol, J. H. Bardarson, and J. E. Moore, Phys. Rev. Lett. **109**, 216602 (2012).

[18] P. Delplace, J. Li, and M. Büttiker, Phys. Rev. Lett. **109**, 246803 (2012).

[19] C. Timm, Phys. Rev. B **86**, 155456 (2012).

[20] A. Del Maestro, T. Hyart, and B. Rosenow, arXiv:1207.7259.

[21] A. Roth, C. Brüne, H. Buhmann, L. W. Molenkamp, J. Maciejko, X.-L. Qi, and S.-C. Zhang, Science **325**, 294 (2009).

[22] M. König, M. Baenninger, A. G. F. Garcia, N. Harjee, B. L. Pruitt, C. Ames, P. Leubner, C. Brüne, H. Buhmann, L. W. Molenkamp, and D. Goldhaber-Gordon, arXiv:1211.3917.

[23] J. I. Väyrynen, M. Goldstein, and L. I. Glazman, arXiv:1303.1766.

[24] J. H. Bardarson, J. Phys. A **41**, 405203 (2008).

[25] C. W. J. Beenakker, Rev. Mod. Phys. **69**, 731 (1997).

[26] H. U. Baranger and P. A. Mello, Phys. Rev. Lett. **73**, 142 (1994).

[27] R. A. Jalabert, J.-L. Pichard, and C. W. J. Beenakker, Europhys. Lett. **27**, 255 (1994).

[28] K. T. Law, P. A. Lee, and T. K. Ng, Phys. Rev. Lett. **103**, 237001 (2009).

[29] C. Liu and S. Zhang, in Contemporary Concepts of Condensed Matter Science: *Topological Insulators*, Vol. 6, edited by Marcel Franz and Laurens Molenkamp (Elsevier, 2013) pp. 59 to pp. 89.

[30] I. M. Khaymovich, N. M. Chtchelkatchev, and V. M. Vinokur, Phys. Rev. B **84**, 075142 (2011).

[31] See the Appendix for details of the model calculation.

[32] I. H. Chan, R. M. Clarke, C. M. Marcus, K. Campman, and A. C. Gossard, Phys. Rev. Lett. **74**, 3876 (1995).

[33] M. W. Keller, A. Mittal, J. W. Sleight, R. G. Wheeler, D. E. Prober, R. N. Sacks, and H. Shtrikmann, Phys. Rev. B **53**, 1693 (1996).

[34] J. Alicea, Y. Oreg, G. Refael, F. von Oppen, and M. P. A. Fisher, Nature Phys. **7**, 412 (2011).

[35] J. D. Sau, D. J. Clarke, and S. Tewari, Phys. Rev. B **84**, 094505 (2011).

[36] B. van Heck, A. R. Akhmerov, F. Hassler, M. Burrello, and C. W. J. Beenakker, New J. Phys. **14**, 035019 (2012).

[37] B. I. Halperin, Y. Oreg, A. Stern, G. Refael, J. Alicea, and F. von Oppen, Phys. Rev. B **85**, 144501 (2012).

[38] T. Hyart, B. van Heck, I. C. Fulga, M. Burrello, A. R. Akhmerov, and C. W. J. Beenakker, arXiv:1303.4379.

[39] C. W. J. Beenakker, D. I. Pikulin, T. Hyart, H. Schomerus, and J. P. Dahlhaus, Phys. Rev. Lett. **110**, 017003 (2013).

Chapter 4

Disorder and magnetic field induced breakdown of helical edge conduction in an inverted electron-hole bilayer

4.1 Introduction

A two-dimensional band insulator can support two types of conducting edge states: counterpropagating (helical) edge states in zero magnetic field and unidirectional (chiral) edge states in a sufficiently strong perpendicular field. These two topologically distinct phases are referred to as a quantum spin Hall (QSH) and quantum Hall (QH) insulator, respectively [1, 2]. The physics of the QSH-to-QH transition is governed by band inversion [3–5]: The electron-like and hole-like subbands near the Fermi level are interchanged in a QSH insulator, so that the band gap in the bulk becomes smaller rather than larger with increasing perpendicular magnetic field [6, 7]. The gap closing at a characteristic field B_c signals the transition from an inverted QSH gap with helical edge states to a non-inverted QH gap supporting chiral edge states.

The early experiments on the QSH effect were performed in HgTe layers with CdTe barriers (type I quantum wells) [8, 9]. Recently the effect has also been observed in InAs/GaSb bilayers with AlSb barriers (type II quantum wells) [10–13]. Both types of quantum wells can have electron-

hole subbands in inverted order, but while these are strongly coupled in type I quantum wells, they are spatially separated and weakly coupled in the broken-gap quantum wells of type II (see Fig. 4.1). Although the difference has no consequences in zero magnetic field, we will show here that the breakdown of helical edge conduction in a magnetic field becomes qualitatively different.

In both type I and type II quantum wells we find an increase with disorder of the characteristic field B_c for the QSH-to-QH transition, as a consequence of the same mechanism that is operative in topological Anderson insulators [14]: a disorder-induced renormalization of the band gap [15]. Basically, in a narrow-gap semiconductor the effect of disorder on the bulk band gap is opposite in the inverted and non-inverted case. While a non-inverted band gap is reduced by disorder, the inverted band gap is increased. Since B_c is proportional to the zero-field band gap, it is pushed to larger fields by impurity scattering.

As a consequence, disorder increases the robustness of helical edge conduction in type I quantum wells, such as HgTe. In contrast, we find that in broken-gap quantum wells of type II a second transition at a weaker field B_c' appears, at which helical edge conduction gives way to bulk conduction. This lower characteristic field splits off from B_c with increasing disorder, producing a quasi-metallic regime in a broad field interval $B_c' \lesssim B \lesssim B_c$. The robustness of helical edge conduction is therefore reduced by disorder in type II quantum wells, such as InAs/GaSb. We discuss the magnetic-field induced bulk conduction in terms of Landau-level hybridization [16] and explain why it is only operative for weakly coupled electron-hole subbands.

4.2 Model Hamiltonian

Our investigation is based on the Bernevig-Hughes-Zhang Hamiltonian for inverted electron-hole bilayers [8, 10, 17]. In zero magnetic field the

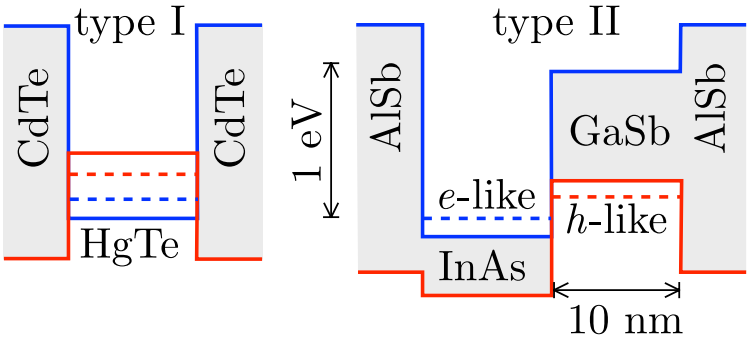

Figure 4.1. Alignment of conduction band (blue) and valence band (red) in a quantum well of type I (panel *a*) and type II (panel *b*). Both quantum wells have electron and hole subbands in inverted order (dotted lines, red *h*-like above blue *e*-like). The band gap (grey) is broken in the InAs/GaSb quantum well of type II, providing for a spatially separated electron-hole bilayer. There is no such spatial separation in the HgTe quantum well of type I.

Hamiltonian of the clean system takes the form

$$\mathcal{H}(\boldsymbol{k}) = \begin{pmatrix} H_0(\boldsymbol{k}) & H_1(\boldsymbol{k}) \\ -H_1^*(-\boldsymbol{k}) & H_0^*(-\boldsymbol{k}) \end{pmatrix}, \tag{4.1}$$

$$H_0(\boldsymbol{k}) = \begin{pmatrix} M_0 + \mu_+ k^2 & \beta k_+ \\ \beta k_- & -M_0 - \mu_- k^2 \end{pmatrix}, \tag{4.2}$$

$$H_1(\boldsymbol{k}) = \begin{pmatrix} \Delta_+ k_+ - i\alpha k_- & -\Delta_0 \\ \Delta_0 & \Delta_- k_- \end{pmatrix}, \tag{4.3}$$

as a function of wave vector $\boldsymbol{k} = (k_x, k_y)$ in the x-y plane of the quantum well. We have defined $k^2 = k_x^2 + k_y^2$, $k_\pm = k_x \pm i k_y$, $\mu_\pm = \mu_0 \pm \delta\mu$. It is a tight-binding Hamiltonian in the spin ($\uparrow\downarrow$) and subband ($\pm$) degrees of freedom, acting on a wave function with elements $(\psi_{+\uparrow}, \psi_{-\uparrow}, \psi_{+\downarrow}, \psi_{-\downarrow})$. The term $\beta k_\pm$ in block H_0 describes the inter-subband coupling, and the block H_1 accounts for Rashba and Dresselhaus spin-orbit coupling. To model the two types of quantum wells we use the parameters listed in Table 4.1. [18]

The time-reversal symmetry breaking effect of a perpendicular magnetic field $\boldsymbol{B} = (0, 0, B)$ is predominantly orbital, accounted for by the substitution $\boldsymbol{k} \mapsto \boldsymbol{k} - (e/\hbar)\boldsymbol{A}$, with vector potential $\boldsymbol{A} = (0, Bx, 0)$. The Zeeman effect, which would be the dominant effect in a parallel field, is not included. (We will return to this later on.)

	type I	type II
M_0 [eV]	-0.01	-0.01
μ_0 [eV·Å^2]	68.6	81.9
$\delta\mu$ [eV·Å^2]	51.1	21.6
β [eV·Å]	3.65	0.72
Δ_0 [eV]	0.0016	0.0003
Δ_+ [eV·Å]	-0.128	0.0011
Δ_- [eV·Å]	0.211	0.0006
α [eV·Å]	0.0	0.16

Table 4.1. Parameters of the tight-binding Hamiltonian (4.1) used in the numerical simulations of quantum wells of type I (HgTe) and type II (InAs/GaSb).[18] The electron-hole asymmetry parameter $\delta\mu$ is set to zero in some of the calculations.

In Figs. 4.2 and 4.3 we show the magnetic field dependence of the Landau levels in the two types of quantum wells. If the inverted electron and hole subbands would be totally uncoupled, then all Landau levels from the valence band would move upwards while all Landau levels from the conduction band would move downwards — resulting in an accumulation of Landau levels inside the zero-field band gap $|E| < |M_0|$. Electron-hole coupling hybridizes the Landau levels from conduction and valence band [16], pushing them out of the gap. In a type I quantum well only a single pair of Landau levels remains inside the gap, see Fig. 4.2*a*. The spatial separation of the electron-hole subbands in a type II quantum well does allow for multiple Landau levels inside the gap, the more so the larger $|M_0|$ — compare Figs. 4.2*b* and 4.3.

To define the characteristic fields mentioned in the introduction it is convenient to set the electron-hole asymmetry parameter $\delta\mu$ to zero, so that the Landau level crossings are all in the middle of the gap, at $E = 0$. As indicated in Fig. 4.3, the first and the last level crossing then identify, respectively, B_c' and B_c. As we will now show, these two fields delimit a regime of bulk conduction in a disordered type II quantum well.

To study the effect of disorder we discretize the tight-binding Hamiltonian (4.1) on a square lattice (lattice constant $a = 2.5\,\mathrm{nm}$, size $W \times L = 500\,\mathrm{nm} \times 300\,\mathrm{nm}$). Randomly distributed dopants are introduced by adding a spin- and layer-independent random potential $U(\boldsymbol{r})$, fluctuating from site to site in the interval $(-U_0/2, U_0/2)$. We take either periodic

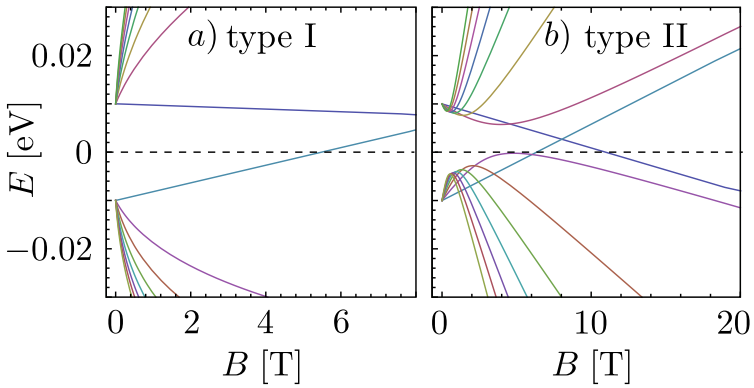

Figure 4.2. Landau level spectrum in the two types of quantum wells, calculated from the Hamiltonian (4.1) for the parameters of Table 4.1 (nonzero $\delta\mu$ and $M_0 = -0.01\,\mathrm{eV}$).

or hard-wall boundary conditions along the sides at $y = 0, W$ and attach the ends at $x = 0, L$ to ballistic leads to obtain the transmission matrix t at the Fermi level E_F. The conductance $G = (e^2/h)\,\mathrm{Tr}\,tt^\dagger$ is averaged over 60 disorder realizations. All calculations were performed using the KWANT tight-binding code [19]. Results are presented in Figs. 4.4 and 4.5.

4.3 Results

We first discuss Fig. 4.4, which shows data for the type II quantum well with electron-hole symmetry. The QSH regime of helical edge conduction appears as a region of quantized conductance $G = 2e^2/h$ in the low-field/weak-disorder corner of panel *a* (hard-wall boundary conditions). The high-field/weak-disorder corner is the QH regime, with $G = 0$ because the Fermi level lies in the gap between the chiral edge states of conduction and valence band. The region between the QSH and QH regimes has a nonquantized conductance $G \gtrsim 2e^2/h$. This is a regime of bulk conduction, since a removal of the edge states by switching from hard-wall to periodic boundary conditions makes no difference (compare panels *a* and *b*). We call this regime "quasi-metallic" rather than metallic, because in the limit of an infinite system all bulk states should localize in a magnetic field.

The curves marked B_c and B_c' in Fig. 4.4 are obtained as in Fig. 4.3, with the effects of disorder accounted for as follows: We replace

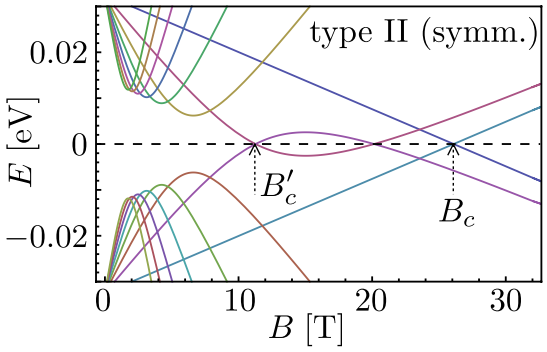

Figure 4.3. Same as Fig. 4.2, for a type II quantum well with electron-hole symmetry ($\delta\mu = 0$) and for a larger zero-field gap $M_0 = -0.0325\,\mathrm{eV}$. The two characteristic fields B_c' and B_c of the first and last Landau level crossing are indicated.

the zero-field band gap M_0 by the renormalized gap $M_{\mathrm{eff}}(U_0)$ in Born approximation,

$$M_{\mathrm{eff}} = M_0 - c\,U_0^2, \tag{4.4}$$

with $c = 0.39\,[\mathrm{eV}]^{-1}$. The band gap M_0 of the clean system is negative, so disorder increases the band gap, as in the topological Anderson insulator [15]. There is no renormalization of the Fermi energy for $\delta\mu = 0$. The Landau level broadening is estimated at $\delta E = U_0^2 \times 0.05\,[\mathrm{eV}]^{-1}$, so that the characteristic fields are determined by the first and last Landau level crossing with the line $E = \delta E$ (rather than with $E = 0$). As is evident from Fig. 4.4, the resulting curves $B_c(U_0)$ and $B_c'(U_0)$ describe quite well the boundaries of the quasi-metallic regime, over a broad range of magnetic fields and disorder strengths.

These are results for the electron-hole symmetric case $\delta\mu = 0$, but the appearance of the magnetic-field induced quasi-metallic regime is a generic feature of inverted type II quantum wells, not tied to electron-hole symmetry — the weak electron-hole coupling is the essential ingredient. This is demonstrated in Fig. 4.5. Because of the non-zero $\delta\mu$ the Fermi energy is renormalized by disorder, which we take into account in Born approximation,

$$E_{\mathrm{F}} = -d\,U_0^2. \tag{4.5}$$

The coefficient d equals $0.12\,[\mathrm{eV}]^{-1}$ and $0.27\,[\mathrm{eV}]^{-1}$, respectively, in the type I and type II quantum wells.

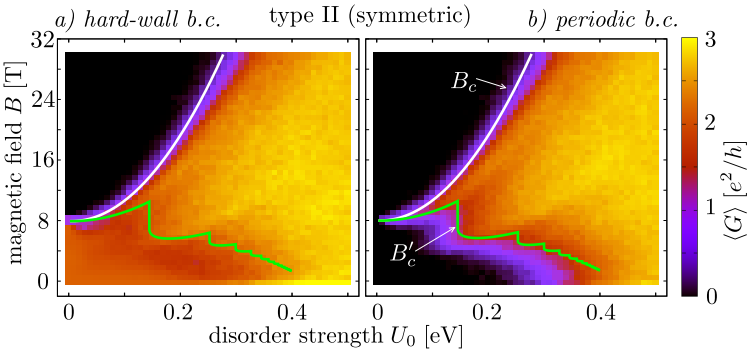

Figure 4.4. Disorder-averaged conductance of a type II quantum well with electron-hole symmetry ($\delta\mu = 0$, other parameters as in Table 4.1), calculated numerically from the tight-binding Hamiltonian (4.1), with hard-wall boundary conditions (panel *a*) or periodic boundary conditions (panel *b*). The Fermi level is set at $E_F = 8 \cdot 10^{-4}$ eV, slightly displaced from the center of the bulk gap to avoid the minigap in the spectrum of helical edge states. The disorder dependence of the characteristic fields B_c and B_c' (white and green curves) is calculated from the renormalization of the band gap in Born approximation, as described in the text.

Comparing the results for the type II quantum well (with hard-wall boundary conditions), we see that Figs. 4.4*a* and 4.5*b* are qualitatively similar, the main effect of the broken electron-hole symmetry being the appearance at weak disorder of a regime of quantized chiral edge conductance ($G = e^2/h$). As one can see in Fig. 4.2*b*, the Landau levels depend nonmonotonically on the magnetic field, and this shows up in Fig. 4.5*b* as a nonmonotonic variation of the conductance from $2 \to 1 \to 2 \to 1 \to 0 \times e^2/h$ at weak disorder.

Both figures 4.4*a* and 4.5*b* show the regime of bulk conduction at strong disorder characteristic of an inverted type II quantum well. This regime requires small electron-hole coupling, to allow for an accumulation of Landau levels near the Fermi energy (compare Figs. 4.2*a* and 4.2*b*). For that reason the quasi-metallic regime is absent in the type I quantum well of Fig. 4.5*a*, which instead shows the expected [20, 21] transition to localized edge states at strong disorder.

So far we have focused on the orbital effect of a perpendicular magnetic field. The effect of spin splitting by the Zeeman energy $g\mu_B B$ is shown in Fig. 4.6, for the type-II quantum well with periodic boundary conditions and electron-hole symmetry. We took the value $g = -7.5$ of

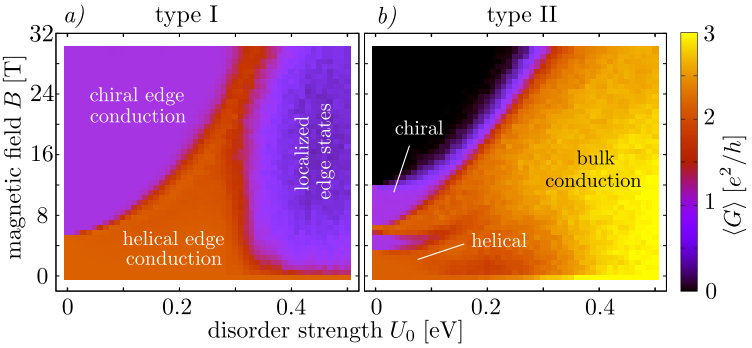

Figure 4.5. Disorder-averaged conductance of a quantum well of type I (panel *a*) and type II (panel *b*), with hard-wall boundary conditions. The parameters are those of Table 4.1, including the effects of broken electron-hole symmetry (nonzero $\delta\mu$). The conductance is calculated at the renormalized Fermi energy (4.5). The region of bulk conduction is present in the type II quantum well, but not in type I, where instead a region of localized edge states appears. (This region turns black for periodic boundary conditions, so we know there is no bulk conduction there.)

bulk InAs, comparable absolute values may be expected for a narrow InAs/GaSb quantum well [22]. Comparison with Fig. 4.4*b* (where we had $g = 0$) shows a qualitatively similar phase diagram, in particular the regime of bulk conduction persists. Possible due to electron-electron interactions or geometry larger g-factors may have more dramatic effect [23].

4.4 Conclusion

In summary, we have investigated how disorder affects the breakdown of the QSH effect in a perpendicular magnetic field. In inverted type I quantum wells, such as HgTe, the characteristic breakdown field B_c increases with disorder strength, due to a renormalization of the band gap (becoming more and more negative with increasing disorder). The same effect is operative in broken gap quantum wells of type II, such as InAs/GaSb — however, there it does not lead to an increased robustness of helical edge conduction. The spatial separation of the inverted electron-hole subbands leads to the accumulation of Landau levels in the zero-field band gap, producing a regime of bulk conduction that extends to lower

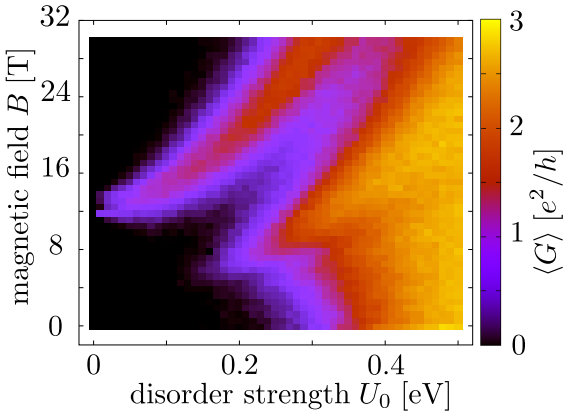

Figure 4.6. Same as Fig. 4.4*b*, but including the effects of the Zeeman energy with effective g-factor -7.5.

and lower magnetic fields with stronger disorder, see Fig. 4.4.

One implication of our findings, see Fig. 4.5, is that the weak disorder limit is in principle consistent with the persistence of helical edge conduction up to 8 T perpendicular fields, reported in Ref. 13. However, in the presence of strong disorder the bulk conduction is expected to take over at much smaller fields.

As directions for further research, it would be interesting to explore the fate of the quasi-metallic regime in the thermodynamic limit. All two-dimensional bulk states should localize in a magnetic field, but the numerics suggests a large localization length. It would also be of interest to study the effect of Landau level accumulation on exciton condensation in the electron-hole bilayer, considered recently in connection with the QSH effect [24, 25].

Bibliography

[1] M. Z. Hasan and C. L. Kane, Rev. Mod. Phys. **82**, 3045 (2010).

[2] X.-L. Qi and S.-C. Zhang, Rev. Mod. Phys. **83**, 1057 (2011).

[3] G. Tkachov and E. M. Hankiewicz, Phys. Rev. Lett. **104**, 166803 (2010); Physica E **44**, 900 (2012).

[4] J.-C. Chen, J. Wang, and Q.-F. Sun, Phys. Rev. B **85**, 125401 (2012).

[5] B. Scharf, A. Matos-Abiague, and J. Fabian, Phys. Rev. B **86**, 075418 (2012).

[6] J. R. Meyer, R. J. Wagner, F. J. Bartoli, C. A. Hoffman, M. Dobrowolska, T. Wojtowicz, J. K. Furdyna, and L. R. Ram-Mohan, Phys. Rev. B **42**, 9050 (1990).

[7] M. Schultz, U. Merkt, A. Sonntag, U. Rössler, R. Winkler, T. Colin, P. Helgesen, T. Skauli, and S. Løvold, Phys. Rev. B **57**, 14772 (1998).

[8] B. A. Bernevig, T. L. Hughes, and S.-C. Zhang, Science **314**, 1757 (2006).

[9] M. König, S. Wiedmann, C. Brüne, A. Roth, H. Buhmann, L. W. Molenkamp, X.-L. Qi, and S.-C. Zhang, Science **318**, 766 (2007).

[10] C. Liu, T. L. Hughes, X.-L. Qi, K. Wang, and S.-C. Zhang, Phys. Rev. Lett. **100**, 236601 (2008).

[11] I. Knez, R.-R. Du, and G. Sullivan, Phys. Rev. Lett. **107**, 136603 (2011).

[12] K. Suzuki, Y. Harada, K. Onomitsu, and K. Muraki, Phys. Rev. B **87**, 235311 (2013).

[13] L. Du, I. Knez, G. Sullivan, and R.-R. Du, arXiv:1306.1925.

[14] J. Li, R.-L. Chu, J. K. Jain, and S.-Q. Shen, Phys. Rev. Lett. **102**, 136806 (2009).

[15] C. W. Groth, M. Wimmer, A. R. Akhmerov, J. Tworzydło, and C. W. J. Beenakker, Phys. Rev. Lett. **103**, 196805 (2009).

[16] K. Suzuki, K. Takashina, S. Miyashita, and Y. Hirayama, Phys. Rev. Lett. **93**, 016803 (2004).

[17] C. Liu and S.-C. Zhang, in *Topological Insulators*, edited by M. Franz and L. W. Molenkamp (Elsevier, Amsterdam, 2013).

[18] Following Ref. [17], the type I parameters in Table 4.1 are those of a 7 nm thick HgTe quantum well. The type II parameters correspond to a 8.4 nm/10 nm InAs/GaSb quantum well, except for M_0, for which we took the same value as for the type I quantum well in order to simplify the comparison.

[19] C. W. Groth, M. Wimmer, A. R. Akhmerov, and X. Waintal, arXiv:1309.2926.

[20] J. Maciejko, X.-L. Qi, and S.-C. Zhang, Phys. Rev. B **82**, 155310 (2010).

[21] P. Delplace, J. Li, and M. Büttiker, Phys. Rev. Lett. **109**, 246803 (2012).

[22] T. P. Smith and F. F. Fang, Phys. Rev. B **35**, 7729 (1987).

[23] D. I. Pikulin and J. Alicea, unpublished.

[24] D. I. Pikulin and T. Hyart, arXiv:1311.1111.

[25] J. C. Budich, B. Trauzettel, and P. Michetti, arXiv:1311.2043.

Chapter 5

Fake Majorana resonances: X-shaped and Y-shaped Andreev resonance profiles in a superconducting quantum dot

5.1 Introduction

Half a century has passed since Alexander Andreev reported the curious retro-reflection of electrons at the interface between a normal metal and a superconductor [1]. One reason why Andreev reflection is still very much a topic of active research, is the recent interest in Majorana zero-modes [2]: Nondegenerate bound states at the Fermi level ($E = 0$) consisting of a coherent superposition of electrons and holes, coupled via Andreev reflection. These are observed in the differential conductance as a resonant peak around zero bias voltage V that does not split upon variation of a magnetic field B [3–6]. In the B, V plane the conductance peaks trace out an unusual Y-shaped profile, distinct from the more common X-shaped profile of peaks that meet and immediately split again. (See Fig. 5.1.)

It is tempting to think that the absence of a splitting of the zero-bias conductance peak demonstrates that the quasi-bound state is nonde-

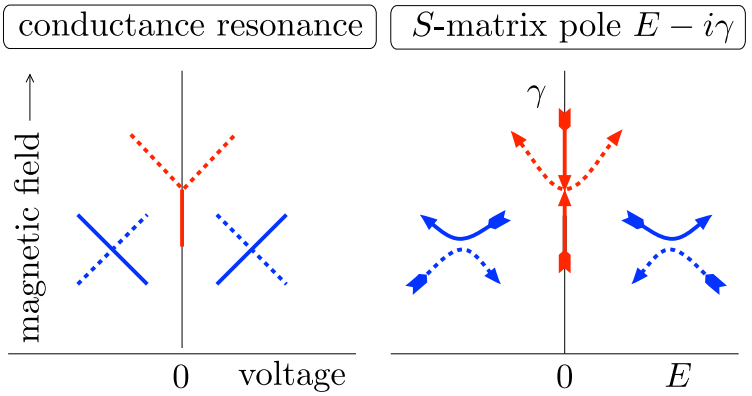

Figure 5.1. Left panel: Magnetic field B-dependence of peaks in the differential conductance $G = dI/dV$. The peak positions trace out an X-shaped or Y-shaped profile in the B-V plane. Right panel: Location of the poles of the scattering matrix $S(\varepsilon)$ in the complex energy plane $\varepsilon = E - i\gamma$. The arrows indicate how the poles moves with increasing magnetic field.

generate, hence Majorana. This is mistaken. As shown in a computer simulation [7], the Y-shaped conductance profile is generic for superconductors with broken spin-rotation and broken time-reversal symmetry, irrespective of the presence or absence of Majorana zero-modes. The theoretical analysis of Ref. [7] focused on the ensemble-averaged conductance peak, in the context of the weak antilocalization effect [8–11]. Here we analyze the sample-specific conductance profile, by relating the X-shape and Y-shape to different configurations of poles of the scattering matrix in the complex energy plane [12].

5.2 Andreev billiard

5.2.1 Scattering resonances

We study the Andreev billiard geometry of Fig. 5.2: A semiconductor quantum dot strongly coupled to a superconductor and weakly coupled to a normal metal. In the presence of time-reversal symmetry an excitation gap is induced in the quantum dot by the proximity effect [13]. We assume that the gap is closed by a sufficiently strong magnetic field. Quasi-bound states can then appear near the Fermi level ($E = 0$),

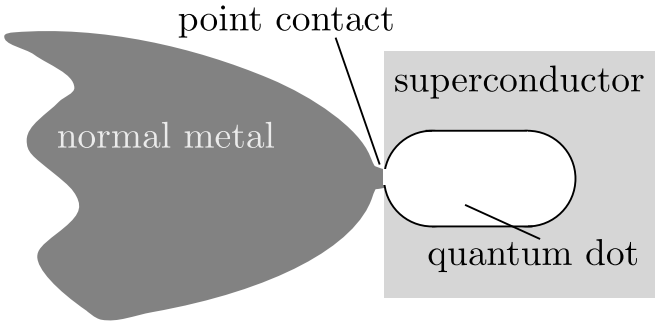

Figure 5.2. Schematic illustration of an Andreev billiard.

described by the Hamiltonian

$$\mathcal{H} = \sum_{\mu,\nu} |\mu\rangle H_{\mu\nu} \langle\nu| + \sum_{\mu,a} \big(|\mu\rangle W_{\mu a} \langle a| + |a\rangle W^*_{\mu a} \langle\mu| \big). \tag{5.1}$$

The bound states in the closed quantum dot are eigenvalues of the $M \times M$ Hermitian matrix $H = H^\dagger$. The $M \times N$ matrix W couples the basis states $|\mu\rangle$ in the quantum dot to the normal metal, via N propagating modes $|a\rangle$ through a point contact. In principle we should take the limit $M \to \infty$, but in practice $M \gg N$ suffices.

The amplitudes of incoming and outgoing modes in the point contact at energy E (relative to the Fermi level) are related by the $N \times N$ scattering matrix [14, 15]

$$S(E) = 1 + 2\pi i W^\dagger \left(H - i\pi W W^\dagger - E \right)^{-1} W. \tag{5.2}$$

This is a unitary matrix, $S(E)S^\dagger(E) = 1$.

A scattering resonance corresponds to a pole $\varepsilon = E - i\gamma$ of the scattering matrix in the complex energy plane, which is an eigenvalue of the non-Hermitian matrix

$$H_{\text{eff}} = H - i\pi W W^\dagger. \tag{5.3}$$

The positive definiteness of $WW^\dagger$ ensures that the poles all lie in the lower half of the complex plane, $\gamma \geq 0$, as required by causality. Particle-hole symmetry implies that ε and $-\varepsilon^*$ are both eigenvalues of H_{eff}, so the poles are symmetrically arranged around the imaginary axis.

The differential conductance $G(V) = dI/dV$ of the quantum dot, measured by grounding the superconductor and applying a bias voltage to the normal metal, is obtained from the scattering matrix via [7]

$$G(V) = \frac{e^2}{h}\left[\frac{N}{2} - \frac{1}{2}\operatorname{Tr} S(eV)\tau_z S^\dagger(eV)\tau_z\right], \tag{5.4}$$

in the electron-hole basis, and

$$G(V) = \frac{e^2}{h}\left[\frac{N}{2} - \frac{1}{2}\operatorname{Tr} S(eV)\tau_y S^\dagger(eV)\tau_y\right], \tag{5.5}$$

in the Majorana basis. The Pauli matrices τ_y, τ_z act on the electron-hole degree of freedom. The two bases are related by the unitary transformation

$$S \mapsto USU^\dagger, \;\; U = \frac{1}{\sqrt{2}}\begin{pmatrix} 1 & 1 \\ i & -i \end{pmatrix}. \tag{5.6}$$

5.2.2 Gaussian ensembles

For a random-matrix description we assume that the scattering in the quantum dot is chaotic, and that this applies to normal scattering from the electrostatic potential as well as to Andreev scattering from the pair potential. In the large-M limit we may then take a Gaussian distribution for H,

$$P(H) \propto \exp\left(-\frac{c}{M}\operatorname{Tr} H^2\right). \tag{5.7}$$

By taking the matrix elements of H to be real, complex, or quaternion numbers (in an appropriate basis), one obtains the Wigner-Dyson ensembles of non-superconducting chaotic billiards [16–18]. Particle-hole symmetry then plays no role, because normal scattering does not couple electrons and holes.

Altland and Zirnbauer introduced the particle-hole symmetric ensembles appropriate for an Andreev billiard [19]. The two ensembles without time-reversal symmetry are obtained by taking the matrix elements of $i \times H$ (instead of H itself) to be real or quaternion. When iH is real there is only particle-hole symmetry (class D), while when iH is quaternion there is particle-hole and spin-rotation symmetry (class C).

Both the Wigner-Dyson (WD) and the Altland-Zirnbauer (AZ) ensembles are characterized by a parameter $\beta \in \{1, 2, 4\}$ that describes the

strength of the level repulsion factor in the probability distribution of distinct eigenvalues E_i of H: a factor $\prod_{i<j}|E_i - E_j|^\beta$ in the WD ensembles and a factor $\prod'_{i<j}|E_i^2 - E_j^2|^\beta$ in the AZ ensembles. (The prime indicates that the product includes only the positive eigenvalues.)

In the WD ensembles the parameter β also counts the number of degrees of freedom of the matrix elements of H: $\beta = 1$, 2 or 4 when H is real, complex, or quaternion, respectively. In the AZ ensembles this connection is lost: $\beta = 2$ in the class C ensemble (iH real) as well as in the class D ensemble (iH quaternion).

The coefficient c can be related to the average spacing δ_0 of distinct eigenvalues of H in the bulk of the spectrum,

$$c = \frac{\beta\pi^2}{8\delta_0^2} \times \begin{cases} 2 & \text{in the WD ensembles,} \\ 1 & \text{in the AZ ensembles.} \end{cases} \tag{5.8}$$

The coefficient (5.8) for the AZ ensembles is twice as small as it is in the WD ensembles with the same β, on account of the $\pm E$ symmetry of the spectrum, see App. 5.6.1.

Because the distribution of H is basis independent, we may without loss of generality choose a basis such that the coupling matrix W is diagonal,

$$W_{mn} = w_n\delta_{mn}, \quad 1 \le m \le M, \quad 1 \le n \le N. \tag{5.9}$$

The coupling strength w_n is related to the tunnel probability $\Gamma_n \in (0,1)$ of mode n into the quantum dot by [14, 15]

$$|w_n|^2 = \frac{M\delta_0}{\pi^2\Gamma_n}\bigl(2 - \Gamma_n - 2\sqrt{1-\Gamma_n}\bigr). \tag{5.10}$$

5.2.3 Class C and D ensembles

We summarize the properties of the $\beta = 2$ Altland-Zirnbauer ensembles, symmetry class C and D, that we will need for our study of the Andreev resonances. (See App. 5.6.2 for the corresponding $\beta = 1, 4$ formulas in symmetry class CI and DIII.) Similar formulas can be found in Ref. [20].

When Andreev scattering operates together with spin-orbit coupling, one can combine electron and hole degrees of freedom from the same spin band into a real basis of Majorana fermions. [This change of basis amounts to the unitary transformation (5.6).] In the Majorana basis the

constraint of particle-hole symmetry reads simply

$$H = -H^*, \tag{5.11}$$

so we can take $H = iA$ with A a real antisymmetric matrix. In the Gaussian ensemble the upper-diagonal matrix elements A_{nm} ($n < m$) all have identical and independent distributions,

$$P(\{A_{nm}\}) \propto \prod_{1=n<m}^{M} \exp\left(-\frac{\pi^2 A_{nm}^2}{2M\delta_0^2}\right), \tag{5.12}$$

see Eqs. (5.7) and (5.8). This is the $\beta = 2$ class-D ensemble, without spin-rotation symmetry.

The $\beta = 2$ class-C ensemble applies in the absence of spin-orbit coupling, when spin-rotation symmetry is preserved. Andreev reflection from a spin-singlet superconductor couples only electrons and holes from different spin bands, which cannot be combined into a real basis state. It is then more convenient stay in the electron-hole basis and to eliminate the spin degree of freedom by considering a single spin band for the electron and the opposite spin band for the hole. (The matrix dimensionality M and the mean level spacing δ_0 then refer to a single spin.) In this basis the particle-hole symmetry requires

$$H = -\tau_y H^* \tau_y, \tag{5.13}$$

where the Pauli matrix τ_y operates on the electron and hole degrees of freedom.

The constraint (5.13) implies that $H = iQ$ with Q a quaternion anti-Hermitian matrix. Its matrix elements are of the form

$$\begin{aligned} &Q_{nm} = a_{nm}\tau_0 + ib_{nm}\tau_x + ic_{nm}\tau_y + id_{nm}\tau_z, \\ &n, m = 1, 2, \ldots M/2, \end{aligned} \tag{5.14}$$

with real coefficients a, b, c, d (to ensure that $Q_{nm} = \tau_y Q_{nm}^* \tau_y$). Anti-Hermiticity of Q requires that the off-diagonal elements are related by $a_{nm} = -a_{mn}$ and $x_{nm} = x_{mn}$ for $x \in \{b, c, d\}$. On the diagonal $a_{nn} = 0$. In the Gaussian ensemble the independent matrix elements have the distribution

$$\begin{aligned} P(\{Q_{nm}\}) \propto &\prod_{n=1}^{M/2} \exp\left(-\frac{\pi^2}{2M\delta_0^2}(b_{nn}^2 + c_{nn}^2 + d_{nn}^2)\right) \\ &\times \prod_{1=n<m}^{M/2} \exp\left(-\frac{\pi^2}{M\delta_0^2}(a_{nm}^2 + b_{nm}^2 + c_{nm}^2 + d_{nm}^2)\right), \end{aligned} \tag{5.15}$$

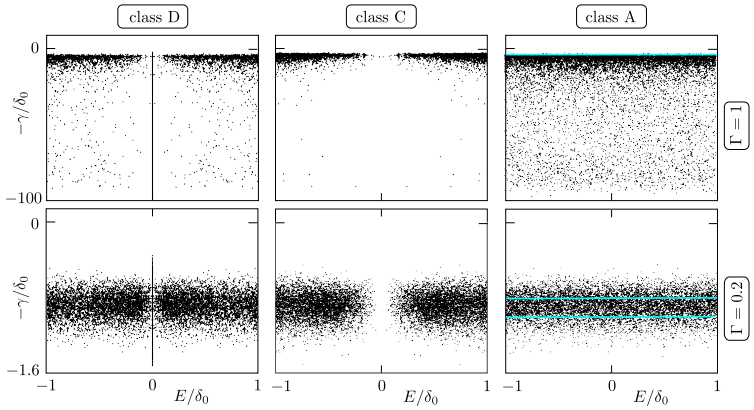

Figure 5.3. Scatter plot of the poles $\varepsilon = E - i\Gamma$ of 5000 scattering matrices $S(\varepsilon)$, in the Gaussian ensembles of class D, C, and A (first, second, and third column), for ballistic coupling ($\Gamma = 1$, first row) and for tunnel coupling ($\Gamma = 0.2$, second row). In each case the Hamiltonian has dimension $M \times M = 500 \times 500$ and the scattering matrix $N \times N = 50 \times 50$. Only a narrow energy range near $E = 0$ is shown, to contrast the accumulation of the poles on the imaginary axis in class D and the repulsion in class C. The blue horizontal lines indicate the expected boundaries (5.17) of the class-A scatter plot in the limit $N, M/N \to \infty$.

5.3 Andreev resonances

5.3.1 Accumulation on the imaginary axis

In Fig. 5.3 we show the location of the poles of the scattering matrix in the complex energy plane, for the $\beta = 2$ Altland-Zirnbauer ensembles with and without spin-rotation symmetry (class C and D, respectively). The $\beta = 2$ Wigner-Dyson ensemble (class A, complex H) is included for comparison. The poles are eigenvalues ε of the non-Hermitian effective Hamiltonian (5.1), with H distributed according to the Gaussian distribution (5.7)–(5.8), $\beta = 2$, and coupling matrix W given by Eqs. (5.9)–(5.10). For simplicity we took identical tunnel probabilities $\Gamma_n \equiv \Gamma$ for each of the N modes connecting the quantum dot to the normal metal.

The number M of basis states in the quantum dot is taken much larger than N, to reach the random-matrix regime. In class C this number is necessarily even, as demanded by the particle-hole symmetry relation (5.13). The symmetry relation (5.11) in class D imposes no such constraint, and when M is odd there is an unpaired Majorana zero-mode in the

spectrum [20, 21]. The class-D superconductor with a Majorana zero-mode is called topologically nontrivial, while class C or class D without a zero-mode is called topologically trivial [22–24]. For a more direct comparison of class C and class D we take M even in both cases, so both superconductors are topologically trivial.

In the absence of particle-hole symmetry (class A), the poles $\varepsilon = E - i\gamma$ of the scattering matrix have a density [25]

$$\rho(E,\gamma) = \frac{N}{4\pi\gamma^2}, \quad \gamma_{\min} < \gamma < \gamma_{\max}, \tag{5.16}$$

$$\gamma_{\min} = N\Gamma\delta_0/4\pi, \quad \gamma_{\max} = \gamma_{\min}/(1-\Gamma), \tag{5.17}$$

for $|E| \ll M\delta_0$ and asymptotically in the limit $N, M/N \to \infty$. For $|E| \gtrsim \delta_0$ all three $\beta = 2$ ensembles A, C, D have a similar density of poles, but for smaller $|E|$ the densities are strikingly different, see Fig. 5.3. While in class C the poles are repelled from the imaginary axis, in class D they accumulate on that axis.

As pointed out in Ref. [12], a nondegenerate pole $\varepsilon = -i\gamma$ on the imaginary axis has a certain stability, it cannot acquire a nonzero real part E without breaking the $\varepsilon \leftrightarrow -\varepsilon^*$ symmetry imposed by particle-hole conjugation. To see why this stability is not operative in class C, we note that on the imaginary axis γ is a real eigenvalue of the matrix

$$\Omega = -Q + \pi WW^\dagger \text{ in class C}, \tag{5.18}$$

$$\Omega = -A + \pi WW^\dagger \text{ in class D}. \tag{5.19}$$

In both classes the matrix Ω commutes with an anti-unitary operator, $\mathcal{C}\Omega = \Omega\mathcal{C}$, with $\mathcal{C} = i\tau_y\mathcal{K}$ in class C and $\mathcal{C} = \mathcal{K}$ in class D. (The operator $\mathcal{K}$ performs a complex conjugation.) In class C this operator $\mathcal{C}$ squares to -1, so a real eigenvalue γ of Ω has a Kramers degeneracy [26] and hence nondegenerate poles $\varepsilon = -i\gamma$ on the imaginary axis are forbidden. In class D, in contrast, the operator $\mathcal{C}$ squares to $+1$, Kramers degeneracy is inoperative and nondegenerate poles are allowed and in fact generic.

5.3.2 Square-root law

As we explain in App. 5.6.3, for ballistic coupling ($\Gamma = 1$) the statistics of poles on the imaginary axis can be mapped onto the statistics of the real eigenvalues of an $M \times M$ random orthogonal matrix with N rows

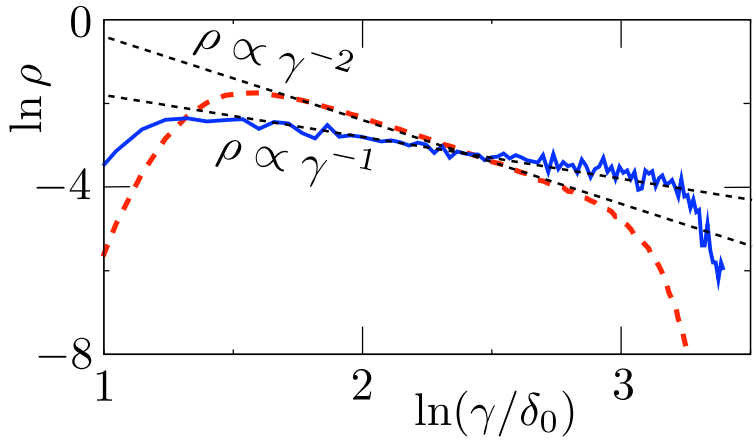

Figure 5.4. Double-logarithmic plot of the probability distribution $\rho(\gamma)$, normalized to unity, of the imaginary part γ of the poles of the scattering matrix. The curves are calculated by averaging over some 2000 realizations of the class-D ensemble, with $N = 10$, $M = 500$, $\Gamma = 0.9$. The red dashed curve includes all poles, while the blue solid curve includes only the poles on the imaginary axis ($E = 0$). The black dashed lines are the predicted slopes from Eq. (5.16) and (5.20).

and columns deleted — which is a solved problem [27, 28]. The linear density profile $\rho_0(\gamma)$ on the imaginary axis is

$$\rho_0(\gamma) = \sqrt{\frac{N\Gamma}{8\pi}}\,\frac{1}{\gamma}, \quad \gamma_{\rm min} < \gamma < \gamma_{\rm max}, \tag{5.20}$$

for $1 \ll N\Gamma \ll M$ and $\gamma_{\rm min}$, $\gamma_{\rm max}$ given by Eq. (5.17). We *conjecture* that this density profile, derived [27] for $\Gamma = 1$, holds also for $\Gamma < 1$. In Fig. 5.4 we give numerical evidence in support of this conjecture.

In Fig. 5.5 we show how the average number $\langle N_{\rm Y}\rangle$ of class-D poles on the imaginary axis depends on the dimensionality N of the scattering matrix and on the tunnel probability Γ. We compare with the square-root law [29]

$$\langle N_{\rm Y}\rangle = -\sqrt{\frac{N\Gamma}{8\pi}}\,\ln(1-\Gamma), \tag{5.21}$$

implied by integration of our conjectured density profile (5.20). This $\sqrt{N}$ scaling is generic for random-matrix ensembles that exhibit accumulation of eigenvalues on the real or imaginary axis, such as the Ginibre ensemble

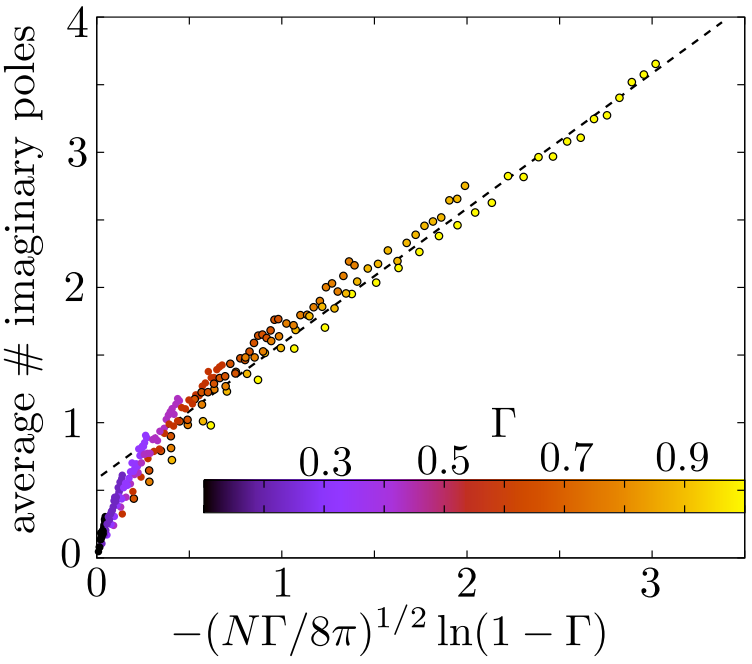

Figure 5.5. Average of the number N_Y of poles on the imaginary axis for an $N \times N$ scattering matrix $S(\varepsilon)$ in symmetry class D. Colors distinguish different tunnel couplings $\Gamma < 1$, and N is increased together with $M = 80\,N$. The slope of the dashed black line is the large-N asymptote (5.21).

[30–32] (real Gaussian matrices without any symmetry) and the Hamilton ensemble [33] (matrices of the form $\mathcal{M} = HJ$ with H a symmetric real Gaussian matrix and $J = \begin{pmatrix} 0 & 1 \\ -1 & 0 \end{pmatrix}$ a fixed anti-symmetric matrix). Fig. 5.5 shows that the Andreev resonances follow the same square-root law.

5.4 X-shaped and Y-shaped conductance profiles

In Ref. [7] it was found in a computer simulation of a superconducting InSb nanowire that the conductance resonances trace out two distinct profiles in the voltage-magnetic field plane: an X-shape or a Y-shape. In the X-shaped profile a pair of conductance resonances merges and immediately splits again upon variation of voltage V or magnetic field B. In the Y-shaped profile a pair of peaks merges at $V = 0$ and then stays

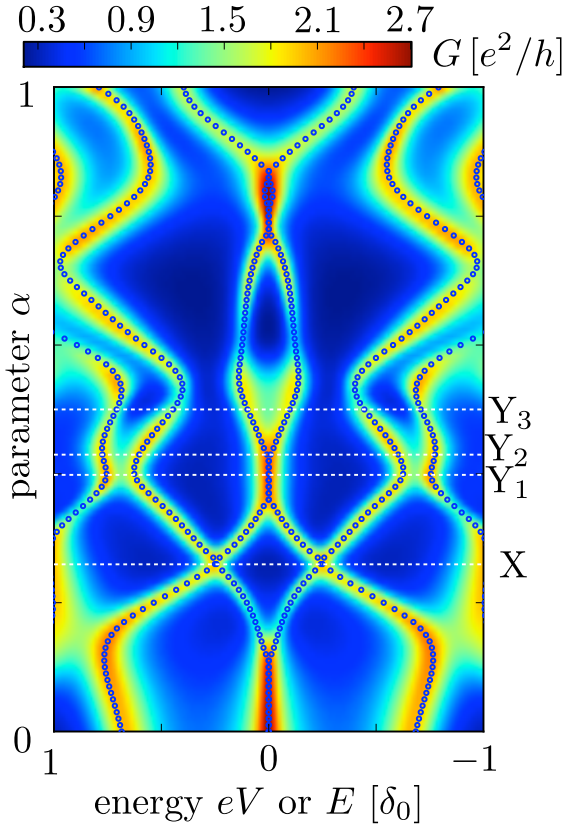

Figure 5.6. Parametric evolution of the differential conductance $G(V,\alpha)$ (color scale) and the real part E of the poles of the scattering matrix $S_\alpha(\varepsilon)$. These are results for a single realization of the class D ensemble with $M = 120$, $N = 6$, and $\Gamma = 0.3$.

pinned to zero voltage over a range of magnetic field values. Here we wish to relate this phenomenology to the parametric evolution of poles of the scattering matrix in the complex energy plane [12].

For that purpose we introduce a parameter dependence in the Hamiltonian H of the Andreev billiard,

$$H_\alpha = (1-\alpha)H_0 + \alpha H_1, \tag{5.22}$$

and calculate the differential conductance as a function of V and α. We work in symmetry class D (broken time-reversal and broken spin-rotation symmetry), so H_0 and H_1 are purely imaginary antisymmetric matrices

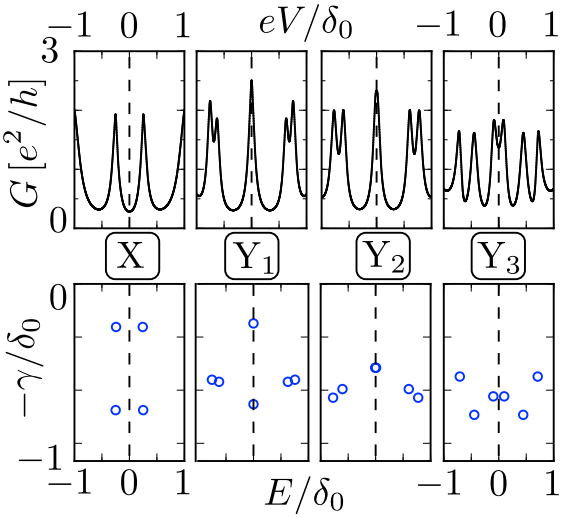

Figure 5.7. Four cuts through the parametric evolution of Fig. 5.6, showing the differential conductance $G = dI/dV$ (top row) and scattering matrix poles $\varepsilon = E - i\gamma$ (bottom row).

(in the Majorana basis). We draw them from the Gaussian distribution (5.12). The scattering matrix S_α, obtained from H_α via Eq. (5.2), gives the differential conductance $G(V, \alpha)$ via Eq. (5.5). For each α we also compute the poles $\varepsilon = E - i\gamma$ of $S(\varepsilon)$ in the complex energy plane.

Fig. 5.6 shows a typical realization where the number N_Y of conductance poles on the imaginary axis switches between zero and two when α varies in the interval $[0, 1]$. The color-scale plot shows $G(V, \alpha)$, while the dots trace out the projection of the poles of $S_\alpha(\varepsilon)$ on the real axis. Labels X and Y indicate the two types of profiles, and Fig. 5.7 shows the corresponding conductance peaks and scattering matrix poles.

Inspection of the figures shows that the X-shaped profile appears when two scattering matrix poles cross when projected onto the real axis. (They do not cross in the complex energy plane.) The Y-shaped profile appears when N_Y jumps by two.

5.5 Conclusion

For a closed superconducting quantum dot, the distinction between topologically trivial and nontrivial is the absence or presence of a level

pinned to the middle of the gap (a Majorana zero-mode). When the quantum dot is connected to a metallic reservoir, the bound states become quasi-bound, $E \mapsto E - i\gamma$, with a finite life time $\hbar/2\gamma$. The distinction between topologically trivial and nontrivial then becomes whether the number N_Y of quasi-bound states with $E = 0$ is even or odd.

One can now distinguish two types of transitions [12]: At a topological phase transition N_Y changes by ± 1 [21]. At a "pole transition" N_Y changes by ± 2. Both types of transitions produce the same Y-shaped conductance profile of two peaks that merge and stick together for a range of parameter values — distinct from the X-shaped profile that happens without a change in N_Y.

There is a variety of methods to distinguish the pole transition from the topological phase transition [7]: Since $N_Y \simeq \Gamma^{3/2}\sqrt{N}$ for $\Gamma \ll 1$, one way to suppress the pole transitions is to couple the metal to the superconductor via a small number of modes N with a small transmission probability Γ. The pole transitions are a sample-specific effect, while the topological phase transition is expected to be less sensitive to microscopic details of the disorder. One would therefore not expect the pole transitions to reproduce in the same sample upon thermal cycling. If one can measure from both ends of a nanowire, one might search for correlations between the conductance peaks at the two ends. The Majorana zero-modes come in pairs, one at each end, so there should be a correlation in the conductance peaks measured at the two ends, which we would not expect to be there for the peaks due to the pole transition.

5.6 Appendix

5.6.1 Factor-of-two difference in the construction of Gaussian ensembles with or without particle-hole symmetry

As we discussed in Sec. 5.2.2, in the Gaussian ensembles of random-matrix theory the Hermitian $M \times M$ matrix H has distribution

$$P(H) \propto \exp\left(-\frac{c}{M}\operatorname{Tr} H^2\right), \tag{5.23a}$$

$$c = \frac{\beta\pi^2}{8\delta_0^2} \times \begin{cases} 2 & \text{in the Wigner-Dyson ensembles,} \\ 1 & \text{in the Altland-Zirnbauer ensembles,} \\ 1 & \text{in the chiral ensembles.} \end{cases} \tag{5.23b}$$

In each ensemble δ_0 refers to the average spacing of distinct eigenvalues of H in the bulk of the spectrum. For $\beta = 4$ the eigenvalues have a twofold Kramers degeneracy, so there are only $M_0 = M/2$ distinct eigenvalues, while for $\beta = 1, 2$ all $M_0 = M$ eigenvalues are distinct (disregarding spin degeneracy).

We have experienced that the factor-of-two difference in the coefficient between the Wigner-Dyson (WD) and Altland-Zirnbauer (AZ) ensembles is a source of confusion. Here we hope to resolve this confusion by pointing to its origin, which is the $\pm E$ symmetry of the spectrum in the AZ ensembles (and also in the chiral ensembles, which we include for completeness). The calculation of the coefficient c is a bit lengthy, with factors of two appearing at different places before the final factor remains, but we have not found a much shorter and convincing argument for the difference.

The eigenvalue distribution in the WD ensembles is [16–18]

$$P(E_1, E_2, \dots E_{M_0}) \propto \prod_{1=i<j}^{M_0} |E_i - E_j|^\beta \prod_{k=1}^{M_0} e^{-\frac{c}{M_0} E_k^2}, \tag{5.24}$$

where the indices i, j, k range over the M_0 distinct eigenvalues.

In the AZ ensembles an eigenvalue at $+E$ has a partner at $-E$, which is a distinct eigenvalue if $E \neq 0$. For the average level spacing in the bulk of the spectrum the existence of a level pinned at $E = 0$ is irrelevant, so we assume that there are no such zero-modes. (This requires M_0 even.) The eigenvalue distribution then has the form [19, 20]

$$\begin{aligned} P(E_1, E_2, \dots E_{M_0/2}) \propto & \prod_{1=i<j}^{M_0/2} |E_i^2 - E_j^2|^\beta \\ & \times \prod_{k=1}^{M_0/2} |E_k|^\alpha \exp\left(-\frac{2c}{M_0} E_k^2\right), \end{aligned} \tag{5.25}$$

where now the indices i, j, k range only over the $M_0/2$ distinct positive eigenvalues. There is a new exponent $\alpha \in \{0, 1, 2\}$ that governs the repulsion between eigenvalues related by $\pm E$ symmetry. This factor $|E_k|^\alpha$ only affects the first few levels around $E = 0$, so we may ignore it for a calculation of the average level spacing in the bulk of the spectrum, effectively setting $\alpha \to 0$.

The two distributions (5.24) and (5.25) may be written in the same form with the help of the microscopic level density

$$\rho(E) = \sum_{n=1}^{M_0} \delta(E - E_n), \tag{5.26}$$

defined for each set of M_0 distinct energy levels. At the mean-field level, sufficient for a calculation of the density of states in the large-M limit, we may assume that $\rho(E)$ is a smooth function of E (Coulomb gas model [16]).

The eigenvalue distribution has the form of a Gibbs distribution $P \propto \exp(-\beta U)$, with energy functional

$$\begin{aligned} U_{\mathrm{WD}} = & -\frac{1}{2}\int_{-\infty}^{\infty} dE \int_{-\infty}^{\infty} dE'\, \rho(E)\rho(E') \ln|E - E'| \\ & + \frac{c}{\beta M_0}\int_{-\infty}^{\infty} dE\, E^2 \rho(E), \end{aligned} \tag{5.27}$$

for the WD ensembles and

$$\begin{aligned} U_{\mathrm{AZ}} = & -\frac{1}{2}\int_{0}^{\infty} dE \int_{0}^{\infty} dE'\, \rho(E)\rho(E') \ln|E^2 - E'^2| \\ & + \frac{2c}{\beta M_0}\int_{0}^{\infty} dE\, E^2 \rho(E) \\ = & -\frac{1}{4}\int_{-\infty}^{\infty} dE \int_{\infty}^{\infty} dE'\, \rho(E)\rho(E') \ln|E - E'| \\ & + \frac{c}{\beta M_0}\int_{-\infty}^{\infty} dE\, E^2 \rho(E), \end{aligned} \tag{5.28}$$

for the AZ ensembles (at $\alpha = 0$). In the second equality we used the $\pm E$ symmetry $\rho(E) = \rho(-E)$.

The mean-field density of states $\bar{\rho}(E)$ minimizes U with the normalization constraint

$$\int_{-\infty}^{\infty} dE\, \bar{\rho}(E) = M_0. \tag{5.29}$$

The normalization constraint is the same in the WD and AZ ensembles,

but the minimization condition is different:

$$\frac{\delta U_{\rm WD}}{\delta\rho(E)} = 0 \Rightarrow -\int_{-\infty}^{\infty} dE'\,\bar\rho_{\rm WD}(E')\ln|E-E'| + \frac{c}{\beta M_0}E^2 = \text{constant}, \tag{5.30}$$

$$\frac{\delta U_{\rm AZ}}{\delta\rho(E)} = 0 \Rightarrow -\frac{1}{2}\int_{-\infty}^{\infty} dE'\,\bar\rho_{\rm AZ}(E')\ln|E-E'| + \frac{c}{\beta M_0}E^2 = \text{constant}. \tag{5.31}$$

The $\pm E$ symmetry does not introduce an additional constraint on $\bar\rho_{\rm AZ}(E)$, since Eq. (5.31) automatically produces an even density.

The solution to this integral equation gives the familiar semi-circular density of states [16],

$$\bar\rho_{\rm WD}(E) = \frac{2c}{\pi\beta M_0}\sqrt{(\beta/c)M_0^2 - E^2}, \tag{5.32}$$

$$\bar\rho_{\rm AZ}(E) = \frac{4c}{\pi\beta M_0}\sqrt{(\beta/2c)M_0^2 - E^2}. \tag{5.33}$$

The mean level spacing near $E = 0$ is $\delta_0 = 1/\bar\rho(0)$, leading to

$$\begin{aligned}\delta_0 &= \frac{1}{2}\pi\sqrt{\beta/c} \ \text{ in the WD ensembles,}\\ \delta_0 &= \frac{1}{2}\pi\sqrt{\beta/2c} \ \text{ in the AZ ensembles,}\end{aligned} \tag{5.34}$$

which amounts to Eq. (5.23b). Notice that the additional factor-of-two arises solely from $\pm E$ symmetry of the spectrum, so it does not matter whether this is a consequence of particle-hole symmetry or of chiral symmetry.

To check that we have not missed a factor of two, we show in Fig. 5.8 the numerical result of an average over a large number of random Hamiltonians in each of the four Altland-Zirnbauer ensembles. The semi-circular density of states (5.33) applies away from the band center, with the expected limit $\rho \times \delta_0 \to 1$ near $E = 0$.

We also see in Fig. 5.8 the anomalies at band center that we ignored in our calculation. Without a zero-mode ($\nu = 0$) the density of states vanishes as $|E|^\alpha$ with $\alpha = 2$ in class C and $\alpha = 1$ in class CI and DIII [19]. In class D one has $\alpha = 0$, which means that the $\pm E$ pairs of energy levels

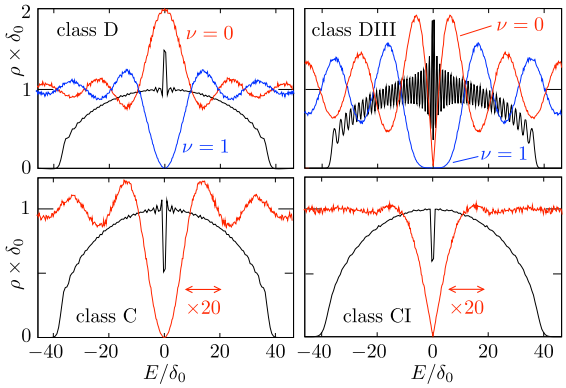

Figure 5.8. Black and red curves: Average density of states in the four Altland-Zirnbauer ensembles, calculated numerically for Hamiltonians of dimension $M \times M = 60 \times 60$ in classes C, CI, D, and $M \times M = 120 \times 120$ in class DIII (when each level has a twofold Kramers degeneracy; ρ and δ_0 refer to distinct levels). The black curve shows the full semicircle, the red curve shows the region around $E = 0$ (horizontally enlarged by a factor 20). These are all results for a topologically trivial superconductor, without a zero-mode ($\nu = 0$). The blue curves (labeled $\nu = 1$) show the effect of a zero-mode in class D ($M = 61$) and class DIII ($M = 122$). The delta-function peak from the zero-mode itself is not plotted.

do not repel at the band center. The density of states then has a quadratic peak at $E = 0$. The delta-function peak of a zero-mode has also an effect on the smooth part of the density of states, which for $\nu = 1$ vanishes as $|E|^{\alpha+\beta}$, so as E^2 in class D and as $|E|^5$ in class DIII [20].

5.6.2 Altland-Zirnbauer ensembles with time-reversal symmetry

For completeness and reference, we record the $\beta = 1, 4$ counterparts of the $\beta = 2$ formulas (5.12) and (5.15). These are the Altland-Zirnbauer symmetry classes CI ($\beta = 1$, time-reversal with spin-rotation symmetry) and DIII ($\beta = 4$, time-reversal without spin-rotation symmetry) [19]. The time-reversal symmetry conditions on the Hamiltonian matrix are

$$\begin{aligned} H &= H^* \quad \text{for} \quad \beta = 1, \\ H &= \sigma_y H^* \sigma_y \quad \text{for} \quad \beta = 4. \end{aligned} \tag{5.35}$$

The Pauli matrix σ_y acts on the spin degree of freedom — the Pauli matrices τ_i we used earlier acted on the electron-hole degree of freedom.

A compact representation can be given if we use the electron-hole basis for $\beta = 1$ and the Majorana basis for $\beta = 4$. The matrix elements of the Hamiltonian can then be represented by Pauli matrices:

$$\begin{aligned} H_{nm} &= a_{nm}\tau_x + b_{nm}\tau_z \quad \text{for} \quad \beta = 1, \\ H_{nm} &= ic_{nm}\sigma_x + id_{nm}\sigma_z \quad \text{for} \quad \beta = 4, \end{aligned} \tag{5.36}$$

with real coefficients a, b, c, d. Notice that iH for $\beta = 1$ is quaternion, so this class CI ensemble is a subset of the class C ensemble. Similarly, because iH is real for $\beta = 4$, this class DIII ensemble is a subset of class D.

Hermiticity of H requires that the off-diagonal elements are related by $a_{nm} = a_{mn}$, $b_{nm} = b_{mn}$, $c_{nm} = -c_{mn}$, $d_{nm} = -d_{mn}$. On the diagonal $c_{nn} = d_{nn} = 0$. The indices n, m range from 1 to $M/2$, for an $M \times M$ matrix H. (The dimensionality is necessarily even to accomodate the Pauli matrices.) For $\beta = 4$ there is a twofold Kramers degeneracy of the energy levels, so only $M/2$ eigenvalues of H are distinct. For $\beta = 1$ all M eigenvalues are distinct (the spin degeneracy that exists in class C, CI is not included in M). The mean level spacing δ_0 refers to the distinct eigenvalues.

Combination of Eq. (5.36) with Eqs. (5.7) and (5.8) gives the probability distribution of the independent matrix elements in the Gaussian ensemble:

$$\begin{aligned} P(\{H_{nm}\}) \propto \prod_{n=1}^{M/2} \exp\left(-\frac{\pi^2}{4M\delta_0^2}(a_{nn}^2 + b_{nn}^2)\right) \\ \times \prod_{1=n<m}^{M/2} \exp\left(-\frac{\pi^2}{2M\delta_0^2}(a_{nm}^2 + b_{nm}^2)\right), \end{aligned} \tag{5.37}$$

for $\beta = 1$, class CI, and

$$P(\{H_{nm}\}) \propto \prod_{1=n<m}^{M/2} \exp\left(-\frac{2\pi^2}{M\delta_0^2}(c_{nm}^2 + d_{nm}^2)\right), \tag{5.38}$$

for $\beta = 4$, class DIII.

5.6.3 Mapping of the pole statistics problem onto the eigenvalue statistics problem of truncated orthogonal matrices

We show how the result (5.20) for the density profile of imaginary poles of the scattering matrix follows from the known distribution of real eigenvalues of truncated orthogonal matrices [27] — for the case $\Gamma = 1$ of ballistic coupling.

Following Ref. [34] we construct the $N \times N$ energy-dependent unitary scattering matrix $S(E)$ in terms of an $M \times M$ energy-independent orthogonal matrix O,

$$S(E) = \mathcal{P}O(e^{-2\pi i E/M\delta_0} + \mathcal{R}O)^{-1}\mathcal{P}^{\mathrm{T}}. \tag{5.39}$$

The rectangular $N \times M$ matrix $\mathcal{P}$ has elements $\mathcal{P}_{nm} = \delta_{nm}$ and $\mathcal{R} = 1 - \mathcal{P}^{\mathrm{T}}\mathcal{P}$. The $M \times M$ Hermitian matrix H is related to O via a Cayley transform,

$$O = \frac{\pi H/M\delta_0 + i}{\pi H/M\delta_0 - i} \Leftrightarrow H = \frac{iM\delta_0}{\pi}\frac{O+1}{O-1}. \tag{5.40}$$

Eq. (5.40) with O uniformly distributed according to the Haar measure in $\mathrm{SO}(N)$ produces the Gaussian distribution (5.7) for H, in the low-energy range $|E| \lesssim N\delta_0 \ll M\delta_0$. Furthermore, in this low-energy range the scattering matrix (5.39) is related to H by Eq. (5.2) with ballistic coupling matrix $W = \mathcal{P}^{\mathrm{T}}(M\delta_0/\pi^2)^{1/2}$.

A pole $\varepsilon = -i\gamma$ of $S(\varepsilon)$ on the imaginary axis corresponds to a real eigenvalue

$$x = e^{-2\pi\gamma/M\delta_0} \tag{5.41}$$

of the $(M-N)\times(M-N)$ matrix $\tilde{O} = \mathcal{R}O\mathcal{R}$ obtained from the orthogonal matrix O by deleting the first N rows and columns. For $M \gg 1$ the x-dependent density $\tilde{\rho}_0(x)$ is given by [27]

$$\tilde{\rho}_0(x) = \frac{1}{B(N/2,1/2)}\frac{1}{1-x^2}, \quad x^2 < 1 - N/M, \tag{5.42}$$

with $B(a,b)$ the beta function.

Using Eq. (5.41) we thus arrive for $N \ll M$ at the γ-dependent density

$$\rho_0(\gamma) = \frac{1}{B(N/2,1/2)}\frac{1}{2\gamma}, \quad \gamma > N\delta_0/4\pi. \tag{5.43}$$

Eq. (5.20) with $\Gamma = 1$ results if we also assume that $N \gg 1$, so that we may approximate $B(N/2,1/2) \approx (2\pi/N)^{1/2}$.

Bibliography

[1] A. F. Andreev, Zh. Eksp. Teor. Fiz. **46**, 1823 (1964) [Sov. Phys. JETP **19**, 1228 (1964)].

[2] M. Silaev and G. E. Volovik, arXiv:1405.1007.

[3] J. Alicea, Rep. Progr. Phys. **75**, 076501 (2012).

[4] M. Leijnse and K. Flensberg, Semicond. Science Technol. **27**, 124003 (2012).

[5] T. D. Stanescu and S. Tewari, J. Phys. Condens. Matter **25**, 233201 (2013).

[6] C. W. J. Beenakker, Annu. Rev. Con. Mat. Phys. **4**, 113 (2013).

[7] D. I. Pikulin, J. P. Dahlhaus, M. Wimmer, H. Schomerus, and C. W. J. Beenakker, New J. Phys. **14**, 125011 (2012).

[8] P. W. Brouwer and C. W. J. Beenakker, Phys. Rev. B **52**, 3868 (1995).

[9] A. Altland and M. R. Zirnbauer, Phys. Rev. Lett. **76**, 3420 (1996).

[10] P. A. Ioselevich, P. M. Ostrovsky, and M. V. Feigel'man, Phys. Rev. B **86**, 035441 (2012).

[11] D. Bagrets and A. Altland, Phys. Rev. Lett. **109**, 227005 (2012).

[12] D. I. Pikulin and Yu. V. Nazarov, JETP Lett. **94**, 693 (2011); Phys. Rev. B **87**, 235421 (2013).

[13] C. W. J. Beenakker, Lect. Notes Phys. **667**, 131 (2005) [arXiv:cond-mat/0406018].

[14] T. Guhr, A. Müller-Groeling, and H. A. Weidenmüller, Phys. Rep. **299**, 189 (1998).

[15] C. W. J. Beenakker, Rev. Mod. Phys. **69**, 731 (1997).

[16] M. L. Mehta, *Random Matrices* (Elsevier, Amsterdam, 2004).

[17] P. J. Forrester, *Log-Gases and Random Matrices* (Princeton University Press, 2010).

[18] *The Oxford Handbook of Random Matrix Theory*, edited by G. Akemann, J. Baik, and P. Di Francesco (Oxford University Press, Oxford, 2011). Chapters relevant for this work are by Y. V. Fyodorov and D. V. Savin [arXiv:1003.0702]; M. R. Zirnbauer [arXiv:1001.0722]; C. W. J. Beenakker [arXiv:0904.1432].

[19] A. Altland and M. R. Zirnbauer, Phys. Rev. B **55**, 1142 (1997).

[20] D. A. Ivanov, J. Math. Phys. **43**, 126 (2002).

[21] Since Majorana zero-modes always appear in pairs, the change from M even to M odd necessarily involves some external system that can absorb one of the two Majoranas. For example, this could be a nanowire coupled at one end to the quantum dot, so that the Majorana zero-mode inside the quantum dot is paired with the zero-mode at the other end of the wire. At the transition from M odd to even the two Majoranas merge because the gap in the nanowire closes.

[22] S. Ryu, A. P. Schnyder, A. Furusaki, and A. W. W. Ludwig, New J. Phys. **12**, 065010 (2010).

[23] M. Z. Hasan and C. L. Kane, Rev. Mod. Phys. **82**, 3045 (2010).

[24] X.-L. Qi and S.-C. Zhang, Rev. Mod. Phys. **83**, 1057 (2011).

[25] Y. V. Fyodorov and H.-J. Sommers, J. Math. Phys. **38**, 1918 (1997).

[26] The usual Kramers degeneracy refers to the eigenvalues of a Hermitian matrix that commutes with an anti-unitary operator squaring to -1. Here the matrix is not Hermitian, but the degeneracy still applies to real eigenvalues.

[27] B. A. Khoruzhenko, H.-J. Sommers, and K. Zyczkowski, Phys. Rev. E **82**, 040106(R) (2010).

[28] P. J. Forrester, J. Stat. Mech. P12018 (2010).

[29] The logarithmic divergence in Eq. (5.21) for $\Gamma = 1$ is cut-off by the finite dimension M of the Hamiltonian, so that $\langle N_Y \rangle \simeq N^{1/2} \ln(M/N)$ for ballistic coupling. This spurious M-dependence does not exist for $\Gamma < 1$.

[30] J. Ginibre, J. Math. Phys. **6**, 440 (1965).

[31] N. Lehmann and H.-J. Sommers, Phys. Rev. Lett. **67**, 2403 (1991).

[32] A. Edelman, E. Kostlan, and M. Shub, J. Am. Math. Soc. **7**, 247 (1994); A. Edelman, J. Multivariate Anal. **60**, 203 (1997).

[33] C. W. J. Beenakker, J. M. Edge, J. P. Dahlhaus, D. I. Pikulin, S. Mi, and M. Wimmer, Phys. Rev. Lett. **111**, 037001 (2013). The supplement to this paper (an appendix in arXiv:1305.2924) contains an overview of the square-root law in a variety of random-matrix ensembles.

[34] P. W. Brouwer, K. M. Frahm, and C. W. J. Beenakker, Waves in Random Media **9**, 91 (1999). See also App. A1 of M. Marciani, P. W. Brouwer, and C. W. J. Beenakker, arXiv:1405.3115.

Chapter 6

Single fermion manipulation via superconducting phase differences in multiterminal Josephson junctions

6.1 Introduction

In quantum mechanics, Kramers' theorem guarantees that in presence of time reversal symmetry the energy levels of a system with half-integer spin are doubly degenerate even if the spin rotation symmetry is broken [1, 2]. A practical consequence of this theorem is that it is necessary to break time reversal symmetry in order to control single fermion states in a condensed matter system. The energy separation of different spin states opens the way to spin detection and manipulation and is often a necessary element for spin qubits [3] and spintronics [4, 5]. The absence of Kramers degeneracy is also a fundamental requirement for the creation of unpaired Majorana bound states in topological superconductors [6, 7].

In order to provide fine-grained manipulation of electron states, a source of time reversal symmetry breaking should be local in space and easily tunable in time. The superconducting phase difference across a Josephson junction satisfies these requirements. It allows one to concentrate the effect of a magnetic flux penetrating a large superconducting ring into the small area of the Josepshon junction, whose spatial ex-

tent may be comparable to the superconducting coherence length ξ (see Fig. 6.1). The magnitude of the energy splitting between a Kramers pair of bound states in the junction can then be comparable to the superconducting gap Δ. The magnetic field required to control the superconducting phase difference is rather small, and may be vanishing in the junction itself. Flux bias loops applying this magnetic field allow one to address different Josephson junctions independently by tuning different fluxes, and have nanosecond response times. These features seemingly make the superconducting phase difference the perfect source of time-reversal symmetry breaking for the manipulation of single fermion states. In contrast, an external magnetic magnetic field seems to lose to phase differences in most respects: it needs to be a fraction of a Tesla to achieve a Zeeman splitting comparable to Δ. Such a field can only be tuned on the time scale of seconds and is rather hard to apply locally to only a part of a mesoscopic system.

Short Josephson junctions with Thouless energy E_T much larger than the superconducting gap Δ are the most promising for single fermion manipulation, since they have the largest level spacing $\delta E \sim \Delta$. Unfortunately, using phase difference as a source of time reversal symmetry breaking is ineffective in short two-terminal Josephson junctions. This fact might seem surprising, since using symmetry considerations alone one would expect the spectrum of the Andreev bound states to be non-degenerate at a finite phase difference ϕ. As is well known, however, this expectation does not hold. The Andreev energy levels ϵ_k are in one-to-one correspondence with the transmission eigenvalues T_k of the scattering matrix of the junction in the normal state [8]:

$$\epsilon_k = \pm\Delta \left[1 - T_k \sin^2(\phi/2)\right]^{1/2} . \tag{6.1}$$

In the absence of time reversal symmetry breaking in the normal state, the transmission eigenvalues T_k are Kramers degenerate (see Ref. [9] for a concise proof), and hence so are the Andreev levels. Relaxing the short junction condition changes the scenario: spin-orbit coupling couples the spin of the bound states to the phase difference and lifts the Kramers degeneracy of the Andreev spectrum, albeit by a small amount of the order Δ^2/E_T [10, 11]. Therefore, time-reversal symmetry can be broken only very weakly in a two-terminal junction.

In this work, we show how this serious limitation can be removed with a simple yet crucial change in the device geometry: the addition of

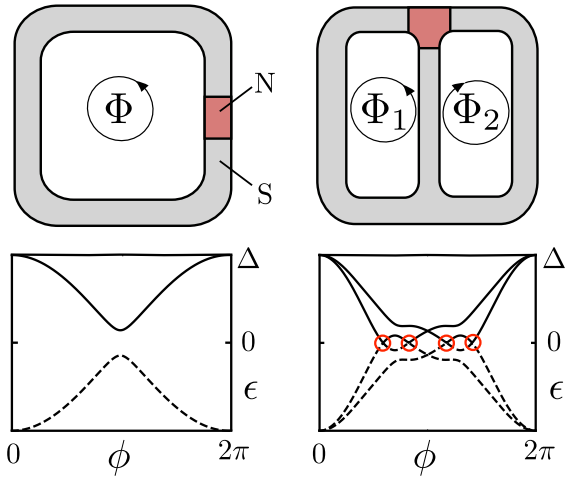

Figure 6.1. *Top left*: A superconducting ring (grey) allows one to concentrate the effect of a magnetic flux Φ on the small area of a Josephson junction (red). *Bottom left*: The junction has subgap Andreev levels whose energy ϵ depends on the phase difference $2e\Phi/\hbar = \phi$. Each level is doubly degenerate since in a short junction a finite phase difference does not induce a splitting of the Kramers degeneracy. *Top right:* As explained in this work, Kramers degeneracy can be efficiently removed in a three-terminal junction, even in the absence of an external magnetic field. *Bottom right:* Andreev spectrum for $2e\Phi_1/\hbar = -2e\Phi_2/\hbar = \phi$. Both the splitting of Kramers degeneracy and Andreev level crossings at zero energy (marked by red circles) appear in the spectrum.

an extra superconducting lead, as shown in Fig. 6.1. Indeed, in devices with more than two superconducting terminals, the energy spectrum is not expected anymore to be in one-to-one correspondence with transmission eigenvalues. We demonstrate that in this case the effect of time reversal symmetry breaking by superconducting phase differences alone leads to large splitting of the Kramers doublets comparable to the superconducting gap Δ. Naturally, since breaking the spin-rotation symmetry remains necessary, spin-orbit coupling is still an essential ingredient. The non-degenerate Andreev spectrum makes these three-terminal junctions a promising platform for superconducting spin qubits [10, 12, 13] and the creation of Majorana bound states, as we will discuss further in Sec. 6.4.

As a consequence of the strong splitting of the Kramers degeneracy, crossings at the Fermi level can appear in the Andreev spectrum, corre-

sponding to a switch in the ground state fermion parity [14, 15]. We find that a necessary condition for the existence of a crossing at the Fermi level is the presence of a discrete vortex in the junction. In other words, the gap in the Andreev spectrum can only close when the superconducting phases of the leads wind by 2π around the junction. If this condition is satisfied, the spectral peaks in the density of states of the junction develop at the Fermi level as expected [16, 14, 17, 18] for a superconducting quantum dot with broken time-reversal and spin-rotation symmetries (symmetry class D of the Altland-Zirnbauer classification [14]).

6.2 General considerations

6.2.1 Scattering formalism and bound state equation for multiterminal Josephson junctions

Three terminal Josephson junctions, such as the one shown in Fig. 6.2, are the main focus of our work. However, since most of our conclusions generalize naturally to the case of more terminals, we consider a junction with m superconducting leads. We assume that all of the leads have the same energy gap Δ and different phases $\phi_1, \ldots, \phi_m$. The coupling between the superconducting leads through the normal scattering region is fully characterized by the electron scattering matrix $s(\epsilon)$, with ϵ the excitation energy. In general $s(\epsilon)$ is a $n \times n$ unitary matrix. Its size $n = n_1 + \cdots + n_m$ is the sum of the number of incoming modes in the leads, counting spin. The integers $n_1, \ldots, n_m$ must be even due to the fermion doubling theorem [19].

When $|\epsilon| < \Delta$, an electron escaping the scattering region must be reflected back as a hole at the interface with the superconductor [1]. Closed trajectories of electron and hole superposition form Andreev bound states in the junction, which are confined by the superconducting pairing potential in the leads. The spectrum of Andreev bound states can be expressed through two distinct scattering matrices: that of the scattering region s_N, and the scattering matrix s_A describing Andreev reflection from a superconducting interface. Both matrices are unitary and depend

[1] In the presence of normal scattering in the superconductor, reflection from the superconductor can be represented as a combination of normal scattering followed by a subsequent perfect Andreev reflection. The former component can be combined with the scattering matrix of the normal region. Therefore, assuming perfect Andreev reflection does not reduce the generality of our results.

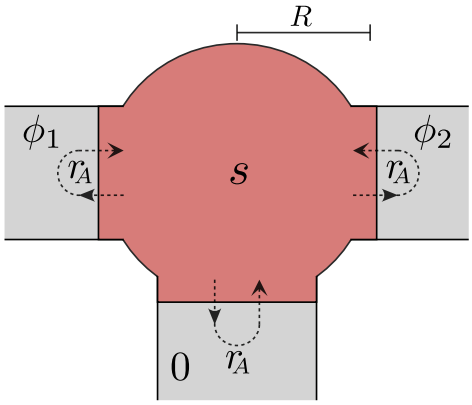

Figure 6.2. Three-terminal Josephson junction geometry. The scattering region (red) is a piece of a disordered two-dimensional material with spin-orbit coupling. It is connected to three superconducting leads (grey). In the normal state, the scattering region has a scattering matrix s. At energies smaller than the superconducting gap Δ, modes leaving the scattering region are reflected at the interface with the superconductor by Andreev reflection processes (black arrows), described by a scattering matrix r_A.

on the energy ϵ. As derived in Ref. [8], the condition for a presence of the bound state is given by:

$$s_A(\epsilon)\, s_N(\epsilon)\, \Psi_{\text{in}} = \Psi_{\text{in}}\,. \tag{6.2}$$

Here, $\Psi_{\text{in}} = (\Psi^e_{\text{in}}, \Psi^h_{\text{in}})$ is a vector of complex coefficients describing a wave incident on the junction in the basis of the modes incoming from the superconducting leads into the normal region.

Since in the normal region electrons and holes are not coupled, s_N is block-diagonal in the electron-hole space. We choose the hole modes as particle-hole partners of the electron modes and obtain

$$s_N(\epsilon) = \begin{pmatrix} s(\epsilon) & 0 \\ 0 & s^*(-\epsilon) \end{pmatrix}. \tag{6.3}$$

For more details regarding the relation between the basis choice for a scattering matrix and its discrete symmetries, see App. A of Ref. [20]. In the same basis, the Andreev scattering matrix s_A is block off-diagonal since it couples only electron to holes and vice versa,

$$s_A(\epsilon) = \alpha(\epsilon) \begin{pmatrix} 0 & r_A^* \\ r_A & 0 \end{pmatrix}. \tag{6.4}$$

The phase factor $\alpha(\epsilon) = \sqrt{1-\epsilon^2/\Delta^2} + i\epsilon/\Delta$ is due to the matching of the wave function at the interface between the normal region and the superconductors [8].

In the short junction limit, the energy dependence of the scattering matrix elements can be neglected,

$$s(\epsilon) \simeq s(-\epsilon) \simeq s(0) \equiv s\,. \tag{6.5}$$

In that case the set of discrete Andreev levels $\{\epsilon_k\}$ can be computed by substituting Eqs. (6.3,6.4) into Eq. (6.2) and solving the resulting eigenproblem for α :

$$\begin{pmatrix} s^\dagger & 0 \\ 0 & s^T \end{pmatrix} \begin{pmatrix} 0 & r_A^* \\ r_A & 0 \end{pmatrix} \Psi_{\rm in} = \alpha \Psi_{\rm in}\,. \tag{6.6}$$

It is convenient to apply to the above problem the Joukowsky transform

$$X \;\rightarrow\; -\frac{i}{2}\left(X - X^{-1}\right)\,, \tag{6.7}$$

which maps α to ϵ/Δ. In this way, we obtain an eigenproblem directly for ϵ :

$$\begin{pmatrix} 0 & -iA^\dagger \\ iA & 0 \end{pmatrix} \Psi_{\rm in} = \frac{\epsilon}{\Delta}\,\Psi_{\rm in}, \tag{6.8}$$

with

$$A \equiv \tfrac{1}{2}\left(r_A s - s^T r_A\right). \tag{6.9}$$

Since A is a normal matrix ($AA^\dagger = A^\dagger A$), its eigenvalues are equal to its singular values up to a phase, and as follows from (6.8) its singular values are equal to $|\epsilon|$. We now arrive at the simplified eigenvalue problem for the energies of Andreev levels:

$$A\,\Psi^e_{\rm in} = \frac{|\epsilon|}{\Delta}\,\mathrm{e}^{i\chi}\,\Psi^e_{\rm in} \tag{6.10}$$

The double degeneracy of the singular values of A is a consequence of the fact that the eigenvalues of Eq. (6.6) come in complex conjugate pairs, while only α with a positive real part are physical. The reduction of the eigenproblem to the form of Eq. (6.10) is an important simplification which allows us to derive the properties of the Andreev spectrum of the junction.

In the normal state the time-reversal symmetry is preserved in the junction and can be used to further constraint the scattering matrix s, which belongs to the circular symplectic ensemble[21] (CSE, symmetry class AII). Choosing a basis such that the outgoing modes are the time-reversed partners of the incoming ones results in s becoming an antisymmetric matrix, $s = -s^T$. Correspondingly, A becomes the anticommutator of s and r_A:

$$A = \tfrac{1}{2}\{s, r_A\}\,. \tag{6.11}$$

Moreover, in the same basis in which s is antisymmetric, the Andreev reflection matrix r_A is diagonal,

$$r_A = \begin{pmatrix} i\,\mathrm{e}^{i\phi_1}\,\mathbf{1}_{n_1} & 0 & \dots & 0 \\ 0 & i\,\mathrm{e}^{i\phi_2}\,\mathbf{1}_{n_2} & \dots & 0 \\ \vdots & \vdots & \ddots & \vdots \\ 0 & 0 & \dots & i\,\mathrm{e}^{i\phi_m}\,\mathbf{1}_{n_m} \end{pmatrix}. \tag{6.12}$$

We are now prepared to build a theory of multiterminal Josephson junctions.

6.2.2 Kramers degeneracy splitting

For completeness, we first apply our formalism given by Eq. (6.10) to repeat the known result of the absence of the Kramers degeneracy splitting in two terminal short junctions. For $m = 2$, the Andreev reflection matrix r_A has only two distinct eigenvalues $i\,\mathrm{e}^{i\phi_1}$ and $i\,\mathrm{e}^{i\phi_2}$, with multiplicity n. [2]

In this case, we can use the polar decomposition of s [21]:

$$\begin{pmatrix} U_1 & 0 \\ 0 & V_1 \end{pmatrix} s \begin{pmatrix} U_2 & 0 \\ 0 & V_2 \end{pmatrix} = \begin{pmatrix} -\sqrt{1-T} & \sqrt{T} \\ \sqrt{T} & \sqrt{1-T} \end{pmatrix}. \tag{6.13}$$

Here, $U_{1,2}$ and $V_{1,2}$ are $n \times n$ unitary matrices, while $T = \mathrm{diag}\,(T_1, \dots, T_{n_1})$ is a $n \times n$ matrix with doubly-degenerate transmission eigenvalues T_k on its diagonal. Crucially, since

$$\begin{pmatrix} U_{1,2} & 0 \\ 0 & V_{1,2} \end{pmatrix} r_A = r_A \begin{pmatrix} U_{1,2} & 0 \\ 0 & V_{1,2} \end{pmatrix}, \tag{6.14}$$

[2] Generalization to unequal numbers of modes in two superconducting leads is straightforward, since in that case one of the leads will simply have several fully reflected modes leading to no extra Andreev bound states.

the polar decomposition of s carries on to A:

$$\begin{pmatrix} U_1 & 0 \\ 0 & V_1 \end{pmatrix} A \begin{pmatrix} U_2 & 0 \\ 0 & V_2 \end{pmatrix} = \begin{pmatrix} -\sqrt{1-T}\,\mathrm{e}^{i\phi_1} & \frac{1}{2}\sqrt{T}(\mathrm{e}^{i\phi_1}+\mathrm{e}^{i\phi_2}) \\ \frac{1}{2}\sqrt{T}(\mathrm{e}^{i\phi_1}+\mathrm{e}^{i\phi_2}) & \sqrt{1-T}\,\mathrm{e}^{i\phi_2} \end{pmatrix} . \quad (6.15)$$

Diagonalization of the right hand side then immediately yields the spectrum of Eq. (6.1).

It is easy to recognize that this derivation cannot be extended to the multiterminal case. Indeed, if r_A has more than two distinct eigenvalues, Eq. (6.14) does not hold anymore and there is no polar decomposition which can be simultaneously applied to both s and A. The correspondence between Andreev levels and transmission eigenvalues of s is then lost. As a consequence, we expect the spectrum of a multiterminal junction to consist of non-degenerate levels, unless the phases in the leads are tuned in such a way that the two-terminal case of only two distinct eigenvalues of r_A is restored.

If spin-rotation symmetry is strongly broken, and the phase differences are not small, there is no small parameter in the eigenproblem of Eq. (6.10) with more than two terminals. This means that the energy splitting between Kramers partners becomes comparable to the Andreev level spacing in the junction, and scales as Δ/n, the maximal possible value. A simple estimate shows that, as one would expect, the splitting of Kramers degeneracy obtained using superconducting phase differences may never exceed the normal level spacing in the scattering region. Indeed, for the junction to be in a short junction regime, Δ should be much smaller than the Thouless energy $n\delta_0$, with δ_0 the normal level spacing in the scattering region. This immediately gives an upper bound of δ_0 on the Kramers degeneracy breaking.

6.2.3 Lower bound on the energy gap and existence of zero-energy solutions

For the two-terminal case, Eq. (6.1) implies a lower bound $|\epsilon| \geq \Delta\cos(\phi/2)$ on the energy of the Andreev states, irrespective of the junction details. Inspecting Eq. (6.11), we see that when all ϕ_i are close to each other, r_A is an almost constant matrix, so that $\{s\,, r_A\}/2$ is almost unitary, and conse-

quently all of the Andreev energies are close to Δ. This suggests that it is natural to expect some lower bound for ϵ also in the multiterminal case.

To determine this lower bound, we rewrite the eigenvalue equation (6.10) as:

$$s\, r_A|\Psi\rangle + r_A|\Psi'\rangle = \frac{2|\epsilon|}{\Delta}\, \mathrm{e}^{i\chi}\, |\Psi\rangle\,, \tag{6.16a}$$

$$|\Psi'\rangle \equiv s\,|\Psi\rangle,\ \|\Psi\| = \left\|\Psi'\right\| = 1. \tag{6.16b}$$

The two above equations dictate that s is a linear mapping such that

$$|\Psi\rangle \xrightarrow{s} |\Psi'\rangle, \tag{6.17a}$$

$$r_A|\Psi\rangle \xrightarrow{s} \frac{2|\epsilon|}{\Delta}\, \mathrm{e}^{i\chi}\, |\Psi\rangle - r_A|\Psi'\rangle\,. \tag{6.17b}$$

Since s is unitary, these equations may be satisfied for given Ψ and Ψ' if and only if the scalar products between the vectors on the left and right hand sides of Eqs. (6.17) are preserved. Hence, a necessary and sufficient condition for the existence of a solution is

$$\langle\Psi|\, r_A\, |\Psi\rangle + \langle\Psi'|\, r_A\, |\Psi'\rangle = \frac{2|\epsilon|}{\Delta}\, \mathrm{e}^{i\chi}\, \langle\Psi'|\Psi\rangle\,. \tag{6.18}$$

Taking the absolute value on both sides and using the Cauchy-Schwarz inequality $|\langle\Psi'|\Psi\rangle| \leq \|\Psi'\|\|\Psi\| = 1$ yields the lower bound

$$|\epsilon| \geq \frac{1}{2}\,\Delta\left|\langle\Psi|\, r_A\, |\Psi\rangle + \langle\Psi'|\, r_A\, |\Psi'\rangle\right|. \tag{6.19}$$

We have thus reduced the problem of finding the lower bound with respect to a unitary matrix s to a problem of finding the lower bound with respect to two vectors.

The two scalar products in Eq. (6.19) are weighted sums of the eigenvalues of r_A with total weight equal to one. This means both these scalar products, as well as their averaged sum, is a point on a complex plane that must lie within a convex polygon whose vertices are the eigenvalues of r_A, see Fig. 6.3. We can now distinguish two possibilities, depending on whether the polygon covers the origin. If it does not, as in the left panel of Fig. 6.3, the energy spectrum has a lower bound $\epsilon_{\min}$ determined by the minimum distance of the polygon from the origin:

$$\epsilon_{\min} = \Delta \min_{ij} \left[\cos\frac{1}{2}(\phi_i - \phi_j)\,\right]. \tag{6.20}$$

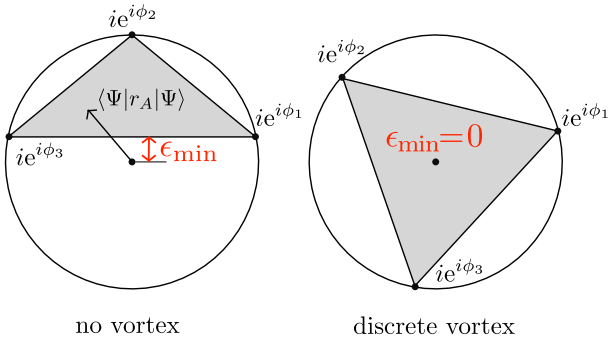

Figure 6.3. Geometrical illustration of Eq. (6.19) in the case of three leads. The sum of the scalar products $\frac{1}{2}\langle\Psi|r_A|\Psi\rangle$ and $\frac{1}{2}\langle\Psi'|r_A|\Psi'\rangle$ must lie within the triangle on the complex plane whose vertices are the eigenvalues $i\,e^{i\phi_1}, i\,e^{i\phi_2}, i\,e^{i\phi_3}$ of r_A. In the left panel, these phases do not surround the origin and the lowest allowed energy (in units of Δ) is the minimum distance between the polygon and the origin [Eq. (6.20)]. In the right panel, the phases surround the origin, a discrete vortex is present in the junction and zero-energy solutions are allowed.

On the other hand, if the polygon covers the origin, as in the right panel of Fig. 6.3, then a zero energy solution $\epsilon = 0$ is allowed. If we order $\phi_1 \leq \phi_2 \leq \cdots \leq \phi_m$ and introduce phase differences between closest phases $\theta_i = \phi_{i+1} - \phi_i \in (-\pi, \pi]$, this happens if

$$\sum_{i=1}^{m} \theta_i = 2\pi\,. \tag{6.21}$$

We call the situation of a non-zero winding of the superconducting phases in the leads a "discrete vortex".

Zero energy solutions are doubly degenerate and identify Andreev level crossings at Fermi energy. These crossings can be seen as topological transitions protected by fermion parity conservation. At the two sides of the gap closing point, the Pfaffian of the Hamiltonian has opposite signs, which means that energy of a single Andreev state must vanish at the transition point. Due to the number of modes in the leads being even, crossings can only occur in pairs when advancing any phase by 2π and for this reason the resulting ground state energy is 2π-periodic. Conversely, the 4π-periodic Josephson effect, a hallmark of topological superconductivity [22–24], requires an odd number of crossings in a 2π phase interval, the fermion parity anomaly.

We note that the results (6.20) and (6.21) are quite general: they hold for any number of leads and for arbitrary scattering matrices of the junction. Hence they are independent of any microscopic detail. The lower bound of Eq. (6.20) is only valid in the short junction limit, while Eq. (6.21) applies in fact to absolutely any Josephson junction since it is a Fermi level property.

6.2.4 Multiterminal Josephson junction in the quantum spin Hall regime

We observe that the lower bound (6.20) corresponds to the spectrum of a fully transmitted mode connecting two leads. This scenario can be realized in a quantum spin Hall insulator [25–28]. In this case the Andreev spectrum will depend only on the phase differences between adjacent leads that are connected by topologically protected helical edge states. In fact, a straightforward generalization of the two-terminal junction of Ref. [24] yields the Andreev spectrum

$$\epsilon_i = \pm\Delta \cos\left[\frac{1}{2}(\phi_{i+1} - \phi_i)\right], \quad i = 1 \ldots, m\,. \tag{6.22}$$

In a QSH insulator a crossing at zero energy occurs whenever one of the phase differences $\phi_{i+1} - \phi_i = \pi$ [see also the bottom left panel of Fig. (6.5)]. For a junction with three leads, this maximizes the region of the phase space with odd ground state fermion parity.

6.3 Applications

We now verify the results of the previous Section applied to junctions with three superconducting leads made in different physical systems. The physical systems that we study are: (i) chaotic quantum dots with random scattering matrices s uniformly sampled [29] from the circular symplectic ensemble, (ii) quantum dots made out of a quantum well with Rashba spin-orbit coupling, (iii) quantum dots made out of a quantum spin Hall insulator. In the latter two systems we obtain the scattering matrix numerically using a tight-binding simulation. We refer to these three systems as 'RMT', 'Rashba' or 'QSH' for brevity.

The Rashba Hamiltonian describing a 2D electron gas is given by

$$H = \frac{\mathbf{p}^2}{2m} + \alpha\left(p_x\sigma_y - p_y\sigma_x\right) - \mu + V(\mathbf{r})\,, \tag{6.23}$$

with $\mathbf{p} = (p_x, p_y)$ the momentum operator, σ_x and σ_y the spin Pauli matrices, α the strength of the spin-orbit coupling, and μ the chemical potential. The disordered electrostatic potential is given by $V(\mathbf{r})$. This Hamiltonian has time-reversal symmetry with operator $\Theta = i\sigma_y$.

The quantum spin Hall insulator is described by the Bernevig-Hughes-Zhang model [27], applicable to HgTe/HgCdTe and InAs/GaAs/AlSb quantum wells. For the numerical simulations, we use the extended model of Ref. [30] (see Appendix 6.5.2), which includes spin-orbit coupling contributions due to bulk inversion asymmetry and structural inversion asymmetry, and the material parameters reported in Ref. [31].

To extract the three-terminal scattering matrices of the normal state, we discretize the two models on a square lattice with lattice constant a. We adopt the circular dot geometry shown in Fig. 6.2, with a radius $R = 20a$ and three leads of width R. We consider the electrostatic disorder $V(\mathbf{r})$ to be uncorrelated and uniformly distributed in an interval $[-u, u]$. After obtaining the scattering matrix of the junction we use a gauge with $\phi_3 = 0$ and solve the eigenvalue problem (6.10) as a function of the remaining two phases ϕ_1, ϕ_2. We perform the numerical simulations using the Kwant code [32]. The scripts with the source code are available online as ancillary files for this preprint.

6.3.1 Splitting of Kramers degeneracy

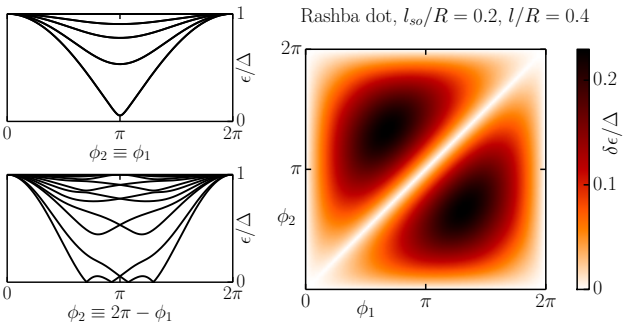

Figure 6.4. *Left*: Phase dependence of the Andreev levels of a Rashba dot with $\mu = 1/4ma$ for $\phi_2 = \phi_1$ (top) and $\phi_2 = 2\pi - \phi_1$ (bottom). Kramers degeneracy is present in the top panel (since one of the phase differences is zero), but not in the bottom panel. *Right*: energy difference $\delta\epsilon$ between the two lowest Andreev levels in a Rashba dot averaged over 10^2 values of $\mu \in [0, 1/2ma]$ for a fixed disorder configuration.

The first property we study is the splitting of the Andreev levels. The two-fold degenerate two-terminal junction spectrum of Eq. (6.1) should be recovered whenever any two out of three phase differences are equal, i.e. when either $\phi_1 = \phi_2$, $\phi_1 = 0$, or $\phi_2 = 0$. Away from this limit, we expect deviation from the two-terminal case and a finite splitting of the Kramers doublets.

A comparison of two typical energy spectra computed for a Rashba dot is shown in the left panel of Fig. 6.4 and confirms our expectations. To consider the experimentally relevant situation we choose spin-orbit interaction strength α and the disorder strength u such that the spin-orbit length $l_{\mathrm{so}} \equiv (m\alpha)^{-1}$ and the mean free path $l \equiv 6\,(mau^2)^{-1}\,\sqrt{\mu/2ma}$ are both smaller than R, but have the same order of magnitude. We first confirm that when $\phi_1 = \phi_2$ the spectrum consists of Kramers doublets with the energies given by Eq. (6.1). On the other hand, when the two phases are opposite, $\phi_2 = 2\pi - \phi_1$, the Kramers pairs of Andreev levels have different energies, except for the time-reversal invariant points $(\phi_1, \phi_2) = 0 \mod 2\pi$. One can also notice the presence of Andreev levels crossings at zero-energy.

To quantify the observed splitting of Kramers degeneracy, we consider the energy difference $\delta\epsilon$ between the two levels belonging to the lowest Kramers doublet. These two levels are of particular interest since they correspond to the most transparent transport channels and their energies are most sensitive to the phase differences. In the right panel of Fig. 6.4 the splitting $\delta\epsilon$ is computed for a Rashba dot, averaged over different values of μ in the dot. It is zero in the two-terminal limit and rises up to $\delta\epsilon \sim 0.2\,\Delta$ away from it. Hence, Fig. 6.4 confirms our conclusions that Kramers pairs of Andreev levels can be split by an energy of an order Δ solely by varying the superconducting phases. The maximal possible splitting is limited by level repulsion, and as expected, we also find that $\delta\epsilon$ is inversely proportional to the total number of Kramers doublets present in the spectrum.

6.3.2 Andreev level crossings at zero energy

By checking the Andreev level spectra of different quantum dots, we find that zero-energy crossings indeed occur for some scattering regions, as shown in the left panel of Fig. 6.5. A simulation of a QSH dot[3] also

[3]We use the parameters for an InAs/GaAs/AlSb quantum well, with layer thickness of 10 nm for both GaSb and InAs [31], in a dot with radius $R \simeq 200$ nm, onsite disorder

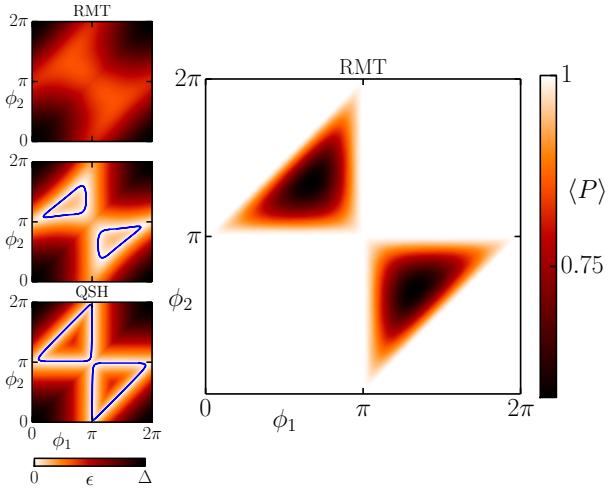

Figure 6.5. *Left:* Examples of the minimum energy ϵ of an Andreev bound state as a function of (ϕ_1, ϕ_2). The first two examples are calculated using random scattering matrices, with and without zero-energy crossings. The positions of the crossings are found numerically using method of App. 6.5.1, and are marked in blue. They form closed curves encircling domains of odd ground state fermion parity. The third example is for a QSH dot in the non-trivial phase, so that the fermion parity switch appears almost exactly at the boundary of the allowed zone. *Right:* ground state fermion parity $\langle P \rangle$ averaged over 10^4 random matrices of size $n = 6$, showing that fermion parity may only be odd only if the discrete vortex condition (6.21) is fulfilled.

confirms the conclusion of Sec. 6.2.4 that quantum spin Hall insulators maximize the area in the phase space where the ground state fermion parity is odd. This behavior is in contrast with that of two-terminal setups, where Eq. (6.1) dictates that a Andreev level crossing at zero-energy may only occur in a time-reversal invariant system in the presence of a perfectly transmitted mode. The stringent requirement of perfect transparency is removed in a multiterminal setup.

In Section 6.2.3 we proved that zero-energy crossings occur only if a discrete vortex is present at the junction. For a more systematic study of the occurrence of the zero-energy crossings, we compute the average ground state fermion parity $\langle P \rangle$ as a function of ϕ_1 and ϕ_2 using RMT, with the results shown in the right panel of Fig. (6.5). The figure shows that the parity deviates from the even value, $\langle P \rangle = 1$, in exact agreement

strength $u = 25$ meV, and $\mu = 0$.

with the vortex condition, Eq. (6.21).

6.3.3 Density of states

We now study the properties of the complete Andreev spectrum. In the top panel of Fig. 6.6 we show the subgap density of states $\rho(\epsilon)$ of a Rashba dot, obtained for a single disorder realization while averaging over different values of μ in the dot. We observe several features of this density of states. First, when zero-energy crossings are forbidden an energy gap is present in the spectrum, in agreement with the lower bound of Eq. (6.20). Second, when crossings are allowed, a spectral peak develops at zero energy. Finally, at the time-reversal symmetric point $(\phi_1, \phi_2) = (\pi, \pi)$ there is no hard gap in the spectrum but the density of states vanishes at zero energy.

The latter two features are explained by the random matrix theory of chaotic Andreev dots. The presence of a spectral peak at zero energy is expected in a chaotic superconducting dot with broken spin rotation and time-reversal symmetries (symmetry class D). In this case, the expected density of states profile is given by [16, 14, 17, 18]:

$$\rho(\epsilon) = \delta^{-1} \left[1 + \sin(x)/x\right] , \tag{6.24}$$

with $x = 2\pi\epsilon/\delta$, and δ the average level spacing at the Fermi level. At the time-reversal symmetric point (π, π) the junction has the symmetry class DIII. In this case we expect the density of states to vanish at the Fermi level [33, 14, 17], with profile

$$\rho(\epsilon) = \delta^{-1} \left[\pi^2 x (J_1'(x) J_0(x) + J_1^2(x)) + \pi J_1(x)\right] , \tag{6.25}$$

where J_0 and J_1 are Bessel functions of the first kind.

These corrections to the density of states near zero energy can be observed in our system more clearly by computing the density of states from RMT, see the bottom panel of Fig. 6.6. There we compare the density of states at the center of the "discrete vortex" $(\phi_1, \phi_2) = (2\pi/3, \pi/3)$ and at the time-reversal symmetric point $(\phi_1, \phi_2) = (\pi, \pi)$ to Eqs. (6.24) and (6.25) respectively, using δ as a fitting parameter. We find that close to the Fermi level the density profiles are in a good agreement with random matrix theory predictions. This result is the final confirmation that in a multiterminal short Josephson junction all the consequences of the time-reversal symmetry present in the normal state are removed in the superconducting state by the phase differences.

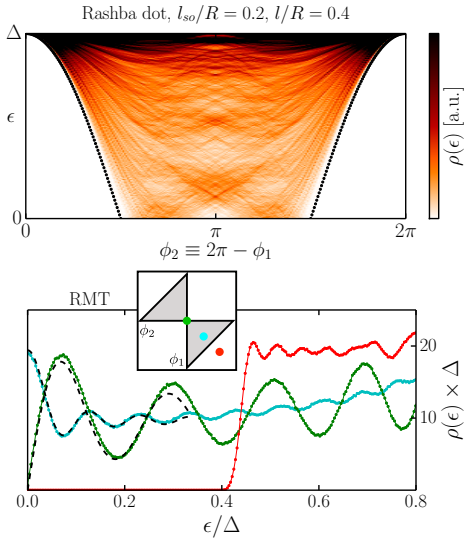

Figure 6.6. *Top:* density of states $\rho(\epsilon)$ of a Rashba dot, computed along the diagonal $\phi_2 = 2\pi - \phi_1$ and averaged over 10^3 values of $\mu \in [0, 1/2ma]$ for a single disorder realization. Spin-orbit coupling α and disorder strength u are the same as in Fig. 6.4. The dotted line shows the lower bound on the Andreev state energy (6.20). *Bottom:* Density of states obtained from 10^6 random scattering matrices with 10 modes per lead, computed for the three different values of (ϕ_1, ϕ_2) shown in the inset: in the gapped region [red, $(3\pi/4, \pi/4)$], in presence of a discrete vortex [blue, $(4\pi/3, 2\pi/3)$], and at the time-reversal invariant point [green, (π, π)]. The black dashed lines are fits of Eqs. (6.24) and (6.25), with a single free parameter δ.

6.3.4 Effect of finite junction size

Most of our results are applicable in the short junction limit. If the size of the junction is increased, the short junction approximation of Eq. (6.5) gradually loses its validity. We now consider the corrections to the short junction limit. In order to do so we include the superconducting pairing explicitly in the Hamiltonian, rather than as a boundary condition for the scattering problem. We therefore compute the subgap energy spectrum by diagonalizing the Bogoliubov-de Gennes Hamiltonian

$$H_{\mathrm{BdG}} = \begin{pmatrix} H & \Delta(\mathbf{r}) \\ \Delta^*(\mathbf{r}) & -H \end{pmatrix}, \tag{6.26}$$

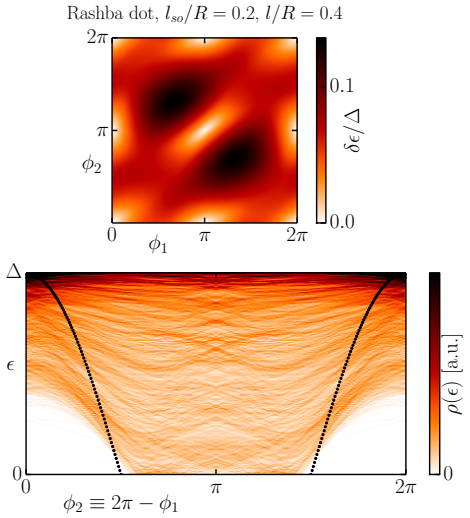

Figure 6.7. Spectral properties of a three-terminal junction made in a Rashba dot and with finite $\Delta = 0.01/2ma$, showing the effect of an increased size of the junction. All other parameters are as in Fig. 6.4. *Top:* energy difference $\delta\epsilon$ between the two lowest Andreev levels, averaged over 10 values of $\mu \in [0, 1/2ma]$. *Bottom:* density of states of the junction, obtained by averaging over 200 values of $\mu \in [0, 1/2ma]$, for a single disorder configuration and a fixed value of μ in the three arms of the junction. Black dots are the lower bound (6.20), which is valid in the limit $\Delta/E_T \to 0$.

where H is the Rashba Hamiltonian (6.23). We apply H to the geometry of Fig. 6.2, with $\Delta(\mathbf{r}) = 0$ in the central region and $\Delta(\mathbf{r}) = \Delta \exp(i\phi_i)$ in the three leads. We consider finite length leads, interrupted at a distance $L \gtrsim \xi$ away from the junction.

In Fig. 6.7 we show the results for a junction with $\Delta = 0.01/2ma$, and all other parameters the same as in Sec. 6.3.1. As expected, the subgap level spacing and hence the energy splitting of Kramers pairs are reduced in a longer junction. In particular, the energy splitting of Kramers pair remains finite when two phases in the leads are equal and it only vanishes at time-reversal invariant points. The lower bound (6.20) on the energy gap ceases to be valid, as can be seen already from the presence of subgap states at zero phase difference. Nevertheless, in agreement with our expectations, the vortex condition (6.21) for a zero-energy crossing remains valid.

6.4 Conclusions and discussion

In conclusion, we have introduced a new method of manipulation of single electron states, which relies solely on applying the superconducting phase differences. This approach has several advantages over the standard ways that rely on the direct application of magnetic fields. It allows one to manipulate electron spin locally both in space and time, and to implement long range spin-spin coupling by using inductive coupling of the supercurrents. Finally, it is not disruptive to superconductivity, making it ideal to apply to hybrid devices.

We demonstrated that, unlike in two terminal Josephson junctions, superconducting phase difference can induce splitting of the Kramers degeneracy in the spectrum comparable to the superconducting gap when more than two superconducting leads are used. We proved that there is a universal lower bound on the induced gap in the junction, which only depends on the phases of different terminals. This lower bound vanishes when the phases of the superconducting leads form a discrete vortex. In that case the ground state fermion parity is allowed to become odd, so that the junction traps an extra fermion in its ground state.

Our findings can be directly tested experimentally using tunneling spectroscopy. This requires adding an extra normal or superconducting lead weakly coupled to the scattering region, and performing voltage bias conductance measurements. The Andreev excitation spectrum of a Josephson junction has also been studied experimentally using microwave absorption spectroscopy [34, 35] or measuring switching current probabilities [36, 37]. Either of these two methods will likewise permit to test our predictions, since both methods are equally applicable to multiterminal junctions.

We expect our results to be testable for junctions defined in any material with a sufficiently strong spin-orbit interaction. Our method of breaking Kramers degeneracy works best in materials with low effective electron mass, since that ensures large normal level spacing. For instance, for an InAs quantum dot with a radius $R \simeq 100$ nm we estimate a level spacing $\delta_0 \simeq \hbar^2\pi^2/8m_{\text{eff}}R^2 = 0.5$ meV in the normal state, thus making the short junction limit $\Delta \ll n\delta_0$ within easy reach in the case of aluminum contacts. In addition to the natural candidates such as InAs, InSb quantum wells, or quantum spin Hall insulators, the recently discovered InSb nanocrosses [38] make a promising candidate for observing

the physics of multiterminal SNS junction. Conventional metallic SNS junctions would not show the effects of time-reversal symmetry breaking due to the extremely small level spacing. However, superconducting break junctions [36] could potentially permit the implementation of multiterminal geometries involving a very small number of modes with a large level spacing.

There is an entirely different aspect of broken time-reversal and spin rotation symmetries in mesoscopic systems, which is beyond the scope of our investigation, but which can also be studied using our methods. If the scattering region is additionally strongly coupled to a normal lead, a persistent zero-bias peak in the Andreev conductance is formed [39–41]. In our case, we expect such a peak to develop in the presence of a discrete vortex, and to disappear in its absence.

Another venue of further investigation is to study the quantum nature of the Andreev bound states. Trapping a single Bogoliubov quasiparticle in a Josephson junction is a promising way to isolate and manipulate a spin degree of freedom - a superconducting spin qubit [10, 12, 13]. A spin-$\frac{1}{2}$ state in a Josephson junction is expected to be very stable at low temperatures, due to the energy gap of the superconductor. These long-lived odd states have been recently observed via switching current measurements in superconducting point contacts [36, 37, 42]. The advantage of using multiterminal Josephson junctions for such qubits is that the presence of several tunable phase differences makes it possible to implement universal quantum manipulation exclusively by inductive means.

Finally, our discovery provides a better way to creating Majorana bound states in superconductor-semiconductor hybrid systems, a focus of an active experimental search [43–49]. The complication that arises in many experiments is that magnetic field required to induce a non-trivial gap in the semiconductor is too strong and spoils the properties of the superconductor. Using superconducting phases as a means of breaking time reversal symmetry and Kramers degeneracy would allow one to reach the same goal without any detrimental effect on the superconductor. Potentially it would even allow one to use aluminum, which forms high quality contacts with semiconductors and is the simplest superconducting material to use in fabrication, and whose application to Majoranas was so far limited by its extremely small critical field. One promising use of our method for creation of Majoranas is to combine multiple superconducting

leads with an engineered Kitaev chain geometry of Refs. [50–52].

6.5 Appendix

6.5.1 Occurrence of a zero-energy crossing as a generalized eigenvalue problem

Given the scattering matrices s and r_A, it is possible to determine whether zero-energy solutions exist in the (ϕ_1, ϕ_2) plane without solving for the spectrum. To do so, we can recast Eq. (6.10) at $\epsilon = 0$ as a generalized eigenvalue problem of the form

$$X\,\Psi^e_{\text{in}} = \mathrm{e}^{-i\phi_1}\; Y\,\Psi^e_{\text{in}} \tag{6.27}$$

We give the explicit form of X and Y in the case of three leads. If s has the following block structure,

$$s = \begin{pmatrix} r_{11} & t_{12} & t_{13} \\ -t_{12}^T & r_{22} & t_{23} \\ -t_{13}^T & -t_{23}^T & r_{33} \end{pmatrix}, \tag{6.28}$$

then X and Y are given by

$$X = \begin{pmatrix} 0 & -\mathrm{e}^{-i\phi_2}\, t_{12} & -t_{13} \\ \mathrm{e}^{-i\phi_2}\, t_{12}^T & 2\,\mathrm{e}^{-i\phi_2}\, r_{22} & -\left(1+\mathrm{e}^{-i\phi_2}\right)\, t_{23} \\ t_{13}^T & \left(1+\mathrm{e}^{-i\phi_2}\right)\, t_{23}^T & 2r_{33} \end{pmatrix},$$
$$Y = \begin{pmatrix} 2\,r_{11} & t_{12} & t_{13} \\ -t_{12}^T & 0 & 0 \\ -t_{13}^T & 0 & 0 \end{pmatrix}. \tag{6.29}$$

The existence of a zero-energy crossing at the position (ϕ_1, ϕ_2) can then be determined numerically by checking that Eq. (6.27) has eigenvalues with unit norm.

6.5.2 BHZ Hamiltonian

The BHZ Hamiltonian describing a 2D quantum spin Hall insulator reads [30]:

$$H_{\text{BHZ}} = H_0 + H_{\text{BIA}} + H_{\text{SIA}} + V(\mathbf{r}), \tag{6.30}$$

with $V(\mathbf{r})$ the electrostatic disorder, and

$$H_0 = \begin{pmatrix} h(\mathbf{p}) & 0 \\ 0 & h^*(-\mathbf{p}) \end{pmatrix}, \tag{6.31a}$$

$$H_{\mathrm{BIA}} = \begin{pmatrix} 0 & 0 & \Delta_e p_+ & -\Delta_z \\ 0 & 0 & \Delta_z & \Delta_h p_- \\ \Delta_e p_- & \Delta_z & 0 & 0 \\ -\Delta_z & \Delta_h p_+ & 0 & 0 \end{pmatrix}, \tag{6.31b}$$

$$H_{\mathrm{SIA}} = \begin{pmatrix} 0 & 0 & i\xi_e p_- & 0 \\ 0 & 0 & 0 & 0 \\ -i\xi_e^* p_+ & 0 & 0 & 0 \\ 0 & 0 & 0 & 0 \end{pmatrix}, \tag{6.31c}$$

and

$$h(\mathbf{p}) = (C - D\mathbf{p}^2)\sigma_0 + A(p_x\sigma_x - p_y\sigma_y) + (M - B\mathbf{p}^2)\sigma_z\,.$$

Here, σ are the Pauli matrices in orbital space, $\mathbf{p}$ is the momentum operator, and $p_\pm = p_x \pm ip_y$. The system is in a topologically nontrivial phase whenever $M < 0$.

Bibliography

[1] H. A. Kramers, Proc. Amsterdam Acad. **33**, 959 (1930).

[2] E. Wigner, Nachrichten von der Gesellschaft der Wissenschaften zu Göttingen, Mathematisch-Physikalische Klasse **1932**, 546 (1932).

[3] D. Loss and D. P. DiVincenzo, Phys. Rev. A **57**, 120 (1998).

[4] S. A. Wolf, D. D. Awschalom, R. A. Buhrman, J. M. Daughton, S. v. Molnár, M. L. Roukes, A. Y. Chtchelkanova, and D. M. Treger, Science **294**, 1488 (2001).

[5] I. Žuticć, J. Fabian, and S. Das Sarma, Rev. Mod. Phys. **76**, 323 (2004).

[6] J. Alicea, Rep. Prog. Phys. **75**, 076501 (2012).

[7] C. W. J. Beenakker, Ann. Rev. Cond. Mat. Phys. **4**, 113 (2013).

[8] C. W. J. Beenakker, Phys. Rev. Lett. **67**, 3836 (1991).

[9] J. H. Bardarson, J. Phys. A **41**, 405203 (2008).

[10] N. M. Chtchelkatchev and Y. V. Nazarov, Phys. Rev. Lett.**90**, 226806 (2003).

[11] B. Béri, J. H. Bardarson, and C. W. J. Beenakker, Phys. Rev. B **77**, 045311 (2008).

[12] C. Padurariu and Y. V. Nazarov, Phys. Rev. B **81**, 144519 (2010).

[13] C. Padurariu and Y. V. Nazarov, Europhys. Lett. **100**, 57006 (2012).

[14] A. Altland and M. R. Zirnbauer, Phys. Rev. B **55**, 1142 (1997).

[15] C. W. J. Beenakker, J. M. Edge, J. P. Dahlhaus, D. I. Pikulin, S. Mi, and M. Wimmer, Phys. Rev. Lett. **111**, 037001 (2013).

[16] M. L. Mehta, Random Matrices (Elsevier S& T, 2004).

[17] D. A. Ivanov, J. Math. Phys. **43,** 126 (2002).

[18] D. Bagrets and A. Altland, Phys. Rev. Lett. **109**, 227005 (2012).

[19] C. Wu, B. A. Bernevig, and S.-C. Zhang, Phys. Rev. Lett. **96**, 106401 (2006).

[20] I. C. Fulga, F. Hassler, and A. R. Akhmerov, Phys. Rev. B **85**, 165409 (2012).

[21] C. W. J. Beenakker, Rev. Mod. Phys. **69**, 731 (1997).

[22] A. Y. Kitaev, Phys. Uspekhi **44**, 131 (2001).

[23] H.-J. Kwon, K. Sengupta, and V. M. Yakovenko, Euro. Phys. J. B **37**, 349 (2003).

[24] L. Fu and C. L. Kane, Phys. Rev. B **79**, 161408 (2009).

[25] C. L. Kane and E. J. Mele, Phys. Rev. Lett. **95**, 146802 (2005).

[26] C. L. Kane and E. J. Mele, Phys. Rev. Lett. **95**, 226801 (2005).

[27] B. A. Bernevig, T. L. Hughes, and S.-C. Zhang, Science **314**, 1757 (2006).

[28] M. König, S. Wiedmann, C. Brüune, A. Roth, H. Buhmann, L. W. Molenkamp, X.-L. Qi, and S.-C. Zhang, Science **318**, 766 (2007).

[29] F. Mezzadri, Notices Am. Math. Soc. **54**, 592 (2007).

[30] C. Liu, T. L. Hughes, X.-L. Qi, K. Wang, and S.-C. Zhang, Phys. Rev. Lett. **100**, 236601 (2008).

[31] C. Liu and S. Zhang, in Contemporary Concepts of Con- densed Matter Science, Topological Insulators, Vol. 6, edited by M. Franz and L. Molenkamp (Elsevier, 2013) pp. 59 to pp. 89.

[32] C. W. Groth, M. Wimmer, A. R. Akhmerov, and X. Wain- tal, New J. Phys. **16**, 063065 (2014).

[33] T. Nagao and K. Slevin, J. Math. Phys. **34**, 2075 (1993).

[34] L. Bretheau, Ç. Ö. Girit, H. Pothier, D. Esteve, and C. Urbina, Nature **499**, 312 (2013).

[35] L. Bretheau, Ç. Ö. Girit, M. Houzet, H. Potheir, D. Esteve, and C. Urbina, arXiv:1406.6301 (2014).

[36] M. Zgirski, L. Bretheau, Q. Le Masne, H. Pothier, D. Esteve, and C. Urbina, Phys. Rev. Lett. **106**, 257003 (2011).

[37] L. Bretheau, Ç. Ö. Girit, C. Urbina, D. Esteve, and H. Pothier, Phys. Rev. X **3**, 041034 (2013).

[38] S. R. Plissard, I. van Weperen, D. Car, M. A. Verheijen, G. W. G. Immink, J. Kammhuber, L. J. Cornelissen, D. B. Szombati, A. Geresdi, S. M. Frolov, L. P. Kouwenhoven, and E. P. A. M. Bakkers, Nat. Nano. **8**, 859 (2013).

[39] D. I. Pikulin and Y. V. Nazarov, JETP Lett. **94**, 693 (2012).

[40] D. I. Pikulin, J. P. Dahlhaus, M. Wimmer, H. Schomerus, and C. W. J. Beenakker, New J. Phys. **14**, 125011 (2012).

[41] S. Mi, D. I. Pikulin, M. Marciani, and C. W. J. Beenakker, arXiv:1405.6896 (2014).

[42] D. G. Olivares, A. L. Yeyati, L. Bretheau, Ç. Ö. Girit, H. Pothier, and C. Urbina, Phys. Rev. **B** 89, 104504 (2014).

[43] V. Mourik, K. Zuo, S. M. Frolov, S. R. Plissard, E. P. a. M. Bakkers, and L. P. Kouwenhoven, Science **336**, 1003 (2012).

[44] A. Das, Y. Ronen, Y. Most, Y. Oreg, M. Heiblum, and H. Shtrikman, Nat. Phys. **8**, 887 (2012).

[45] I. Knez, R.-R. Du, and G. Sullivan, Phys. Rev. Lett. **109**, 186603 (2012).

[46] W. Chang, V. E. Manucharyan, T. S. Jespersen, J. Nygård, and C. M. Marcus, Phys. Rev. Lett. **110**, 217005 (2013).

[47] E. J. H. Lee, X. Jiang, R. Aguado, G. Katsaros, C. M. Lieber, and S. De Franceschi, Phys. Rev. Lett. **109**, 186802 (2012).

[48] E. J. H. Lee, X. Jiang, M. Houzet, R. Aguado, C. M. Lieber, and S. De Franceschi, Nat. Nano. **9**, 79 (2014).

[49] S. Hart, H. Ren, T. Wagner, P. Leubner, M. Mühlbauer, C. Brüne, H. Buhmann, L. W. Molenkamp, and A. Yacoby, arXiv:1312.2559 (2013).

[50] A. Romito, J. Alicea, G. Refael, and F. von Oppen, Phys. Rev. B **85**, 020502 (2012).

[51] J. D. Sau and S. D. Sarma, Nat. Comm. **3**, 964 (2012).

[52] I. C. Fulga, A. Haim, A. R. Akhmerov, and Y. Oreg, New J. Phys. **15**, 045020 (2013).

Samenvatting

Majorana nul-toestanden zijn gebonden toestanden die optreden in het midden van de excitatie-gap (het nulpunt van energie), in materialen die bekend staan als topologische supergeleiders. Zij hebben de potentie om een bouwsteen te worden voor een kwantumcomputer, en zij zijn ook van zichzelf interessant vanwege het bijzondere effect dat zij hebben op transporteigenschappen. Het onderwerp van dit proefschrift is de theoretische studie van Majorana nul-toestanden in systemen van verschillende dimensionaliteit: de twee-dimensionale kwantum-spin-Hall-isolator, de één-dimensionale nanodraad, en de nul-dimensionale kwantumdot.

Na een korte inleiding in Hoofdstuk 1, over het concept van een Majorana nul-toestand, beginnen we in Hoofdstuk 2 met het theoretische onderzoek aan de InSb nanodraad die experimenteel is onderzocht door de Kouwenhoven groep in Delft. De zachtheid van de geïnduceerde supergeleidende gap is een raadselachtig aspect van het experiment, dat we graag zouden willen begrijpen. We vinden dat de betrekkelijk grote vrije weglengte, in combinatie met de gedeeltelijke bedekking van de nanodraad door de supergeleider, de vermoedelijke oorzaak is van de zachte gap. Een belangrijke conclusie van onze studie is dat de aanwezigheid van de zachte gap noch de vorming noch de detectie belemmert van de Majorana nul-toestanden, die aan het eindpunt van de nanodraad zouden moeten optreden.

We gaan door met een ander systeem, de rand van een kwantum-spin-Hall-isolator, gevormd door een kwantumput in een samengestelde structuur van HgTe en CdTe of van InAs en GaSb. Het ontbreken van een tunnelbarrière in zo'n systeem was een obstakel in de zoektocht naar Majorana nul-toestanden. In Hoofdstuk 3 stellen we voor dat zwakke wanorde en een zwak magnetisch veld het mogelijk moeten maken om een barrière te vormen door middel van een gate-elektrode. Op deze

manier kan een Majorana nul-toestand worden opgesloten tussen deze gate-elektrode aan de ene kant en een supergeleidende elektrode aan de andere kant. Dit is een praktisch alternatief voor een barrière die gevormd zou moeten worden met behulp van een magnetische isolator. We laten zien dat een constrictie in de kwantumput het mogelijk maakt om Majorana nul-toestanden uit te wisselen (te "vlechten"). Dit is de stap die nodig is voor de toepassing in een kwantumcomputer.

We vervolgen onze studie van dit tweedimensionale systeem in Hoofdstuk 4, waar wij een opvallende waarneming onderzoeken van een groep uit Rice University, die hebben gevonden dat de randtoestanden in een InAs/GaSb kwantumput blijven bestaan in de aanwezigheid van een loodrecht magnetisch veld van 8 Tesla. Hoewel we de experimentele data niet helemaal kunnen verklaren, vinden we wel een ongebruikelijk fasediagram in onze modelberekening. Het kritische veld voor het verdwijnen van de randtoestanden splitst zich in tweeën op als de wanorde toeneemt. Er is een hoog kritisch veld voor de overgang naar een kwantum-Hall-isolator (met randtoestanden die slechts één richting op bewegen), en een laag kritisch veld voor de overgang naar metallische bulk-geleiding. The ruimtelijke scheiding van de geïnverteerde banden van de kwantumput, typisch voor de combinatie InAs/GaSb, is essentieel voor het optreden van de bulk-geleiding — het treedt niet op in de HgTe/CdTe kwantumputten die de Würzburg groep heeft onderzocht.

De laatste twee hoofdstukken gaan over kwantumdots, kleine halfgeleidende structuren die via puntcontacten met supergeleiders zijn verbonden. In Hoofdstuk 5 onderzoeken we het optreden van resonanties in the stroom-spanning karakteristiek bij spanning nul. Deze zouden een kenmerk zijn van Majorana nul-toestanden. We vinden dat het karakteristieke Y-vormige resonantieprofiel in het B, V vlak (B is magnetisch veld, V is spanning) niet noodzakelijkerwijs een teken is van Majorana nul-toestanden. De polen van de verstrooiingsmatrix in het complexe energievlak hebben de neiging om vast te blijven zitten aan de imaginaire as, zelfs in het topologische triviale regime, eenvoudigweg als gevolg van deeltje-antideeltje symmetrie. Wat hiervoor nodig is, is gebroken tijdsomkeersymmetrie en gebroken spin-rotatiesymmetrie. (We spreken dan van symmetrie-klasse D.) Als de spin behouden is (klasse C) treedt het effect niet op. We stellen methodes voor, waarop deze "valse" Majorana-resonanties van de echte kunnen worden onderscheiden.

Tenslotte onderzoeken we in Hoofdstuk 6 of het mogelijk is om

tijdsomkeersymmetrie effectief te breken door het aanbrengen van een faseverschil tussen supergeleiders in een kwantumdot met meerdere puntcontacten. De noodzaak om een magnetisch veld aan te leggen is een ernstige experimentele complicatie, en het zou prachtig zijn als die vermeden zou kunnen worden. Drie contacten zijn voldoende om een "discrete vortex" te realiseren, die de meeste effecten nabootst van een werkelijke magnetische vortex. We tonen aan dat het mogelijk is om de elektronenpariteit van de supergeleidende grondtoestand te wisselen door de supergeleidende faseverschillen te variëren, zonder enig magnetisch veld in de kwantumdot aan te brengen. Een aanpassing van dit ontwerp (in combinatie met een topologische isolator) zou gebruikt kunnen worden om Majorana nul-toestanden te vangen en te manipuleren zonder magnetisch veld.

Summary

Majorana zero-modes are states that appear in the middle of the excitation gap (the zero-point of energy), in materials known as topological superconductors. They have the potential to become a building block for a quantum computer and are also of interest in their own right, because of their unusual effect on transport properties. The topic of this thesis is the theoretical study of the Majorana zero-modes in systems of different dimensionality: the two-dimensional quantum spin Hall insulator, the one-dimensional nanowire, and the zero-dimensional quantum dot.

Following a brief Introduction in Chapter 1 on the concept of a Majorana zero-mode, Chapter 2 begins to examine them in the InSb nanowire that has been studied experimentally by the Kouwenhoven group in Delft. The softness of the induced superconducting gap is a puzzling aspect of the experiment that we would like to understand. We find that the relatively large mean free path, in combination with a partial coverage of the nanowire by the superconductor, is the likely origin of the soft gap. One important conclusion of our study is that the presence of a soft gap does not prevent the formation and observation of a Majorana zero-mode at the end-point of the wire.

We then move on to the edge of a quantum spin-Hall insulator, formed by a quantum well in a heterostructure of HgTe/CdTe or InAs/GaSb. The lack of a tunnel barrier in such a system was an obstacle in the search for Majorana zero-modes. In Chapter 3 we propose that in the presence of weak disorder and weak magnetic field, a gate tunable metallic puddle can play the role of a barrier for the edge states, confining the Majorana zero-mode at the interface with a superconductor. This is a practical alternative to barriers formed out of magnetic insulators. We show that a constriction in the quantum well allows for braiding of Majorana zero-modes on opposite edges, which is the key step needed for applications

in quantum computing.

We continue with this two-dimensional system in Chapter 4, where we investigate the remarkable observation by the group from Rice University that the helical edge states in InAs/GaSb quantum wells persist in perpendicular magnetic fields as large as 8T. Although we cannot quite explain the experimental data, we do find an unusual phase diagram in our model calculation: The critical breakdown field for helical edge conduction splits into two fields with increasing disorder, an upper critical field for the transition into a quantum Hall insulator (supporting chiral edge conduction) and a lower critical field for the transition to bulk conduction in a quasi-metallic regime. The spatial separation of the inverted bands, typical for broken-gap InAs/GaSb quantum wells, is essential for the magnetic-field induced bulk conduction — there is no such regime in the HgTe quantum wells studied by the Würzburg group.

The last two chapters deal with quantum dots, coupled to superconductors by point contacts. In Chapter 5 we study the appearance of zero-bias resonances in the differential conductance, which are a hallmark of Majorana zero-modes. We find that the characteristic Y-shaped resonance profile in the B, V plane (B is magnetic field, V is applied voltage) is not necessarily a Majorana signature. The poles of the scattering matrix have a tendency to stick to the imaginary energy axis even in the topologically trivial regime, simply as a consequence of particle-hole symmetry. What is needed is broken time-reversal and broken spin-rotation symmetry (known as symmetry class D). When spin is conserved (class C) the effect does not appear. We suggest ways in which these "fake" Majorana resonances can be distinguished from the real thing.

Finally, in Chapter 6 we investigate whether it is possible to effectively break time-reversal symmetry by applying a phase difference between superconductors in a multi-terminal superconducting quantum dot. The need to apply a magnetic field is a severe experimental complication, and it would be very welcome if this could be avoided. Three terminals suffice to realize a "discrete vortex", which mimics most of the effects of a true magnetic vortex. We demonstrate that it is possible to switch the fermion parity of the superconducting ground state by varying the phase differences, all at zero magnetic field in the quantum dot. A modification of this design (combining it with a topological insulator) might be used to trap and manipulate Majorana zero-modes in zero magnetic field.

List of Publications

1. *Size effect of Ruderman-Kittel-Kasuya-Yosida interaction mediated by electrons in nanoribbons*, Shuo Mi, Shuo-hong Yuan, and Pin Lyu, J. Appl. Phys. **109**, 083931 (2011).

2. *Proposal for the detection and braiding of Majorana fermions in a quantum spin Hall insulator*, Shuo Mi, D. I. Pikulin, M. Wimmer, and C. W. J. Beenakker, Phys. Rev. B **87**, 241405(R) (2013). [Chapter 3]

3. *Wigner-Poisson statistics of topological transitions in a Josephson junction*, C. W. J. Beenakker, J. M. Edge, J. P. Dahlhaus, D. I. Pikulin, Shuo Mi, and M. Wimmer, Phys. Rev. Lett. **111**, 037001 (2013).

4. *Disorder and magnetic-field induced breakdown of helical edge conduction in an inverted electron-hole bilayer*, D. I. Pikulin, T. Hyart, Shuo Mi, J. Tworzydło, M. Wimmer, and C. W. J. Beenakker, Phys. Rev. B **89**, 161403(R) (2014); *Erratum* Phys. Rev. B. **89**, 199901 (2014). [Chapter 4]

5. *X-shaped and Y-shaped Andreev resonance profiles in a superconducting quantum dot*, Shuo Mi, D. I. Pikulin, M. Marciani, and C. W. J. Beenakker, JETP **119**, 1018–1027 (2014). [Chapter 5]

6. *Single fermion manipulation via superconducting phase differences in multi-terminal Josephson junctions*, B. van Heck, Shuo Mi, and A. R. Akhmerov, Phys. Rev. B **90**, 155450 (2014). [Chapter 6]

7. *Impact of the soft induced gap on the Majorana zero-modes in semiconducting nanowires*, Shuo Mi, A. R. Akhmerov, and M. Wimmer, in preparation. [Chapter 2]

Curriculum Vitæ

I was born in Beijing, China, on June 24^{th} 1983, where I completed my primary, secondary, and high school education.

I then continued my undergraduate and master study at the College of Physics of Jilin University, Changchun, China. My bachelor thesis "Self-assembly process of branched block liquid crystal copolymers and a prospect view from system dynamics" was performed under supervision of Prof. Cheng-Xiang Zhang. In September 2008, I joined the research group of Prof. Pin Lyu for a master program in condensed matter theory and obtained a Master degree of Science with honors in July 2011 with thesis title "RKKY Magnetic Interaction in Nanostructures".

In the autumn of 2011, I received an opportunity to pursue my doctoral research in the group of Prof. C. W. J. Beenakker with a scholarship supported by China Scholarship Council (CSC) and Nederlandse Organisatie voor Wetenschappelijk Onderzoek (NWO) under the program of "Talent and Training China-Netherlands" (T&T) in cooperation with Casimir Research School. I benefited a lot from the discussions with my group members and fellows from the Instituut-Lorentz in Leiden and the Kavli Insitute of Nanoscience in Delft.

During my PhD years, I was a teaching assistant for the undergraduate course "Inleiding Fysica vaste stof" (Introduction to Solid State Physics) with Prof. H. Schiessel. I attended summer schools in Windsor, Les Houches, and Copenhagen, a winter school in Jerusalem, and other workshops and conferences. I presented my work in the United Kingdom, France, Germany, Russia, Denmark, and the Netherlands.